2. GLOBAL CLIMATE—K. M. Willett, D. F. Hurst, R. J. H. Dunn, and A. J. Dolman

a. Overview—K. M. Willett, D. F. Hurst, R. J. H. Dunn, and A. J. Dolman

Following the warmest year on record in 2014 according to most estimates, 2015 reached record warmth yet again, surpassing the previous record by more than 0.1°C. The considerable warmth, protracted strong El Niño, and new record levels of greenhouse gases provided climatological highlights for the year.

The progressing El Niño is a common theme woven throughout the essential climate variables (ECVs) presented here; its characteristic signature in temperature and water-related ECVs is clear across the maps in Plate 2.1. Having appeared in some indicators in 2014, and maturing in early 2015, this now-protracted event became the strongest since the 1997/98 El Niño. Indeed, many sections in this chapter compare the two events. Although strength-wise there are similarities, their characteristics are quite different (see Sidebar 1.1).

Atmospheric burdens of the three dominant greenhouse gases (CO_2, CH_4, N_2O) all continued to increase during 2015. The annual average CO_2 mole fraction at Mauna Loa, Hawaii (MLO), exceeded 400 ppm, a milestone never before surpassed in the MLO record or in measurements of air trapped in ice cores for up to 800 000 years. The 2015 global CO_2 average at Earth's surface was not far below, at 399.4 ± 0.1 ppm. The 3.1 ppm (0.76%) increase in CO_2 at Mauna Loa during 2015 was the largest annual increase observed in the 56-year record. Global average surface methane increased 11.5 ± 0.9 ppb (0.6%) from 2014 to 2015, the largest annual increase since 1997–98. Many ozone-depleting substances (ODS) continued to decline, lowering the stratospheric loading of halogen and the radiative forcing associated with ODS. Recent ozone measurements in the extra-polar upper stratosphere (~40 km) show a small increase that may be a first sign of long-term ozone layer recovery. Despite this, the 2015 Antarctic ozone hole was near-record in terms of size and persistence. Stratospheric water vapor just above the tropical tropopause increased 30% from December 2014 to December 2015, likely due to the combined changes in phase of the quasi-biennial oscillation (QBO) (cold to warm) and the El Niño–Southern Oscillation (ENSO) during 2015. The strong El Niño in 2015 produced extremely dry conditions in Indonesia, contributing to intense and widespread fires during August–November that produced anomalously high abundances of carbonaceous aerosols, carbon monoxide, and ozone in the tropical troposphere (Sidebar 2.2).

Significant forest fires were noted in many of the terrestrial variables, with emissions from tropical Asian biomass burning almost three times the 2001–14 average. Drier-than-average conditions were also evident over the global landmass. Soil moisture was below average for the entire year, and terrestrial groundwater storage was lower than at any other time during the record, which began in 2002. Areas in "severe" drought greatly increased, from 8% at the end of 2014 to 14% by the end of 2015. In keeping with the prevailing theme of warmer/drier, the global average surface air temperature record was accompanied by record high frequency of warm days and record low frequency of cool days. The lower troposphere was also close to record warmth.

Despite drier conditions on the ground, there was generally more moisture in the air as shown by the peaks in surface specific humidity and total column water vapor. These peaks were especially high over oceans, consistent with the generally warmer air. These warmer, moister conditions tend to lag El Niño by a few months, and the event was ongoing at year end.

In the cryosphere, Northern Hemisphere snow cover extent was slightly below average. However, alpine glacier retreat continued unabated and, with an update to the now 41-reference glacier dataset, 2015 became the 36th consecutive year of negative mass balance.

In addition to the strong El Niño, 2015 saw mostly positive Antarctic Oscillation (AAO) conditions throughout the year, contributing to stronger wind speed anomalies both at the surface and aloft (850 hPa). This typically leads to reduced west Antarctic Peninsula (WAP) sea ice extent, but it was opposed in 2015 by the El Niño, which is more often associated with a weaker polar jet stream. The North Atlantic Oscillation (NAO) was broadly positive for the fifth year in a row. Land wind speed continued a slight increase, similar to 2014, following a long, steady decline over the entire record from 1973.

The lake temperatures section returns this year after two years of unavailability. Additionally, two sidebars are included: Sidebar 2.1 explores our ability to monitor evaporation over land, a crucial missing link for studying the hydrological cycle; Sidebar 2.2 provides an overview of atmospheric chemical composition changes in 2015 as a result of El Niño–related forest fires.

Time series and anomaly maps for many EVCs are shown in Plates 1.1 and 2.1 respectively. Supplementary online figures can be found at: http://journals.ametsoc.org/doi/suppl/10.1175/2016BAMSStateoftheClimate.1.

(a) Lower Stratospheric Temperature

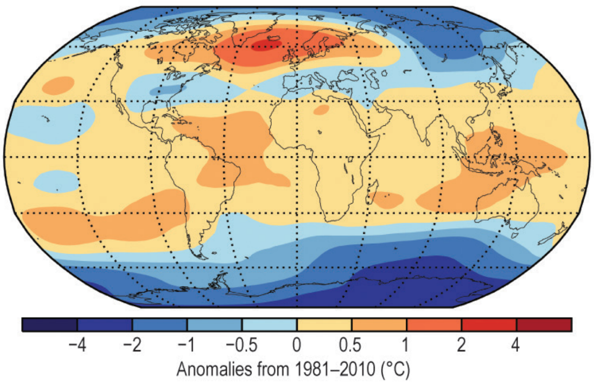

(b) Lower Tropospheric Temperature

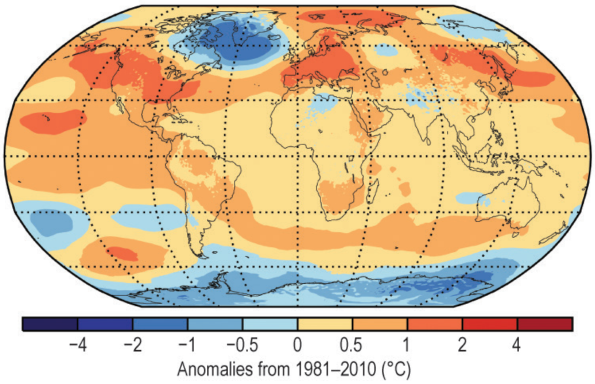

(c) Surface Temperature

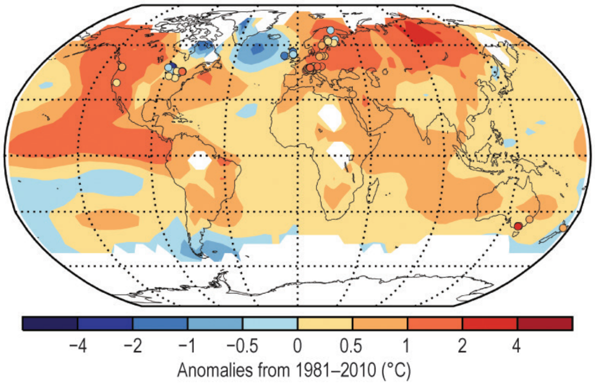

(d) Warm Days

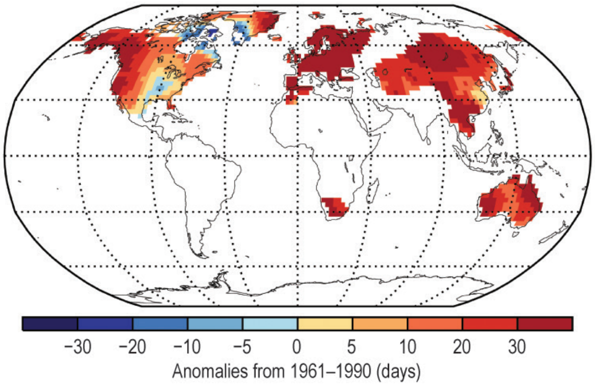

(e) Cool Days

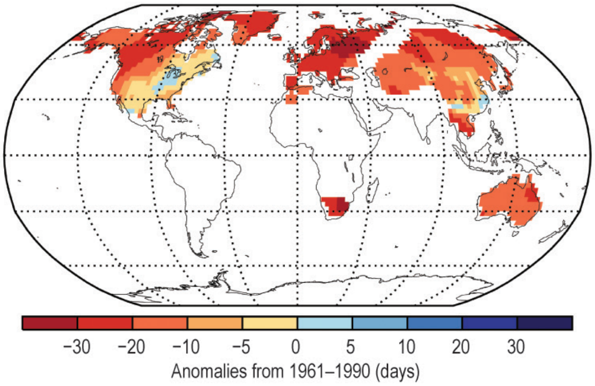

(f) Soil Moisture

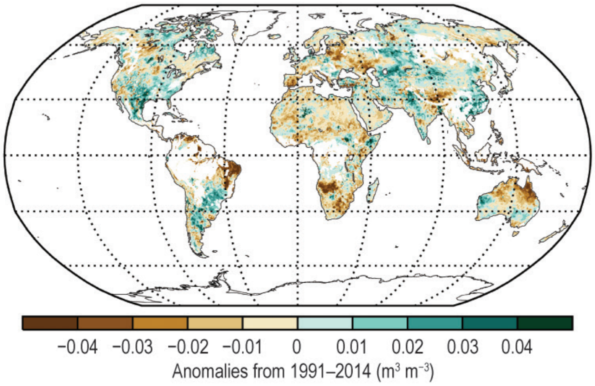

(g) Terrestrial Water Storage

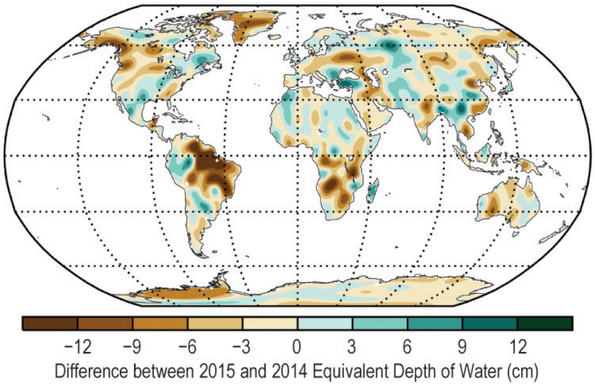

(h) Precipitation

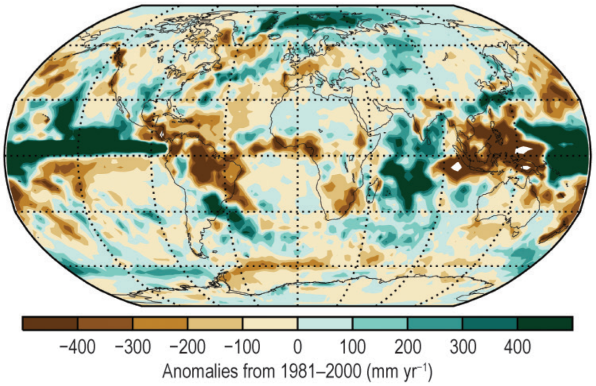

(i) Runoff

(m) Cloudiness

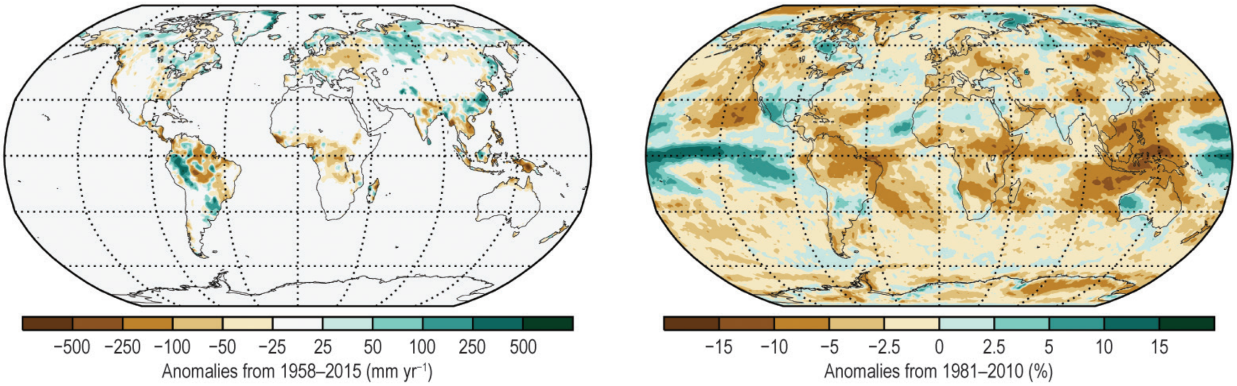

(j) River Discharge

(n) Upper Tropospheric Humidity

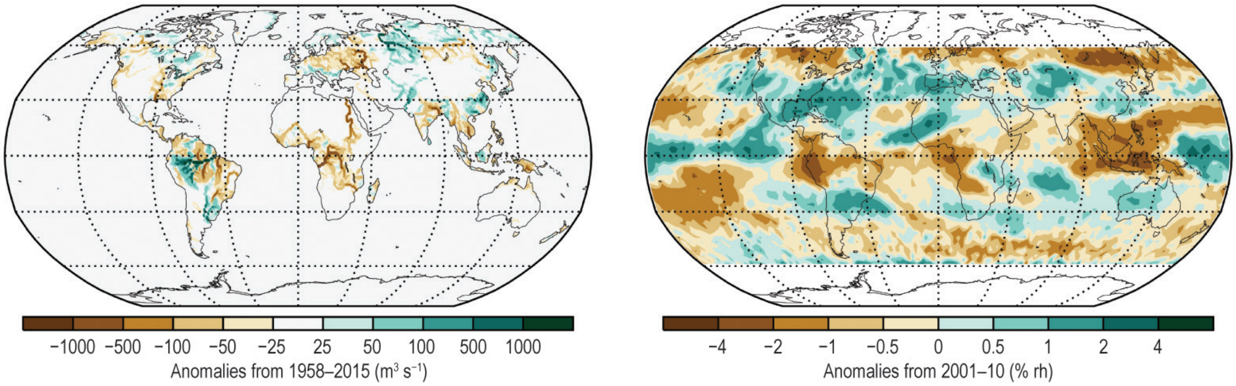

(k) Surface Specific Humidity

(o) Total Column Water Vapor

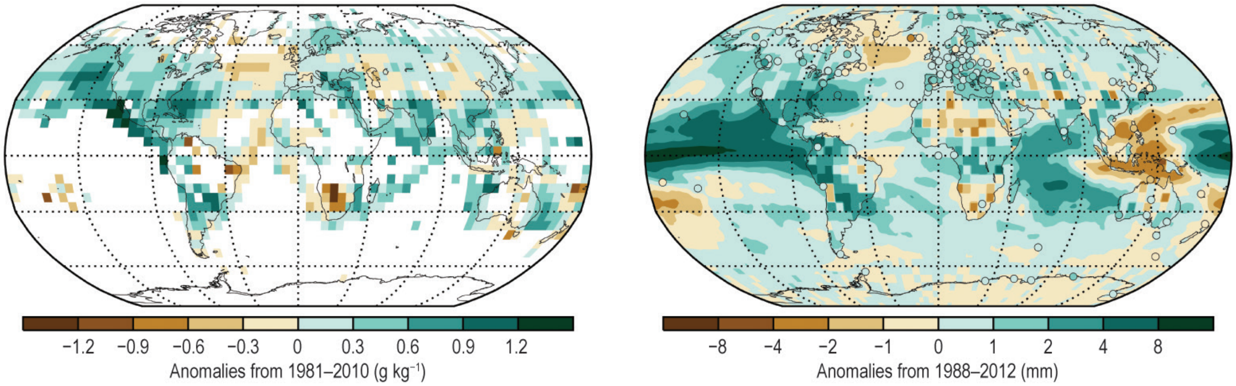

(l) Surface Relative Humidity

(p) Drought (self-calibrating PDSI)

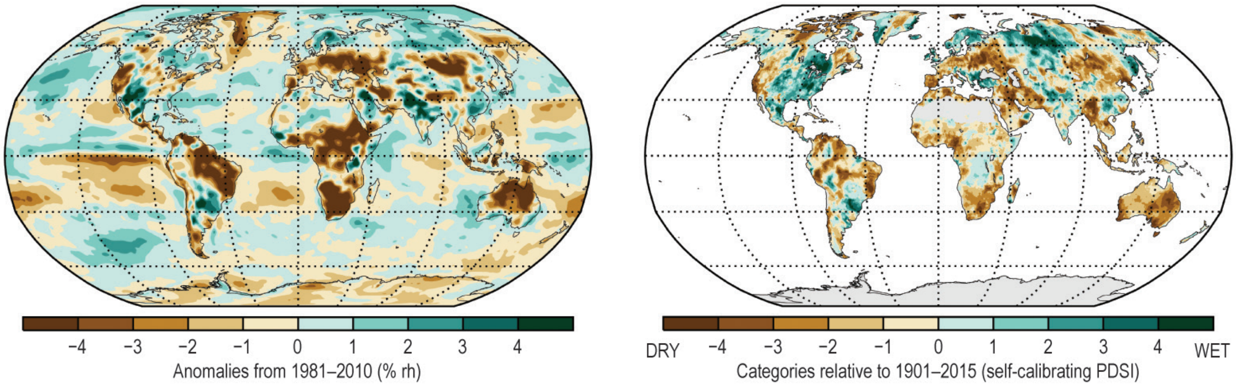

(q) Stratospheric (Total Column) Ozone

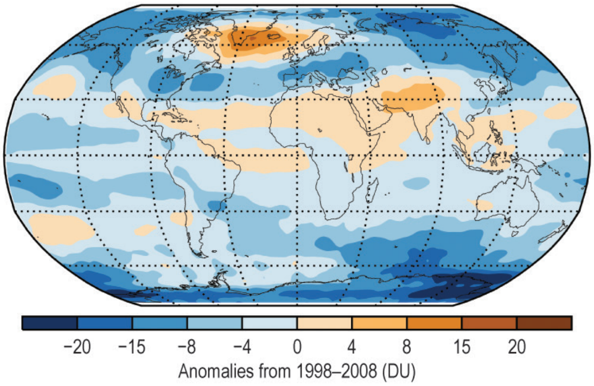

(r) Upper Air (850-hPa) Winds

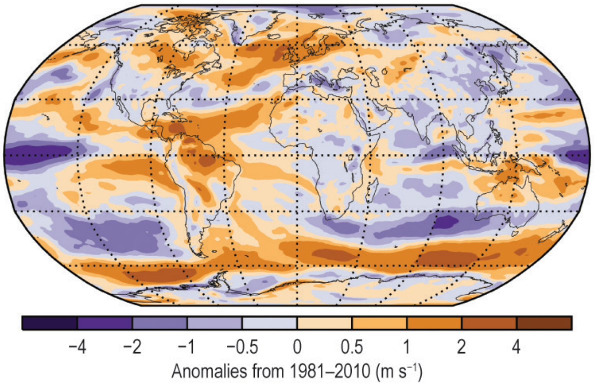

(s) Surface Winds

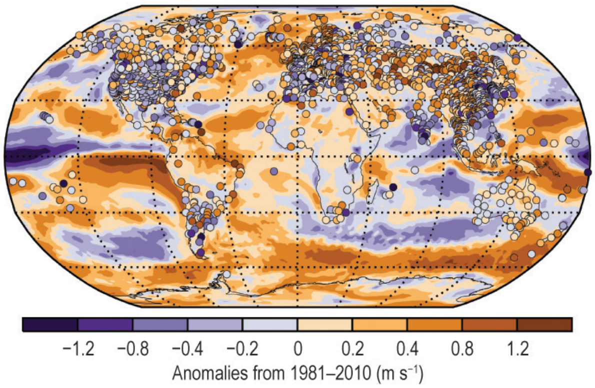

(t) Sea Level Pressure

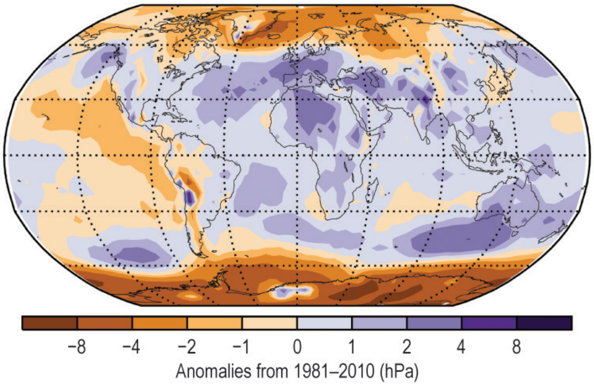

(u) OMI/MLS Tropospheric Column Ozone

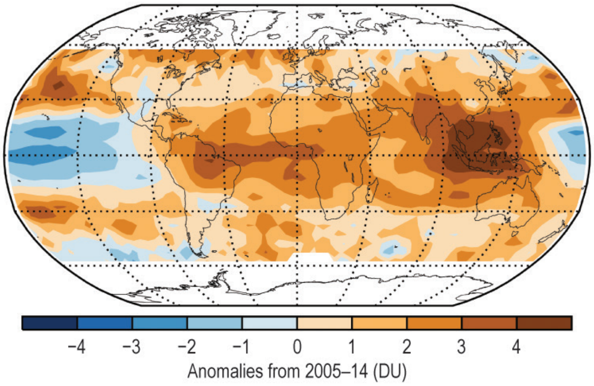

(v) Total Aerosol

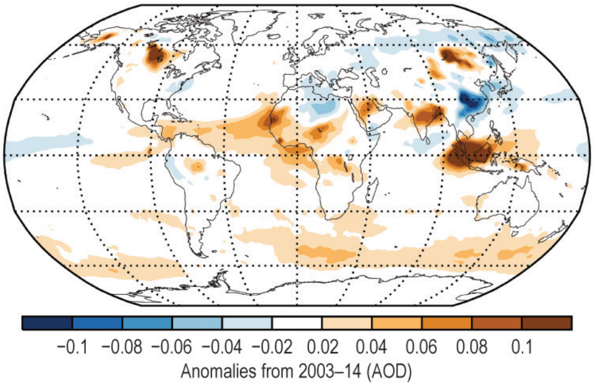

(w) Dust Aerosol

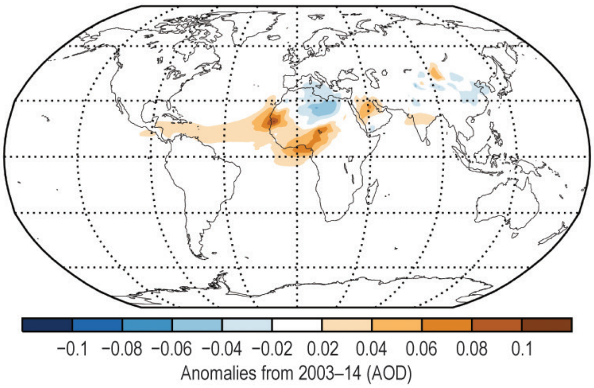

(x) Biomass Burning Aerosol

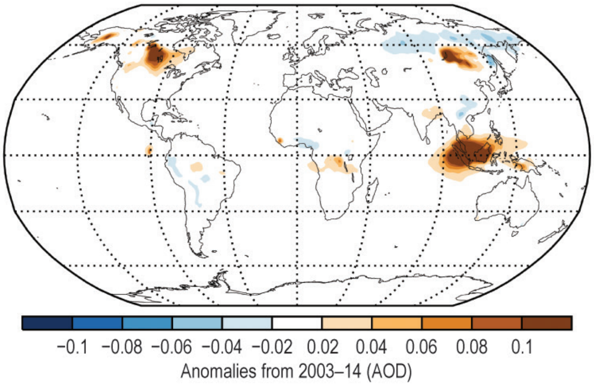

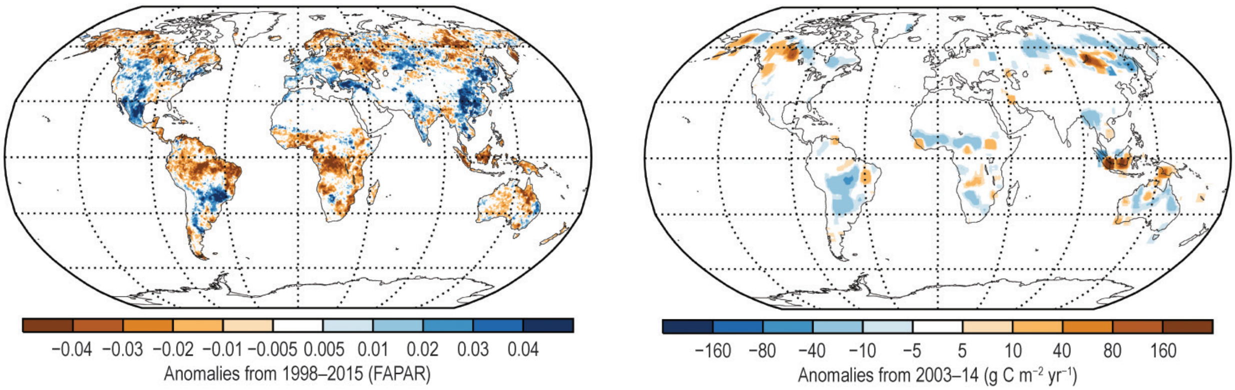
(y) Fraction of Absorbed Photosynthetically Active Radiation

(ab) Carbon Emissions from Biomass Burning

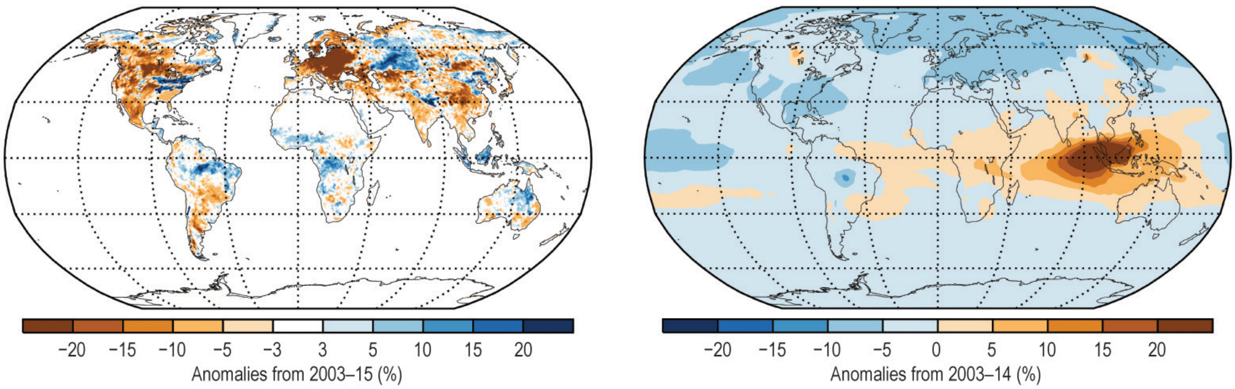
(z) Land Surface Albedo in the Visible

(ac) Carbon Monoxide

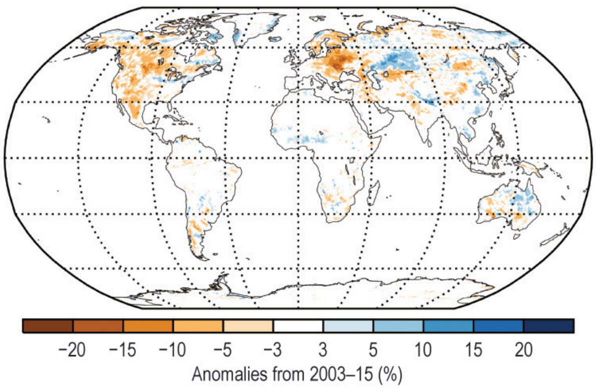
(aa) Land Surface Albedo in the Near-Infrared

PLATE 2.1. (a) ERA-Interim lower stratospheric temperature; (b) ERA-Interim lower tropospheric temperature; (c) NOAA/NCEI surface temperature (contoured) and lake temperatures (circles); (d) GHCNDEX warm day threshold exceedance (TX90p); (e) GHCNDEX cool day threshold exceedance (TX10p); (f) ESA CCI soil moisture; (g) GRACE 2015 difference from 2014 water storage; (h) GPCP precipitation; (i) ELSE system runoff; (j) ELSE system river discharge; (k) HadISDH (land) and NOCSv2.0 (ocean) surface specific humidity; (l) ERA-Interim surface relative humidity; (m) PATMOS-x cloudiness; (n) HIRS upper tropospheric humidity; (o) Microwave radiometer retrievals (ocean), COSMIC GPS-RO data (land), and GNSS (circles, land) total column water vapor; (p) sc-PDSI drought annual average 2015 anomaly; (q) GOME-2 (using GOME, SCIAMACHY, and GOME-2 for the climatology) stratospheric (total column) ozone; (r) ERA-Interim 850-hPa wind speed; (s) ERA-Interim (worldwide grids) and HadISD (points) surface wind speed; (t) HadSLP2r sea level pressure; (u) Tropospheric ozone; (v) CAMS total aerosol optical depth; (w) CAMS aerosol optical depth from dust; (x) CAMS aerosol optical depth from biomass burning; (y) SeaWiFS/MERIS/MODIS fraction of absorbed photosynthetically active radiation (FAPAR); (z) Surface visible-light albedo from MODIS White Sky broadband; (aa) Surface near-infrared albedo from MODIS White Sky broadband; (ab) GFASv1.3 carbonaceous emissions from biomass burning; (ac) CAMS total column CO anomalies.

b. Temperature

1) Surface temperature—A. Sánchez-Lugo, C. Morice, and P. Berrisford

The 2015 global land and ocean temperature set new records, exceeding the previous records set in 2014 (and 2010 depending on the in situ dataset) by a wide margin of 0.13°–0.18°C. Much-warmer-than-average conditions across much of the world's surface and a strong El Niño contributed to the highest temperature since records began in the mid- to late 1800s, according to four independent in situ analyses (NASA–GISS, Hansen et al. 2010; HadCRUT4, Morice et al. 2012; NOAAGlobalTemp, Smith et al. 2008; JMA, Ishihara 2006). The 2015 globally averaged surface temperature was 0.42°–0.46°C (Table 2.1) above the 1981–2010 average. Note that ranges of temperature anomalies provided in this summary are ranges of best estimates for the assessed in situ datasets. These ranges do not include additional uncertainty information from each in situ analysis, which can be found in Table 2.1.

The last time a record high temperature surpassed the previous record by such a wide margin was 1998, which surpassed the previous 1997 record by 0.12°–0.16°C. Similar to 2015, a strong El Niño developed during the latter half of 1997, reaching its maturity during the first part of 1998 (see Sidebar 1.1). The presence of El Niño typically increases concurrent global temperatures and those in the year following its onset.

The year 2015 also marked the first time the global average surface temperature reached more than 1°C above the average of the mid- to late 19th century, a period in which temperatures are commonly taken to be representative of pre industrial conditions. The best-estimate global average surface temperatures were 1.03°–1.09°C above the mid- to late 19th century average in assessed datasets. Fourteen of the 15 warmest years on record have occurred since the beginning of the 21st century, with 1998 the only exception (ranking between third and eighth warmest year, depending on the dataset).

Every estimate of global average temperature has inherent uncertainty. The main sources of uncertainty in observational datasets tend to be associated with changes in measurement practices and with sparse spatial sampling, both of which can vary with time. When taking into consideration the estimated uncertainty of the global land and ocean annual temperature in the annual ranking, following the method of Arguez et al. (2013), it is virtually certain that 2015 was the warmest year since records began, with a probability >99%, according to the NOAAGlobalTemp dataset (see Arguez and Applequist 2015).

The near-surface temperature analyses assessed here are derived from air temperatures observed at weather stations over land and sea surface temperatures (SST) observed from ships and buoys. While each analysis differs in methodology, all four analyses are in close agreement (Fig. 2.1). Plate 2.1c and Online Figs. S2.1, S2.2, and S2.3 show the differences between the datasets, which are mainly due to how each methodology treats areas with little to no data and how each analysis accounts for changes in measurement methods [for more details see Kennedy et al. (2010); Hansen et al. (2010); and Huang et al. (2015)].

Global average surface air temperatures are also estimated using reanalyses, which blend information from a numerical weather prediction model with observations. Reanalysis produces datasets with uniform spatial and temporal coverage, but suffers from model biases and problems arising from time variations in amount and/or quality of assimilated observations. Surface temperatures from reanalyses are consistent with observations in regions of good observational coverage at the surface, due in part to the large volumes of assimilated observations (e.g., more than 40 billion to date in the ERA-Interim reanalysis).

According to ERA-Interim (Dee et al. 2011), the 2015 globally averaged, analyzed 2-m temperature was the highest since records began in 1979. The

Table 2.1. Temperature anomalies (°C) and uncertainties (where available) for 2015 (base period: 1981–2010). The uncertainties indicate the scope of the range around the central value. For ERA-Interim, the values shown are the analyzed 2-m temperature anomalies (uncorrected). Note that the land values computed for HadCRUT4 used the CRUTEM.4.4.0.0 dataset (Jones et al. 2012), the ocean values were computed using the HadSST.3.1.1.0 dataset (Kennedy et al. 2011a, 2011b), and the global land and ocean values used the HadCRUT4.4.0.0 dataset. Uncertainty ranges are represented in terms of a 95% confidence interval, with the exception of JMA which has a 90% confidence interval.

Global	NASA–GISS	HadCRUT4	NOAA-Global Temp	JMA	ERA-Int
Land	+0.64	+0.66±0.14	+0.72±0.18	+0.70	+0.65
Ocean	+0.36	+0.39±0.07	+0.37±0.16	+0.33	+0.28
Land and Ocean	+0.44±0.05	+0.45 ±0.08	+0.46 ±0.08	+0.42±0.13	+0.38

temperature was 0.38°C above the 1981–2010 average (Table 2.1) and 0.10°C above its previous record set in 2005. The magnitude of the anomaly would be larger had the temperature analyses been corrected for changes in the source of the prescribed SST, which was uniformly cooler by about 0.1°C relative to HadCRUT4 from 2002 onwards (Simmons and Poli 2014).

The only land areas with temperatures below average, according to the in situ datasets, were parts of southern South America, eastern Canada, Greenland, and Antarctica. Overall, the globally averaged annual temperature over land [including the land-only Berkeley Earth analysis (Rohde et al. 2013)] was 0.61°–0.72°C above average—the highest on record. This exceeds the previous 2007 record (and, depending on the in situ dataset, 2010) by 0.12°–0.26°C.

The strong El Niño maturing during 2015 resulted in record high SSTs across much of the tropical Pacific Ocean. However, areas in the North Atlantic, South Pacific, and the waters south of South America experienced below-average conditions (Plate 2.1c). The globally averaged annual temperature across the oceans was 0.33°–0.39°C above average—the highest on record according to the in situ datasets, surpassing the previous record set in 2014 by 0.10°–0.12°C (see section 3b for more detailed SST information).

Similarly, ERA-Interim for 2015 shows warmer-than-average conditions over many, but not all, regions of the world (Online Fig. S2.1). The average analyzed 2-m temperature over land was 0.65°C above average (0.09°C above the previous 2007 record), and, over the oceans, it was 0.28°C above average (0.10°C above the previous 2005 record).

2) Lower and midtropospheric temperatures—

J. R. Christy

The 2015 globally averaged annual temperature of the lower troposphere (LT, the bulk atmosphere below 10 km altitude or roughly the lower 70% by mass) was approximately +0.3°C above the 1981–2010 mean. This placed 2015 first to fourth warmest of the past 58 years, depending on the dataset, and was on average about 0.2°C cooler than the warmest year, 1998, varying from just above the 1998 value in two radiosonde datasets to 0.1°–0.3°C below in the remaining datasets (Fig. 2.2).

Direct measurement of the LT bulk temperature utilizes radiosonde datasets since 1958, complemented by satellites since late 1978. The datasets are described in Christy (2015) with new additions of the UNSW radiosonde dataset from Sherwood and Nishant (2015) and, for use in the tropical midtroposphere, two satellite datasets with similar construction methods [NOAA (Zhou and Wang 2011) and UW (Po-Chedley et al. 2015)]. Previously utilized datasets from UAH and RSS have been updated (UAHv6.0, Spencer et al. 2016 submitted to *Asia-Pacific J. Atmos. Sci.;* RSSv4.0 for the midtroposphere, Mears and

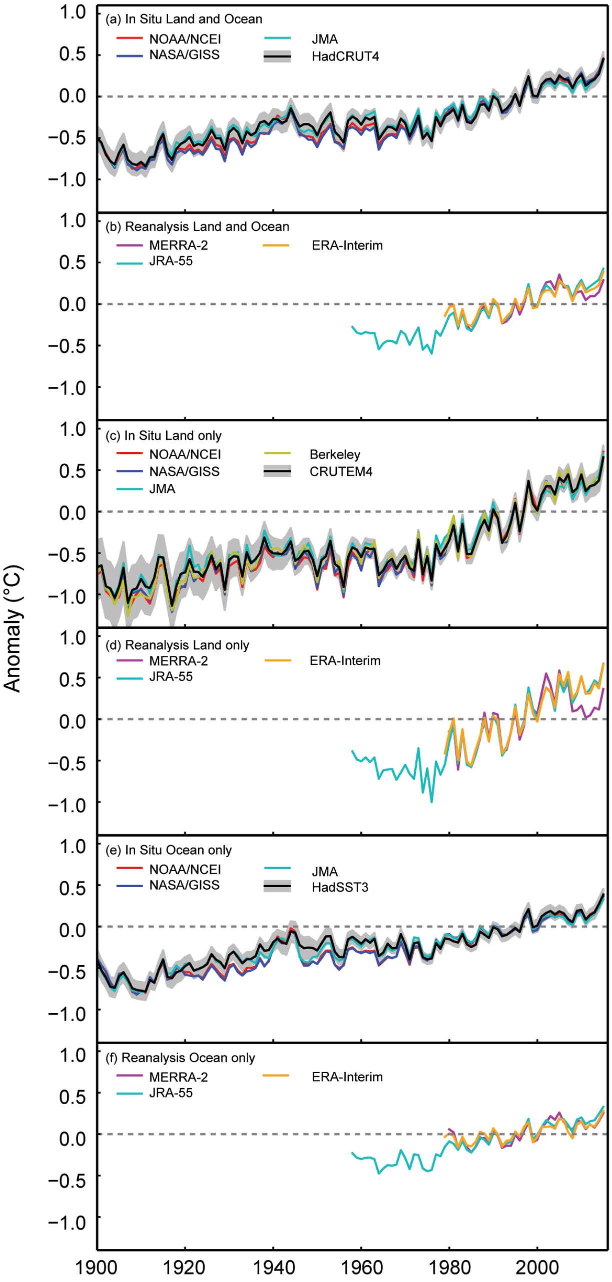

Fig. 2.1. Global average surface temperature anomalies (°C, 1981–2010 base period). In situ estimates are shown from NOAA/NCEI (Smith et al. 2008), NASA-GISS (Hansen et al. 2010), HadCRUT4 (Morice et al. 2012), CRUTEM4 (Jones et al. 2012), HadSST3 (Kennedy et al. 2011a, b), JMA (Ishihara 2006), and Berkeley Earth (Rohde et al. 2013). Reanalyses estimates are shown from ERA-Interim (Dee et al. 2011), MERRA-2 (Gelaro et al. 2016; Bosilovich et al. 2015), and JRA-55 (Ebita et al. 2011).

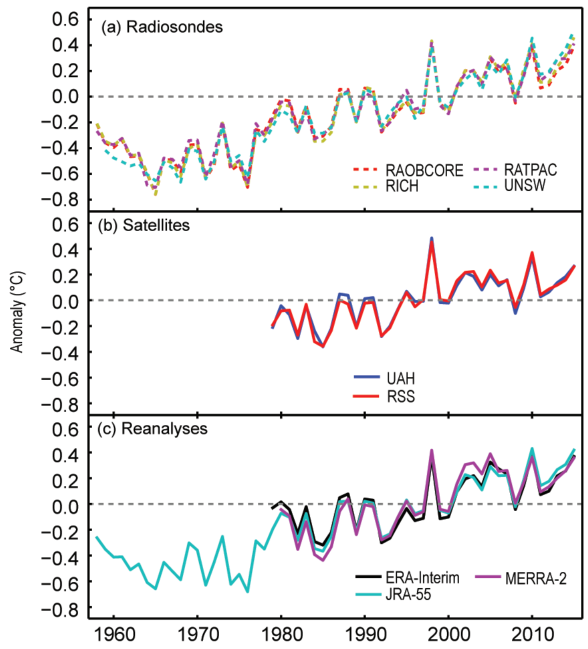

Fig. 2.2. Global average lower tropospheric temperature annual anomalies (°C; 1981–2010 base period) for the MSU LT equivalent layer. (a) Radiosonde: RATPAC (Free et al. 2005; 85 stations), RAOBCORE and RICH (Haimberger et al. 2012; 1184 stations), and UNSW (Sherwood and Nishant 2015, 460 stations). (b) Satellites: UAHv6.0 (Spencer et al. 2016 submitted to *Asia-Pacific J. Atmos Sci*) and RSSv3.3 (Mears and Wentz 2009). (c) Reanalyses: ERA-Interim, MERRA-2, and JRA-55 are shown as described in Fig. 2.1.

Wentz 2016). In addition, three reanalyses products are also shown. There is close agreement in the interannual variability between all products; ERA-Interim is used here to provide the spatial depictions (Plate 2.1b and Online Fig. S2.4).

The global LT anomaly at any point in time is closely tied to the phase of the El Niño–Southern Oscillation (ENSO). The year 2015 is analogous to 1997 in that a warm ENSO phase began and peaked in the Pacific Ocean. The year 1998 was approximately +0.5°C warmer than 1997, and thus a comparison of 2016 with 1998 will indicate how similar the ENSOs evolved, having been quite similar for 1997 vs. 2015.

Regionally, warm anomalies extended from the Arctic equatorward to the eastern Pacific and much of Europe. The midlatitude belt in the Southern Hemisphere was mostly warmer than average. Cooler-than-average temperatures occupied northeast North America–Greenland, portions of Russia, and the far Southern Ocean (Plate 2.1b). The latitude–time depiction of the LT temperatures beginning in 1979 indicates tropical warming that is particularly strong during 2015, associated with the ongoing El Niño (Online Fig. S2.4).

The long-term global LT trend based on radiosondes (starting in 1958) is +0.15° ± 0.02°C decade^{-1} and based on both radiosondes and satellites (starting in 1979) is +0.13° ± 0.03°C decade^{-1}. The range represents the variation among the different datasets, which then serves as an estimate of structural uncertainty in Fig. 2.2. When taking into account the magnitude of the year-to-year variations, there is a statistical confidence range of ± 0.06°C decade^{-1}, meaning that the trends are significantly positive. Major volcanic events in 1963, 1982, and 1991 contributed to cooler temperatures during the early part of the LT record, especially in the satellite era, thus increasing the upward trend to some extent.

With this edition we introduce the midtropospheric temperature (MT, surface to around 70 hPa) product for the tropical atmosphere (Fig. 2.3). The MT profile extends higher than that of LT, entering the stratosphere, but only slightly in the tropics where the tropopause is at approximately 16-km altitude. The dominant signal of this product is in the mid- to-upper troposphere, thus capturing the layer in the tropics which represents the maximum response to forcing (e.g., increased greenhouse gases, warm surface waters from El Niño, volcanic cooling, etc.). MT is constructed from the Microwave Sounding Unit (MSU) channel 2 and the Advanced MSU

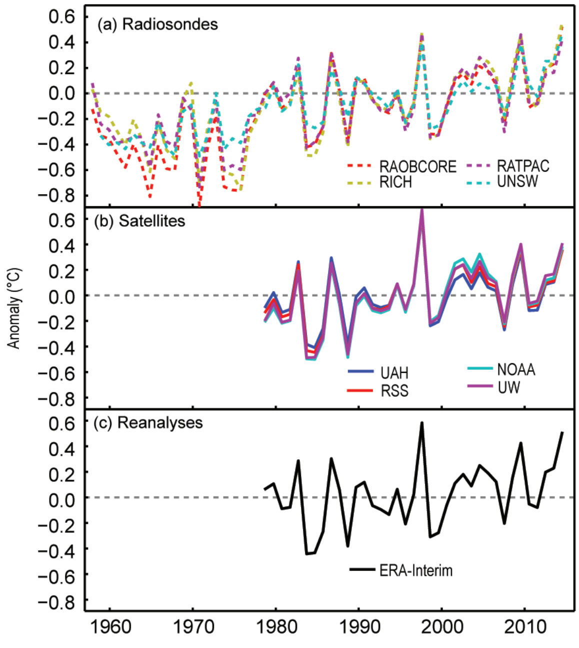

Fig. 2.3. Tropical (20°S–20°N) anomalies of midtropospheric temperature relative to the 1981–2010 base period. Data sources are as described in Figs. 2.1 and 2.2 with the addition of NOAA (Zhou and Wang 2011), UW (Po-Chedley et al. 2015) and RSSv4.0 (Mears and Wentz 2016).

channel 5 (Christy et al. 2003). MT tropical trends are influenced by lower stratospheric cooling by approximately 0.03°–0.04°C decade^{-1}, which is fully accounted for in comparison with theory.

Examining the various datasets of tropical MT trends (1979–2015), there are two clusters of results: +0.08°C decade^{-1} (most radiosonde datasets and satellite UAH) and +0.12°C decade^{-1} (RICH radiosonde dataset and satellite datasets of RSS, NOAA, and UW; Table 2.2). A significant difference between UAH and the other satellite datasets is evident over the oceans. This suggests the disagreement is due to differing assumptions regarding basic calibration issues rather than corrections for the diurnal drift of the spacecraft, and is an active area of research.

The MT time series and trends (Fig. 2.3, Table 2.2) through 2015 continue the characteristic noted in past *State of the Climate* reports that observed MT trends tend to be below estimates anticipated from basic lapse-rate theory—the theory that indicates a magnification of trend with height (Christy 2014). This is especially true in the tropics where theory suggests amplification by a factor of 1.4 ± 0.2 of the mid tropospheric trend over the surface trend. The range of trends for 1979–2015 from the different radiosonde datasets is +0.07° to +0.11°C decade^{-1} and from satellites is +0.07° to +0.14°C decade^{-1} compared with the tropical surface trend (average of NOAAGlobalTemp and HadCRUT4) of +0.12°C decade^{-1}. The median trend of all observational datasets examined here is between +0.09 and 0.10°C decade^{-1}. Thus, the current tropical MT/surface ratio from observations since 1979 (0.8 ± 0.3) continues to be less than theory.

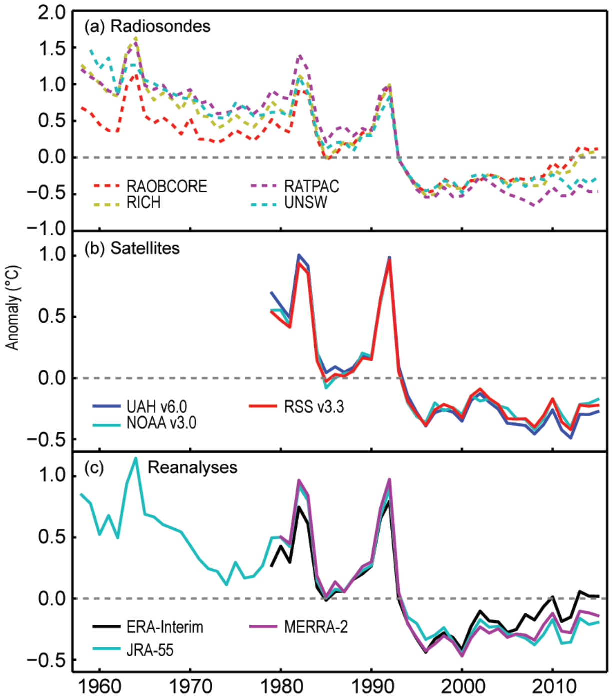

Fig. 2.4. Global mean annual temperature anomalies of the lower-stratosphere temperatures derived from (a) radiosonde, (b) satellite, and (c) reanalysis. Anomalies are from the 1981–2010 mean. Data sources are as described in Figs. 2.1 and 2.2, additional data sources: NOAA (Zhou and Wang 2010).

Table 2.2. Linear trends (°C decade^{-1}) in lower tropospheric (LT) and midtropospheric (MT) temperatures. The tropics region spans 20°S–20°N.

	Global LT		**Tropics MT**	
Start Year	**1958**	**1979**	**1958**	**1979**
Radiosondes				
RAOBCORE	+0.15	+0.13	+0.13	+0.08
RICH	+0.15	+0.15	+0.10	+0.11
RATPAC	+0.15	+0.15	+0.09	+0.07
UNSW	+0.17	+0.16	+0.10	+0.07
Satellites				
UAHv6.0	x	+0.11	x	+0.07
RSSv3.3	x	+0.12	x	+0.09
RSSv4.0	x	x	x	+0.14
NOAAv3.0	x	x	x	+0.13
UWv1.0	x	x	x	+0.12
Reanalyses				
ERA-I	x	+0.12	x	+0.08
JRA-55	+0.16	+0.15	x	+0.08
MERRA	x	+0.19	x	+0.16

3) LOWER STRATOSPHERIC TEMPERATURE—C. S. Long and J. R. Christy

The globally averaged temperature in the lower stratosphere (TLS) for 2015, as measured by radiosonde and satellite and analyzed by reanalyses, ranged from slightly above to approximately 0.5°C below the 1981–2010 climatology (Fig. 2.4). All TLS estimates agree that globally 2015 was about the same as 2014. This year's persistence of last year's annual temperatures only slightly impacted the near-neutral to very gradual warming trend observed from 1995 to present.

Despite similarity in the global average value, spatial patterns are different than those of 2014. The annual averaged temperature analysis (Plate 2.1a) shows negative anomalies in both hemispheres' polar latitudes. The Arctic negative anomalies extended into Siberia but positive anomalies were centered near Iceland. This strong positive anomaly was mirrored in the lower troposphere and surface by a strong cool anomaly (Plates 2.1b,c). The Antarctic had negative anomalies throughout the entire zone. In lower latitudes, positive anomalies generally prevailed over the Atlantic and eastern Asia, with negative anomalies over the central Pacific. These anomalies were related to the El Niño that grew during the latter half of 2015. The northern polar region oscillated between cold and warm anomalies for the first five months of 2015 (Online Fig. S2.5). The southern polar region was anomalously cold from August through December. These negative temperature anomalies coincided with the large and persistent ozone hole for 2015 (section 2g4). The tropical warm anomalies were a result of the thermal response to the descending quasi-biennial oscillation (QBO) westerlies during 2015 and the upper troposphere warming from the El Niño in the latter half of 2015.

A cooler stratosphere is consistent with a warmer troposphere in the case of rising greenhouse gases, as more outgoing energy is trapped in the troposphere. The TLS is a weighted layer-mean temperature of the part of the atmosphere observed by specific channels from satelliteborne microwave sounding instruments. It ranges from around 200–20 hPa (12–27 km) and is entirely in the lower stratosphere polewards of 35°. But equatorward of this, it extends into the upper troposphere, which needs to be accounted for when assessing latitudinal trends. For further details see Long and Christy (2015).

All radiosonde datasets (RATPAC, RAOBCORE, RICH, NSW) show a cooling trend in the lower stratosphere from 1958 to 1995. However, after 1995 there is not much of a trend to the present (Fig. 2.4). The pre-1995 cooling trend is only interrupted by several volcanoes [Agung (1963), El Chichón (1982), and Mt. Pinatubo (1991)], which imparted a warm pulse for about two years following each eruption. The satellite MSU channel 4 datasets (RSS, NOAA, and UAH) and four recent reanalysis datasets (CFSR; ERA-Interim; JRA-55; MERRA-2) also show general agreement with the radiosonde time series. Table 2.3 provides the trends for various time periods for the radiosondes, satellites, and reanalyses. There is variability among the datasets in the cooling trend from 1979 to 1995, with RATPAC having the greatest cooling of the radiosonde datasets and MERRA-2 having the greatest cooling of the reanalyses, while ERA-Interim and JRA-55 have the least cooling. The post-1995 trends also vary considerably. All three satellite, JRA-55, RATPAC, and NSW trends are near neutral. The ERA-Interim and MERRA-2 reanalyses, RICH, and RAOBCORE have a slightly positive trend. As shown in Long and Christy (2015), the trends discussed above are not uniformly distributed across all latitudes, rather there is considerable variability with latitude.

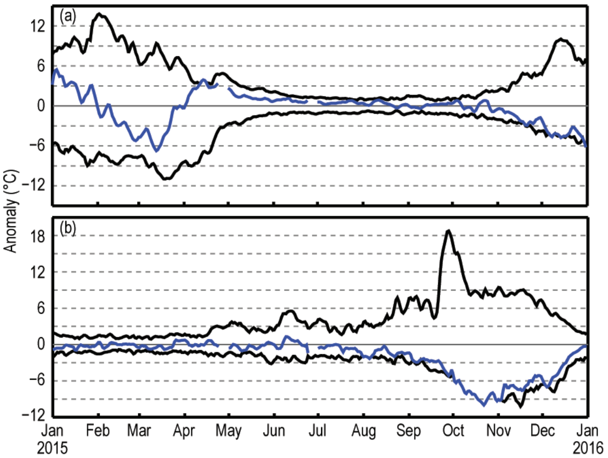

Fig. 2.5. Daily time series (blue lines) for 2015 lower stratosphere temperatures from the CFSR (Saha et al. 2010a) for the (a) northern high latitudes (60°–90°N) and (b) southern high latitudes (60°–90°S). The 1979–2015 daily maximum and minimum temperatures for each latitude region are shown in black.

Figure 2.5 shows time series of daily TLS anomalies for the 60°–90°N and 60°–90°S bands for 2015. The southern high latitudes were exceptionally cold from August through December 2015. Monthly mean height analyses show that the polar circulation in late 2015 was centered over the South Pole (not shown). Additionally, wave activity was minimal, keeping the circulation very zonal and cold. The low temperatures and persistent circulation aided the destruction of ozone, resulting in a larger ozone hole than in recent years (section 2g4). In the northern high latitudes, a few midwinter warmings affected the upper stratosphere but did not propagate down into the middle or lower stratosphere. A final warming in mid-March propagated down to the TLS region and increased the temperatures in the polar zone (Fig. 2.5). This warming is classified as a "final" warming as the atmospheric temperatures and circulation did not return to a winter pattern but continued to transition to a summer pattern. During the boreal autumn and early winter, Arctic TLS temperatures were well below normal.

Table 2.3. Computed trends (°C decade^{-1}) for radiosonde, satellite, and reanalysis data for the periods: 1958–95, 1979–95, 1995–2015, and 1979–2015. 1995 is chosen as an inflection point distinguishing the earlier downward trend from the near-neutral trend of recent years.

Global (82.5°N–82.5°S) TLS Temperature Anomaly Trends (1981–2010 base period)				
Dataset	**1958–95**	**1979–95**	**1995–2015**	**1979–2015**
Radiosonde				
RAOBCORE	−0.117	−0.306	0.260	−0.208
RICH	−0.282	−0.484	0.219	−0.278
RATPAC	−0.257	−0.649	−0.010	−0.467
UNSW	−0.330	−0.474	0.039	−0.317
Satellite				
RSS	×	−0.336	−0.012	−0.261
STAR	×	−0.364	−0.002	−0.262
UAH	×	−0.399	−0.046	−0.312
Reanalysis				
CFSR	×	−0.652	0.106	−0.348
ERA-Interim	×	−0.187	0.199	−0.119
JRA-55	×	−0.235	0.018	−0.217
MERRA-2	×	−0.300	0.171	−0.199

4) Lake surface temperatures—R. I. Woolway, K. Cinque, E. de Eyto, C. L. DeGasperi, M. T. Dokulil, J. Korhonen, S. C. Maberly, W. Marszelewski, L. May, C. J. Merchant, A. M. Paterson, M. Riffler, A. Rimmer, J. A. Rusak, S. G. Schladow, M. Schmid, K. Teubner, P. Verburg, B. Vigneswaran, S. Watanabe, and G. A. Weyhenmeyer

Lake summer surface water temperatures (LSSWT) in 2015 strongly reflected the decadal patterns of warming noted in the scientific literature. Northern Hemisphere summer refers to July–September whereas Southern Hemisphere summer refers to January–March. A recent worldwide synthesis of lake temperatures (O'Reilly et al. 2015) found that LSSWTs rose by, on average, 0.034°C yr^{-1} between 1985 and 2009, ~1.4 times that of the global surface air temperature (SAT) in general. Data from lakes in various regions collated here show that during 2009–15 lake temperatures continued to rise.

During 2015, LSSWT of many lakes exceeded their 1991–2010 averages by 1°C or more (Online Fig. S2.6; Plate 2.1c). Strong warm anomalies in LSSWT were most prominent in central Europe [Austria, Switzerland, and Poland (data from the Institute of Meteorology and Water Management, Poland)], where anomalies above 1°C were recorded. The hot central European summer (JJA) of 2015 (sections 2b6 7f, and Sidebar 7.1) is reflected in relatively high mean LSSWTs in three Austrian lakes (Mondsee, Neusiedler See, Wörthersee; Fig. 2.6; Online Fig. 2.6) with anomalies up to +1.6°C. Similarly, satellite-based LSSWT anomalies of 25 European lakes in and near the Alps were in excess of 1.0°C in 2015 (Fig. 2.7a), the second warmest anomaly year since the record summer of 2003 (Beniston 2004). High LSSWTs were also observed in other regions of the world (Plate 2.1c; Online Fig. 2.6), with anomalies for lakes in Seattle [Washington (state), U.S.], for example, up to +1°C in 2015.

LSSWTs are influenced by a combination of broad climatic variability and local characteristics, so regional and subregional differences in LSSWTs are common. LSSWTs in Britain and Ireland during 2015 were ~0.6°C below average, in contrast to central Europe. This likely reflects cool anomalies in SAT in early and mid-2015 (e.g., www.met.ie/climate/MonthlyWeather/clim-2015-ann.pdf).

Although the Great Lakes (United States and Canada) have warmed faster than SAT in recent decades, the 2015 LSSWTs were relatively cool. This is attributable to above-average winter ice cover during 2014/15, which shortened the warming season. The annual maxima of percent ice cover (Great Lakes Environmental Research Laboratory; www.glerl.noaa.gov/) in 2014 (92.5%) and 2015 (88.8%) were substantially above the 1973–2015 average (53.2%). These were the first consecutive high-ice-cover years since the 94.7% maximum ice coverage recorded in 1979. The strong El Niño conditions of 2015 lessen the chance that 2016 will imitate 2014 and 2015.

Despite these recent cooler LSSWTs, the average warming rate for the Great Lakes is approximately 0.05°C yr^{-1} (1979–2015). This rate contrasts with the Dorset lakes in Ontario, Canada (surface areas <100 ha), which do not show a statistically significant trend in LSSWT between 1980 and 2015. In 2015, LSSWT anomalies in these lakes were ~+0.6°C. These lakes display large interannual variation in LSSWT, mainly reflecting interannual differences in SAT, with strong agreement in high and low years.

The relationship between SAT and LSSWT can be complicated by several processes. For Lake Erken, Sweden, LSSWT is strongly influenced by water column mixing and precipitation, leading to a relatively weak relationship between SAT and LSSWT. The LSSWT of New Zealand's largest lake, Lake Taupo, is thought to be influenced by interannual variation in geothermal heating (de Ronde et al. 2002) and shows no significant trend. Furthermore, an analysis of the 47-year record (1969–2015) of LSSWT from Lake Kinneret, Israel, reveals warming of ~1.65°C over the period (~0.036°C yr^{-1}). Two factors explain most of the variability ($r^2 = 0.67$): SAT and water levels (Rimmer et al. 2011; Ostrovsky et al. 2013).

In recent years there has been a strong emphasis on investigating LSSWT warming, with only a few investigations focusing on the winter months (e.g., Dokulil et al. 2014) due to a lack of available data. Winter temperature changes can be quite distinct from LSSWT trends. For example, the regional average warming rate for lakes in Britain and Ireland is substantially higher during winter (0.028°C yr^{-1}; Fig. 2.7b) than in summer (0.018°C yr^{-1}; Fig. 2.7d). Future assessments that focus on all seasons will provide a more complete picture.

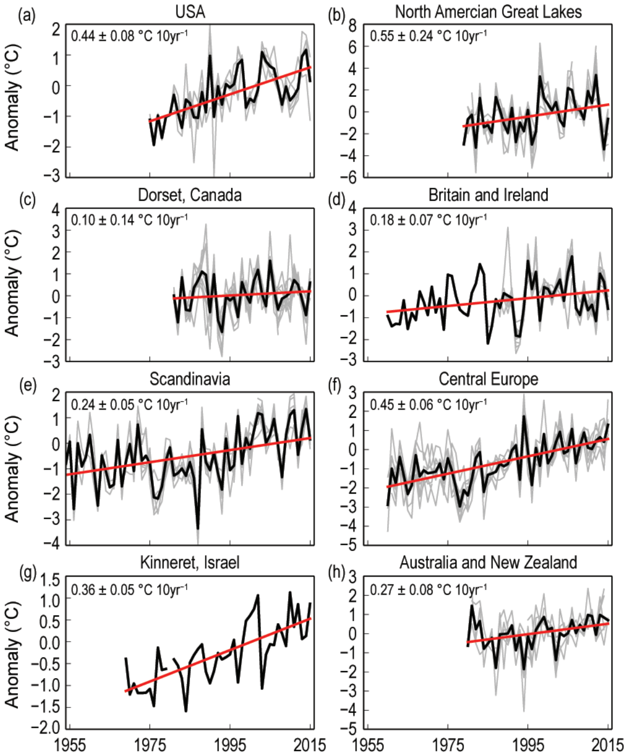

Fig. 2.6. Lake summer (Jul–Sep in Northern Hemisphere, Jan–Mar in Southern Hemisphere) surface water temperature anomalies relative to 1991–2010 for (a) the United States (Washington, Sammamish, Union, and Tahoe); (b) the Laurentian Great Lakes, [Superior (buoys 45001, 45004, 45006), Michigan (buoys 45002, 45007), Huron (buoys 45003, 45008), and Erie (buoy 45005)]; (c) Dorset, Ontario, Canada [Blue Chalk, Chub, Crosson, Dickie, Harp, Heney Plastic, and Red Chalk (East and Main basin)]; (d) Britain and Ireland [Bassenthwaite Lake, Blelham Tarn, Derwent Water, Esthwaite Water, Lough Feeagh, Grasmere, Loch Leven, and Windermere (North and South basins)]; (e) Scandinavia (Erken, Inarijärvi, Kitusjärvi, Lappajärvi, Päijänne, Pielinen, and Saimaa); (f) central Europe (Charzykowskie, Jeziorak, Lubie, Mondsee, Neusiedler See, Wörthersee, and Zurich); (g) Israel (Kinneret); and (h) Australia and New Zealand (Burragorang, Cardinia, Sugarloaf, Taupo, and Upper Yarra). Gray lines indicate the temperature for each individual lake and the thick black line indicates the average lake temperature for the specified region. The trend for the regionally averaged temperatures is shown in red, and the equation describing the change is presented. Note that the warming rates are not comparable among the different regions due to the different time periods shown.

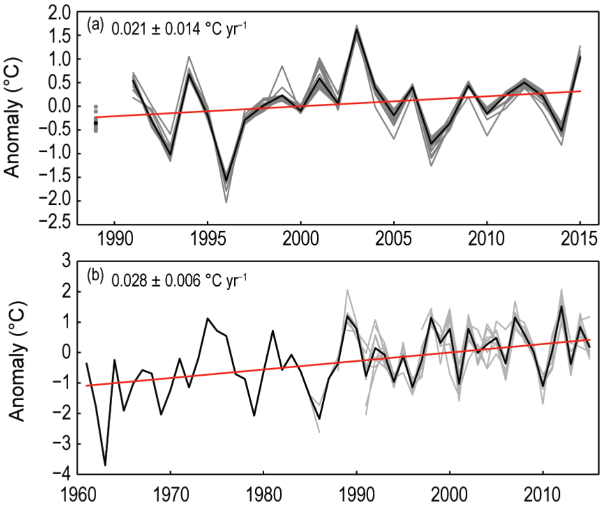

Fig. 2.7. Satellite-derived lake surface water temperature anomalies for (a) summer (Jul–Sep; 1991–2015) for European Alpine lakes (all natural water bodies in or near the Alps larger than 14 km^2; Riffler et al. 2015) and (b) winter (Jan–Mar, 1961–2015) for Britain and Ireland (base period: 1991–2010). Gray lines indicate the temperature for each individual lake and the thick black line indicates the average lake temperature for the region. The trend for the regionally averaged temperatures is shown in red, and the equation describing the change is presented. The lakes included are the same as those shown in Online Fig. 2.6 and Plate 2.1c.

5) LAND SURFACE TEMPERATURE EXTREMES—M. G. Donat, R. J. H. Dunn, and S. E. Perkins-Kirkpatrick

The year 2015 not only set the highest global annual mean temperature on record, it also brought some extreme temperature events, most anomalously warm. Regionally, the frequencies of warm days and warm nights were the highest on record in western North America, parts of central Europe, and central Asia (Plates 2.1d,e). The GHCNDEX dataset (Donat et al. 2013) is used to monitor temperature extremes for 2015. GHCNDEX is a quasi-global gridded dataset of land-based observed temperature and precipitation extremes. A suite of temperature and precipitation extremes indices (Zhang et al. 2011) is first calculated for daily station time series from the GHCN-Daily archive (Menne et al. 2012), before interpolating the indices on global grids. At the time of writing, and similar to Dunn et al. (2015), some of the indices fields have limited spatial coverage for 2015, especially those derived from minimum temperatures across central and eastern Asia, compared to those calculated from maximum temperatures. This limited spatial coverage is related to an excessive number of missing values throughout the year, whereas monthly indices fields are more complete. For more details on the completeness requirements see Zhang et al. (2011).

Here, results for TX90p (frequency of warm days, defined as number of days above the seasonal 90th percentile of daily maximum temperatures over the 1961–90 base period), TX10p (frequency of cool days, defined as number of days with maximum temperatures below the seasonal 10th percentile), TXx (the hottest daily maximum temperature) and TNn (the coldest daily minimum temperature) are presented.

Some of the extreme temperature indices showed global average records during 2015. For example, 2015 had the largest number of warm days (TX90p, 1.8 times compared to the 1961–90 baseline) and the smallest number of cool days (TX10p, 0.6 times the baseline; Fig. 2.8) in the GHCNDEX record going back to 1951. Note the limited spatial coverage of GHCNDEX; however, similar results also indicating the highest number of warm days and lowest number of cool days are found in the ERA-Interim reanalysis that provides complete coverage (see Online Fig. S2.7).

Several regions, including western North America, Europe, and large parts of Asia and Australia, experienced strong warm anomalies, i.e., high frequencies of warm days and low frequencies of cool days, throughout much of the year (Plates 2.1d,e). As GHCNDEX has limited spatial coverage, the ERA-Interim reanalysis product (Dee et al. 2011) is used to provide a more complete picture. ERA-Interim also shows anomalously high numbers of warm days and low numbers of cool days in Africa and large parts of South America, where GHCNDEX lacks coverage, suggesting that most global land areas saw warm anomalies in 2015 (see Online Fig. S2.8).

The first half of the year had some strong cold anomalies over the eastern United States, persisting after the cold winter 2014/15 into spring and even early summer. This resulted in comparatively lower values of warm extremes, though some cold extremes indices only showed cold anomalies during boreal winter (December–February; Fig. 2.9a). Similar behavior was observed during 2013 and 2014.

Notable extreme temperature events included the European summer heat waves (late June–early July and early August); a number of Asian heat waves in, for example, India, Pakistan, and Indonesia; and the warm spring and autumn in Australia, Alaska, and western Russia. Winter (December–February) showed strong warm anomalies over much of the Northern Hemisphere, including large parts of Europe, Asia, and western North America. Most of these events are evident in higher frequencies of warm days and lower frequencies of cool nights (TN10p) and they mainly occurred during the shoulder seasons. The heat waves of Pakistan, India, and Indonesia could not be monitored from GHCNDEX due to lack of coverage. However, results from the ERA-Interim reanalysis (see Online Fig. S2.8) indicate anomalously high annual frequencies of warm days and low frequencies of cold nights over these areas during 2015.

The European heat wave is clearly evident in June–August hottest days (TXx), with anomalies of 4°–5°C, and to a lesser extent in corresponding

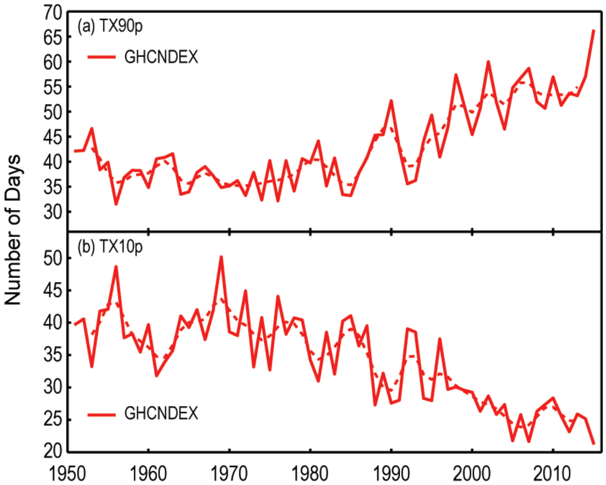

Fig. 2.8. Global average time series of the number of (a) warm days (TX90p) and (b) cool days (TX10p) over land. The dashed line shows a 5-year binomial smoothed time series. (Source: GHCNDEX.)

coldest nights (TNn), with anomalies of 1°–2°C (see Online Fig. S2.9). The frequency of both warm days and nights were also about double the normal for this period (see Fig. 2.9 and Online Fig. S2.7).

The Australian spring (September–November) experienced frequencies of cool nights and warm days well below and above average, respectively (Fig. 2.9), although anomalies in the hottest day and coldest night were not as extreme. The Russian and western North American springs (March–May) were also notably warm, similarly manifested in high frequencies of warm days and nights (Fig. 2.9).

The European autumn (September–November) also had anomalously high frequencies of warm days, whereas over northern North America and Greenland high frequencies of warm nights were more notable. Northern Russia and central Europe experienced warm days 3°–5°C warmer than normal during autumn. Interestingly, the northern central Asia autumn was relatively cold for both warm and cold extremes (Fig. 2.9).

c. *Cryosphere*

1) PERMAFROST THERMAL STATE—J. Noetzli, H. H. Christiansen, M. Gugliemin, V. E. Romanovsky, N. I. Shiklomanov, S. L. Smith, and L. Zhao

The Global Terrestrial Network for Permafrost (GTN-P) brings together long-term records on permafrost from permafrost regions worldwide (Smith and Brown 2009; Biskaborn et al. 2015). The two current observation elements are permafrost temperatures and active layer thickness (ALT). The ALT is the layer that thaws and freezes over the seasonal cycle; it generally increases in warmer conditions.

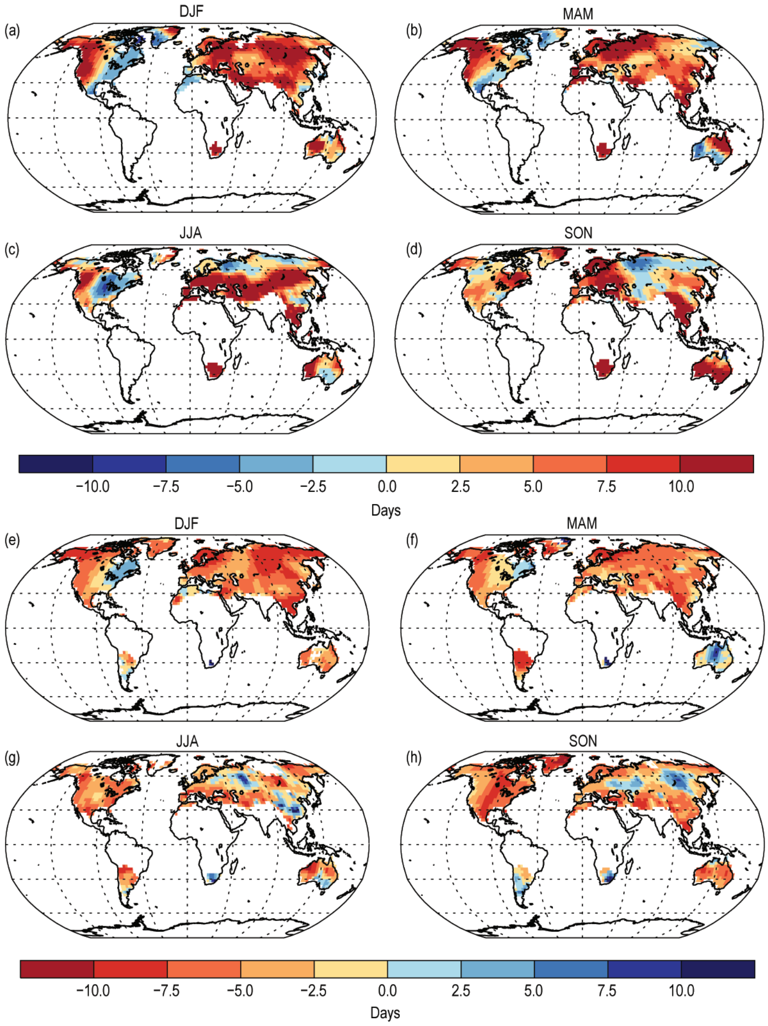

Fig. 2.9. Seasonal anomalies of the frequency of (a–d) warm days (TX90p) and (e–h) cool nights (TN10p) for 2015 relative to the 1961–90 base period. There must be at least two months of data present within each season. (Source: GHCNDEX.)

Permafrost has warmed over the past 2–3 decades, and generally continues to warm across the circumpolar north. Record-high temperatures were observed in 2015 on the Alaskan North Slope region and a noticeable warming has been recorded at several sites in the Alaskan Interior. Similar results have been obtained for northwestern Canada, Russia, and the Nordic regions. ALT for 2015 was generally greater than the long-term average. A detailed discussion of measurement results from Arctic terrestrial permafrost is provided in section 5i. In this section, results from the European Alps, central Asia, and continental Antarctica are summarized.

Mountain permafrost in the European Alps is patchy and its character and thermal conditions are spatially heterogeneous. The majority of permafrost is found between 2600 and 3000 m a.s.l. (Boeckli et al. 2012) in shady debris slopes and rock glaciers. There, permafrost temperatures have been measured for 1–2 decades and are typically above −3°C (Fig. 2.10). Recent installations on very high elevation shaded bedrock slopes show that the highest peaks can be significantly colder. For example, the Aiguille du Midi north face in the Mont Blanc area at 3840 m a.s.l. (see Figs. 2.10a,b), and the Matterhorn summit north slope at 4450 m a.s.l. experience annual mean temperatures near the surface as low as −10°C (Paolo Pogliotti, Environmental

Protection Agency of Valle d'Aosta, 20 February 2015, personal communication). Records measured within the Swiss Permafrost Monitoring Network (PERMOS) during the past 10 to 25 years show a general warming trend at depths to 10 and 20 m, especially over the past seven years (Figs. 2.10a,b). The recent warming is accentuated in 2015, when the highest permafrost temperatures were recorded at most PERMOS sites. This is a cumulative effect of the continuously warm weather conditions in recent years rather than a result of the extremely warm summer 2015. ALT reached new record values in 2015 at many PERMOS sites. Absolute ALT changes depend strongly on surface processes—mainly snow cover duration and thickness—and subsurface ice content (PERMOS 2013). The recent warming of permafrost in the Swiss Alps since 2009 has been accompanied by an increase of rock glacier velocities, as observed at multiple sites within Switzerland.

In the warm permafrost of the higher elevations of central Asia, ground temperatures have increased by up to 0.5°C decade^{-1} since the early 1990s, and a general increase in ALT has been observed (e.g., Zhao et al. 2010). The ground temperature at sites along the Qinghai–Xizang Highway increased between 2004 and 2014 by 0.04°–0.5°C decade^{-1} at 10-m depth, and about 0.01°–0.29°C decade^{-1} at 20-m depth (Fig. 2.10c,d). Based on monitoring results extended by a freezing–thawing index model, the average increase of ALT was about 28 cm decade^{-1} from 1981 to 2015 along the Qinghai–Xizang Highway (Fig. 2.11). The average ALT from 2011 to 2015 in Fig. 2.11 was about 15 cm more than the 2001–10 average. The mean annual air temperature in the Tibetan Plateau region increased at an average rate of 0.68°C decade^{-1} over the past 35 years (Fig. 2.11).

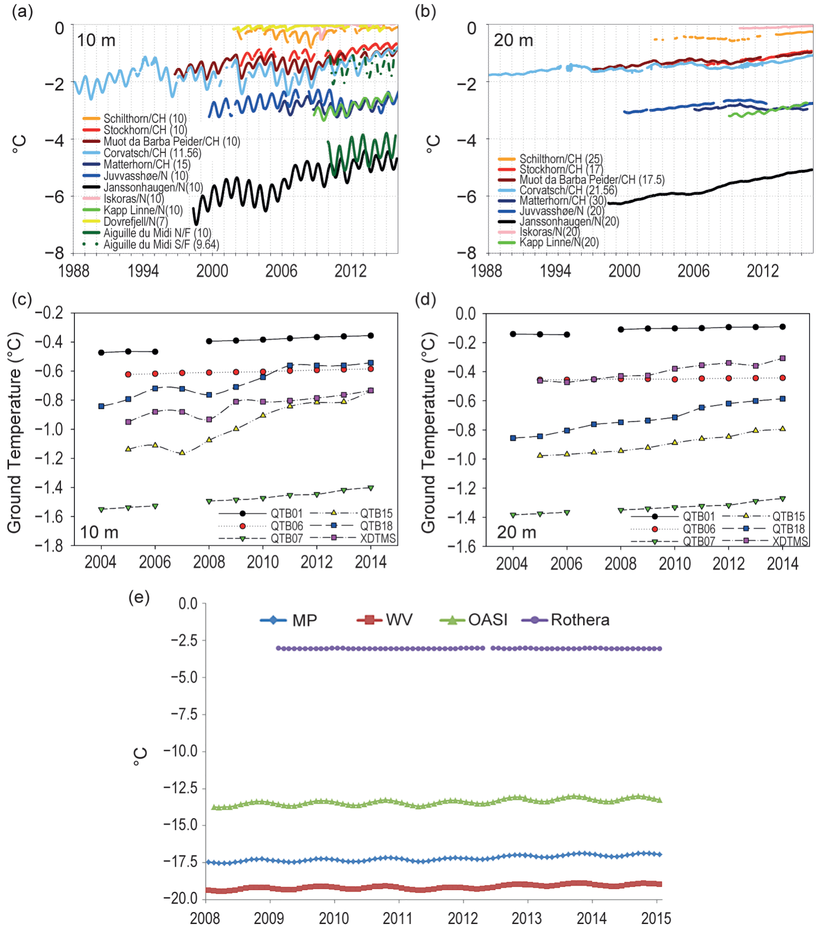

Fig. 2.10. Temperatures measured in permafrost boreholes. Boreholes for central and northern Europe at approximately (a) 10-m and (b) 20-m depth, with actual depths shown in parentheses; along Qinghai–Xizang Highway on the Tibetan Plateau at (c) 10-m and (d) 20-m depth; and (e) in Antarctica at 20-m depth: WV = Wright Valley; MP= Marble Point; OASI in Continental Antarctica; and Rothera in Maritime Antarctica. (Sources: Swiss Permafrost Monitoring Network PERMOS; Norwegian Meteorological Institute and the Norwegian Permafrost Database, NORPERM; EDYTEM/University of Savoie; Cryosphere Research Station on Qinghai–Xizang Plateau, CAS.)

Permafrost temperature at 20-m depth along the latitudinal transect in Victoria Land, continental Antarctica between Wright Valley and OASI (Terra Nova Bay), has increased by about 0.5°C since 2008 (Balks et al. 2016; Fig. 2.10e). This increase is independent of the air temperature, which has been stable since 1960. In contrast, there is no apparent trend in permafrost temperatures in maritime Antarctica (Rothera, Fig. 2.10e) despite recorded air warming in the area. ALT is strongly increasing in the coastal areas of continental Antarctica, between 5 cm year^{-1} at Marble Point (Balks et al. 2016) and 0.8 cm year^{-1} at Boulder Clay (Guglielmin et al. 2014a). In maritime Antarctica, at Signy Island, the active layer has ranged between 124 and 185 cm since 2006 (Guglielmin et al. 2012), while at Livingstone Island between 124 and 145 cm (De Pablo et al. 2014), both without any trends despite air temperatures having increased in this area.

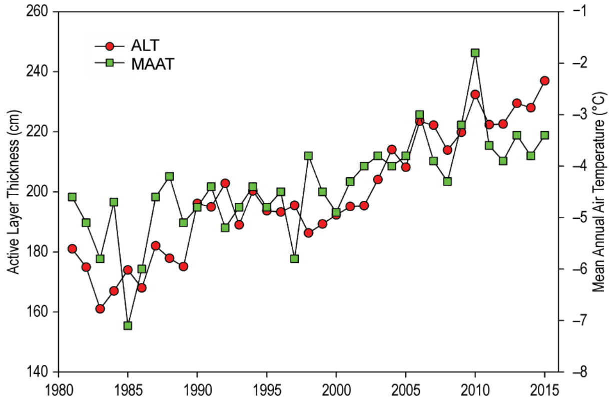

FIG. 2.11. Annually-averaged ALTs and MAATs along Qinghai–Xizang Highway on the Tibetan Plateau (modified after Li et al. 2012 based on new data). (Sources: Cryosphere Research Station on Qinghai–Xizang Plateau, CAS.)

2) NORTHERN HEMISPHERE CONTINENTAL SNOW COVER EXTENT—D. A. Robinson

Annual snow cover extent (SCE; Table 2.4; Fig. 2.12) over Northern Hemisphere (NH) lands averaged 24.6 million km² in 2015. This is 0.5 million km² less than the 46-year average and ranks 2015 as having the 36th most extensive (or 10th least extensive) cover on record. This evaluation considers snow over NH continents, including the Greenland ice sheet. SCE in 2015 ranged from 47.1 million km² in January to 3.0 million km² in August. Monthly SCE is calculated at the Rutgers Global Snow Lab from daily SCE maps produced by meteorologists at the National Ice Center (a U.S. joint NOAA, Navy, and Coast Guard facility), who rely primarily on visible satellite imagery to construct the maps.

SCE across the NH was close to average in January 2015, a balance between above-average cover in Eurasia (EU) and below-average over North America (NA). This reversed in February, with SCE 1.1 million km² below average, mostly due to the ninth lowest SCE over EU. Both continents ranked among their 10 smallest for SCE during March. Spring melt proceeded faster over NA than EU, with the overall NH April coverage in the middle tercile. May and June behaved like most years within the past decade, quickly losing continental snow cover. This resulted in the sixth lowest May NH SCE and second lowest in June within the satellite era.

TABLE 2.4. Monthly and annual climatological statistics on Northern Hemisphere and continental snow extent between November 1966 and December 2015. Included are: number of years with data used in the calculations, means, standard deviations, 2015 values, and ranks. Areas are in km² (millions). 1968, 1969, and 1971 have 1, 5, and 3 missing months, respectively, thus are not included in the annual calculations. North America (N. Am.) includes Greenland. Ranks are from most extensive (1) to least (ranges from 46 to 50, depending on the month).

	Years	Mean	Std. Dev.	2015	2015 N. Hem rank	Eurasia rank	N. Am. rank
Jan	49	47.1	1.6	47.3	22	18	32
Feb	49	46.1	1.8	45.0	36	41	20
Mar	49	40.6	1.8	38.5	43	41	40
Apr	49	30.6	1.7	30.1	28	21	35
May	49	19.3	1.9	17.0	44	38	47
Jun	48	9.7	2.4	5.4	47	47	47
Jul	46	4.0	1.2	2.5	42	39	44
Aug	47	3.0	0.7	2.6	34	39	23
Sep	47	5.4	1.0	5.9	14	18	8
Oct	48	18.3	2.6	21.4	7	6	11
Nov	50	34.0	2.1	36.2	7	7	19
Dec	50	43.7	1.9	43.5	32	30	22
Ann	46	25.1	0.8	24.6	36	29	39

Much as in the previous two years, snow arrived early over NH continents during autumn 2015, with SCE 14th highest in September. Coverage continued expanding quickly in October and November, each month ranking seventh most extensive. December saw the brakes put on this rapid expansion, with coverage 0.2 million km² below average, or 32nd most extensive.

SCE over the contiguous United States was at the boundary of the middle and lower tercile in January 2015. It was within the middle tercile but nearer the above-normal side in February. The situation changed considerably in spring, with March SCE the fifth lowest on record and April ninth least extensive. Autumn 2015 SCE began building slowly in October, ranking ninth lowest. This changed in November and December, which ranked 19th and 22nd most extensive, respectively.

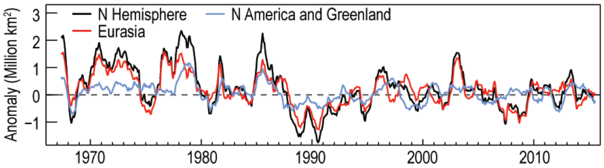

Fig. 2.12. Twelve-month running anomalies of monthly snow cover extent over Northern Hemisphere lands as a whole and Eurasia and North America (including Greenland) separately between Nov 1966 and Dec 2015. Anomalies are calculated from NOAA snow maps (http://snowcover.org) relative to 1981–2010. Monthly means for the period of record are used for 9 missing months between 1968 and 1971 in order to create a continuous series of running means. Missing months fall between Jun and Oct; no winter months are missing.

Maps depicting daily, weekly, and monthly conditions, daily and monthly anomalies, and monthly climatologies for the entire period of record may be viewed at the Rutgers Global Snow Lab website (http://snowcover.org). Monthly SCE for the NH, EU, NA, contiguous U.S., Alaska, and Canada are also posted, along with information on how to access weekly areas and weekly and monthly gridded products.

3) Alpine glaciers and ice sheets—M. S. Pelto

The World Glacier Monitoring Service (WGMS) record of mass balance and terminus behavior provides a global index for alpine glacier behavior. The WGMS dataset for terminus change contains 42 000 observations from 2000 glaciers extending from the mid-19th century. There are 5200 geodetic and glaciological mass balance observations in this dataset. Annual mass balance is the annual change in volume due to snow and ice accumulation and snow and ice losses. Here, WGMS mass balance is reported in mm of water equivalent (Fig. 2.13). In 2014 mean mass balance was –798 mm for the 41 long-term reference glaciers and –586 mm for all 130 observed glaciers. Preliminary data for 2015 from 16 nations with more than one reporting glacier from Argentina, Austria, Canada, Chile, Italy, Kyrgyzstan, Norway, Switzerland, and the United States indicate that 2015 will be the 36th consecutive year of negative annual balances with a mean loss of –1162 mm for 27 reporting reference glaciers and –1481 mm for all 59 reporting glaciers (WGMS 2016). Reference glaciers are those with records longer than 30 years, hence the increase from 37 in 2014 to 41 this year. The number of reporting reference glaciers is 90% of all reporting glaciers but only 50% of all glaciers that have reported to date. The preliminary data indicate 2015 mass balance will be one of the two most negative along with 2003, with 2003 at –1268 mm for reference glaciers and –1198 mm for all glaciers.

The unprecedented ongoing retreat is a result of strongly negative mass balances over the last 32 years (Zemp et al. 2015). An examination of the WGMS record by Zemp et al. (2015) found that the rates of early 21st century mass loss are without precedent on a global scale, at least for the time period observed. The Randolph Glacier Inventory version 3.2 (RGI) was completed in 2014, compiling digital outlines of alpine glaciers using satellite imagery from 1999 to 2010. The inventory identified 198 000 glaciers, with a total extent estimated at 726 800 ± 34 000 km^2 (Pfeffer et al. 2014). This inventory was crucial for glacier runoff modelling that indicates 11 of 13 alpine regions are experiencing decreased runoff (Bliss et al. 2014). This is due to a greater loss of glacier area than increased rate of glacier melt. The volume loss of alpine glaciers has led to a current sea level rise equivalent of approximately 0.8–1.0 mm year^{-1} (Marzeion et al. 2012).

The cumulative mass balance loss from 1980 to 2015 is 18.8 m, the equivalent of cutting a 20.5 m thick slice off the top of the average glacier (Fig. 2.13). The trend is remarkably consistent from region to region (WGMS 2015a). The decadal mean annual mass balance was –261 mm in the 1980s, –386 mm in the 1990s, –727 mm for 2000s, and –818 mm from 2010 to 2015. The declining mass balance trend during a period of glacier retreat indicates alpine glaciers are not approaching equilibrium and retreat will continue to be the dominant terminus response (Zemp et al. 2015). The recent rapid retreat and prolonged negative balances have led to many glaciers disappearing and others fragmenting (Pelto 2010; Carturan et al. 2015).

In South America, seven glaciers in Colombia, Argentina, and Chile reported mass balance in 2015. All seven glaciers had losses greater than 1200 mm,

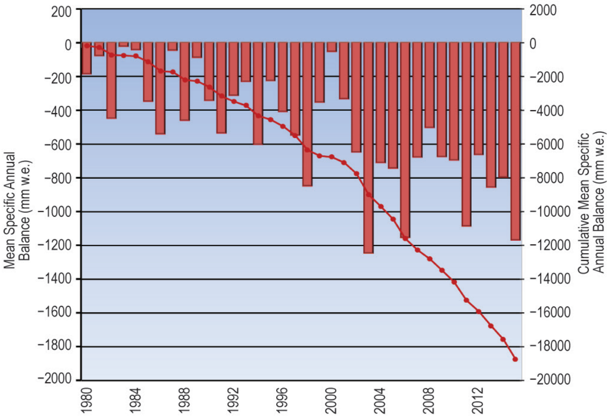

Fig. 2.13. Mean annual (red bars) and cumulative (red line) annual balance reported for the 41 reference glaciers to the WGMS (1980–2015). The data for 2015 are preliminary, only including 27 reference glaciers at the time of publication.

with a mean of –2200 mm. These Andean glaciers span 58° of latitude.

In the European Alps, mass balance has been reported for 15 glaciers from Austria, France, Italy, Spain, and Switzerland. All 15 had negative balances exceeding –1000 mm, with a mean of –1860 mm. This is an exceptionally negative mass balance, rivaling 2003 when average losses exceeded –2000 mm. The negative mass balances were largely due to an exceptionally hot summer (see section 7f), as in 2003.

In Norway, mass balance was reported for seven glaciers in 2015; all seven were positive with a mean of 860 mm. This is the only region that had a positive balance for the year. In Svalbard six glaciers reported mass balances, with all six having a negative mass balance averaging –675 mm.

In North America, Alberta, British Columbia, Washington (state), and Alaska mass balance data from 17 glaciers were reported with a mean loss of –2590 mm, with all 17 negative. This is the largest negative mass balance for the region during the period of record. From Alaska south through British Columbia to Washington the accumulation season temperature was exceptional with the mean for November–April being the highest observed (Fig. 2.14).

In the high mountains of central Asia, seven glaciers from China, Russia, Kazakhstan, and Kyrgyzstan reported data; all were negative with a mean of –705 mm.

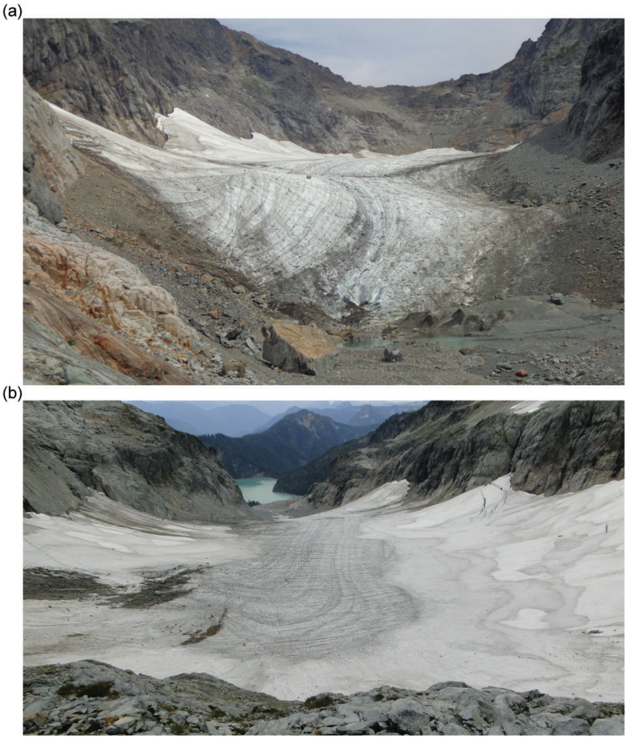

Fig. 2.14. Columbia Glacier, Washington: 1 of 41 WGMS reference glaciers, viewed on 4 Aug 2015 from (a) below the terminus and (b) above the head of the glacier. Note the lack of retained snowcover with seven weeks left in the melt season. Numerous annual firn and ice layers exposed. (Photo credit: M. Pelto)

d. Hydrological cycle

1) Surface humidity—K. M. Willett, D. I. Berry, M. G. Bosilovich, and A. Simmons

Surface moisture values in 2015 were at their highest level since the last El Niño event in 2010 (Fig. 2.15). Over land, levels of water vapor in the air (specific humidity) were well above the 1981–2010 average and approaching those of 1998 and 2010. Over oceans, annual average specific humidity values were higher than at any other point in the record that began in the early 1970s. The ability of the atmosphere to carry water vapor is limited by its temperature. The extra warmth associated with the El Niño, ongoing in some respects since 2014, together with generally above-average global temperatures, is consistent with the high atmospheric humidity seen in 2015. Similar anomalously high humidity levels are seen in the years following previous El Niño events, with the atmospheric humidity typically lagging the temperature changes by a few months.

Relative humidity levels in 2015 remained well below average, continuing an apparent declining trend since the early 2000s. While the land in situ data (HadISDH.2.1.0.2015p) are in broadscale agreement with the ERA-Interim and JRA-55 reanalyses in terms of overall behavior, HadISDH presents 2015 as slightly more moist than 2014 whereas both reanalyses present 2015 as slightly more arid. However, for HadISDH at least, the 2015–2014 difference is smaller than the annual uncertainty estimate for 2015 (±0.2% rh)

All estimates contain uncertainty. Arguably the largest sources of uncertainty, generally, are the gaps in sampling both in space and time. There is also uncertainty stemming from systematic errors in the data and the different methods for dealing with these by bias correction or homogeneity detection and adjustment. Over the ocean (Berry and Kent 2009, 2011), ship heights have increased over time, requiring height adjustment to avoid erroneously decreasing specific and relative humidity. Systematic biases have also been found between psychrometers housed within screens versus those that are hand held. Over land (Willett et al. 2013b, 2014b), changes to observing instruments, locations, or processes have been common and poorly documented, requiring statistical methods to account for them. Measurement uncertainty also plays a role. Reanalyses (Simmons et al. 2010; Simmons and Poli 2014) have the benefit of the physical model and assimilation of high density observations with which to reduce the errors. However, they are not fully immune to such issues, and changing data streams over time can introduce inhomogeneities that can be substantial (Kent et al. 2014).

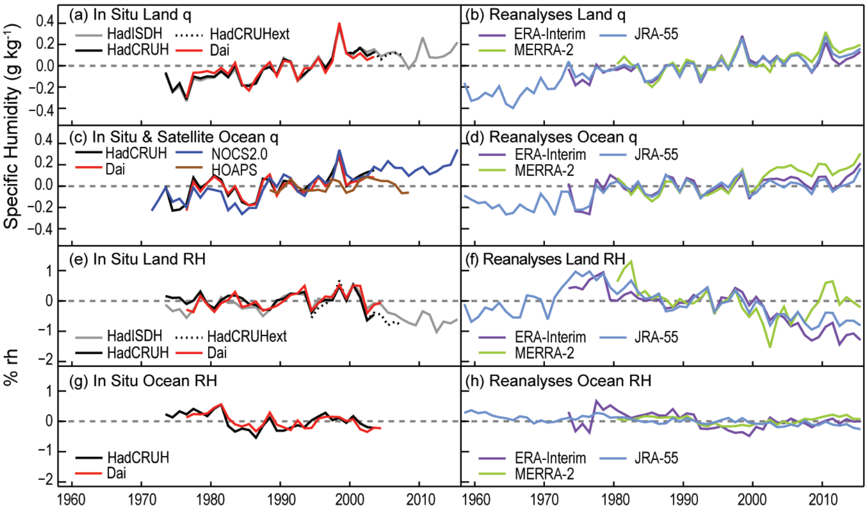

Fig. 2.15. Global average surface humidity annual anomalies (base period: 1979–2003). For in situ datasets, 2-m surface humidity is used over land and ~10-m over the oceans. For the reanalysis, 2-m humidity is used across the globe. For ERA-Interim, ocean-only points over open sea are selected and background forecast values are used as opposed to analysis values because of unreliable use of ship data in producing the analysis. All data have been adjusted to have a mean of zero over the common period 1979–2003 to allow direct comparison, with HOAPS given a zero mean over the 1988–2003 period. ERA values over land are from ERA-40 prior to 1979 and ERA-Interim thereafter. [Sources: HadISDH (Willett et al. 2013a, 2014a); HadCRUH (Willett et al. 2008); Dai (Dai 2006); HadCRUHext (Simmons et al. 2010); NOCSv2.0 (Berry and Kent, 2009, 2011); HOAPS (Fennig et al. 2012) and reanalyses as described in Fig. 2.1. Data provide by authors, A. Dai, M. Bosilovich and S. Kobayashi.]

Despite these uncertainties, there is generally good agreement between the various estimates presented here [described more fully in Willett et al. (2013a, 2014a)]. The new MERRA-2 reanalysis (R. Gelaro et al. 2016 unpublished manuscript; Bosilovich et al. 2015) shows better agreement than the previously used MERRA, owing to improved data selection, inclusion of modern data, and model and data assimilation advances. MERRA-2 uses observation-corrected precipitation for forcing the land surface, which helps constrain the near-surface temperature and moisture over land (Reichle and Lui 2015). While the year-to-year variability is similar to the other estimates, there are some deviations around 2002 and 2007–09 (Fig. 2.15). These are thought to be linked to variability in the precipitation forcing at those times. All agree on the most recent period having the highest specific humidity levels on record while also being the most arid in relative humidity terms (Fig. 2.15).

Spatially, specific humidity was anomalously high over much of the land, especially over India and Southeast Asia, which was also common to 1998 and 2010 (Plate 2.1k; Online Figs. S2.10, S2.11). In contrast to 2014, the United States experienced almost entirely above-average specific humidity. Southern Africa was particularly dry. Over oceans, data quality significantly impacts the spatial coverage of the in situ data, meaning that the key El Niño–Southern Oscillation (ENSO) region of the Pacific Ocean is not well observed. ERA-Interim and MERRA-2 show strong moist anomalies there, in good agreement with the other hydrological cycle ECVs and the very warm SSTs (Plate 2.1c, Online Figs. S2.1 to S2.3).

Relative humidity was anomalously low over much of the land (Plate 2.1l; Online Fig. S2.12). Interestingly, some regions, such as southern Africa and Australia, experienced both below-average water vapor amounts (specific humidity) and levels of saturation (relative humidity), while other regions, such as the United States and southern India, experienced above-average water vapor but below-average saturation. The regions of low relative humidity are broadly, but not exactly, consistent with below-average precipitation (Plate 2.1h). Over the oceans there was a strong dipole along the equatorial Pacific with much lower-than-average values to the south. This was slightly farther north than the specific humidity dipole associated with the El Niño warm pool.

2) Total column water vapor—C. Mears, S. Ho, J. Wang, H. Huelsing, and L. Peng

Total column water vapor (TCWV) rapidly increased during 2015 in response to the 2015/16 El Niño event (Fig. 2.16), with the annual average anomaly lying well above the long-term average. Estimates come from satelliteborne microwave radiometers over ocean (Wentz 1997, 2015), COSMIC

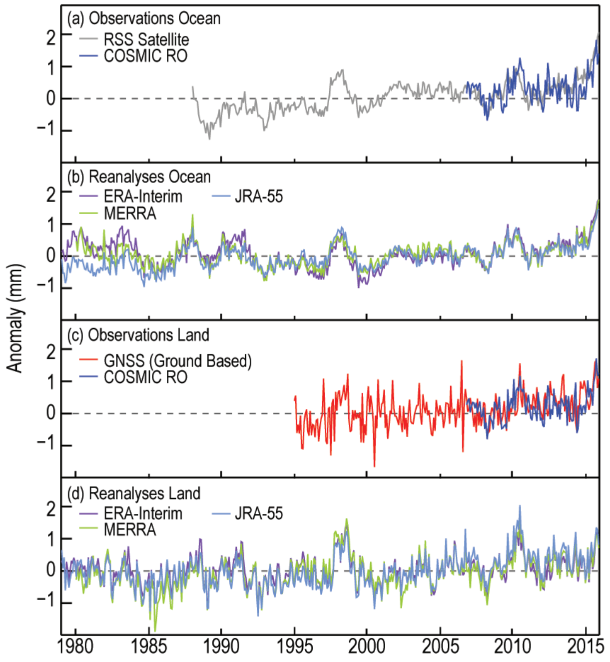

Fig. 2.16. Global average total column water vapor anomalies (mm; 1981–2010 reference period) for (a,b) ocean only and (c,d) land only for observations and reanalyses (see Fig. 2.1 for reanalyses references) averaged over 60°S–60°N. The shorter time series have been given a zero mean over the period of overlap with ERA-Interim (1988–2015 for RSS Satellite, 1995–2015 for GNSS, 2007–15 for COSMIC).

GPS-RO (Global Positioning System–Radio Occultation) over land and ocean (Ho et al. 2010; Teng et al. 2013; Huang et al. 2013), and ground-based GNSS (Global Navigation Satellite System) stations (Wang et al. 2007) over land. The 2015 anomaly map (Plate 2.1o) combines data from satellites over ocean and COSMIC GPS-RO over land with ground-based GNSS stations (Wang et al. 2007) also shown. Most of the tropical Pacific showed a large wet anomaly, which grew to unprecedented size by the end of 2015. Wet anomalies, albeit less pronounced, covered most of the rest of the globe, except for dry anomalies over the Maritime Continent, north of New Zealand, to the south of Greenland, southern Africa, and the Amazon basin. The spatial patterns in TCWV over the ocean (Plate 2.1o) are confirmed by similar features in COSMIC ocean measurements and supported by reanalysis output.

Over the ocean, the TCWV anomaly time series (Fig. 2.16a,b) from reanalysis and microwave radiometers show maxima in 1983/84, 1987/88, 1997/98, 2009/10, and late 2015, each associated with El Niño events. The December 2015 anomaly is the largest recorded for any month, particularly in the satellite radiometer data. This is a result of the large wet anomaly in the tropical Pacific Ocean, coupled with the lack of large dry anomalies across the rest of the world. The radiometer data show a discernible increasing trend over the period. The different reanalysis products show reasonable agreement from the mid-1990s but deviations prior to that, resulting in a range of long-term trends. Minima are apparent in Northern Hemisphere winters during the La Niña events of 1984/85, 1988/89, 1999/2000, 2007/08, and late-2010 to mid-2012. The ocean-only COSMIC data are in general agreement with the reanalysis and radiometer data, but show a sharp peak in early 2012 and a small dip relative to the other data after 2013.

Over land, average anomalies from the ground-based GNSS stations are used in place of the satellite radiometer measurements (Figs. 2.16c,d), providing a record back to 1995, alongside the much shorter COSMIC record. The various reanalysis products, COSMIC, and GNSS are in good agreement throughout the record and all show a subtle increase in TCWV, similar to over ocean.

A land-and-ocean time–latitude plot derived from JRA-55 (Fig. 2.17) indicates that the long-term increase in TCWV is occurring at all latitudes, with less variability outside the tropics. The El Niño events are clear, especially the 1997/98 event. The previous strong El Niño events during 1983/84 and 1997/98 showed pronounced drying in the northern tropics that accompanied moistening on the equator and the southern subtropics. Although similar in strength in terms of sea surface temperature, the TCWV response to the current El Niño does not show this feature (see Sidebar 1.1; Online Fig. S2.13).

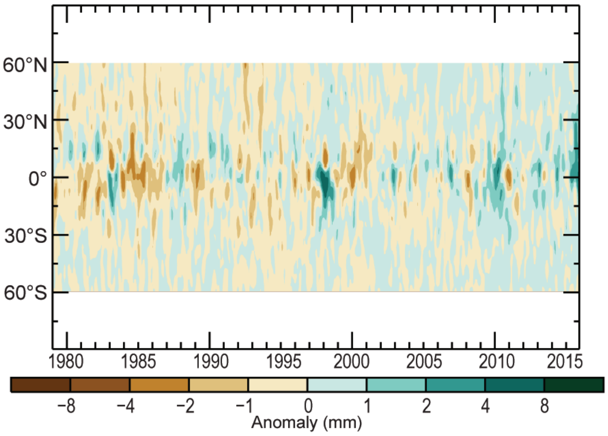

Fig. 2.17. Hovmöller plot of total column water vapor anomalies (mm; base period 1981–2010) including land and ocean derived from JRA-55 reanalysis.

3) Upper tropospheric humidity—V. O. John, L. Shi, and E.-S. Chung

Global scale monitoring of upper tropospheric relative humidity (UTH) was first reported last year, using one dataset of satellite origin and one reanalysis. However, the reanalysis data showed drying of the upper troposphere since 2001 that was not present in the satellite data. Therefore, for this year, two independent UTH satellite datasets are used. One is the infrared-based HIRS dataset (Shi and Bates 2011) which was used last year, and the other is the microwave-based UTH dataset (Chung et al. 2013). UTH represents a weighted average of relative humidity in a broad layer, roughly between 500 and 200 hPa. Humidity distribution at these levels of the atmosphere is a key climate variable due to its strong control on the outgoing longwave radiation (OLR) which makes a strong feedback factor in the climate system.

Area-weighted anomaly time series of UTH for the 60°N–60°S latitude belt are shown in Fig. 2.18. The anomalies are computed relative to 2001–10 because the microwave-based UTH dataset begins only in 1999. A slightly below-average 2015 anomaly is observed. A near-zero trend in the UTH time series indicates an increase in specific humidity in the warming upper troposphere and is consistent with a positive water vapor feedback (Chung et al. 2016). It is encouraging to see good agreement between the two independent datasets despite their differences in sampling: microwave data have an almost all-sky sampling whereas HIRS data samples mainly clear-sky areas. The annual average of UTH for 2015 (Plate 2.1n; Online Fig. S2.14) shows large moist anomalies over the central and eastern tropical Pacific and dry anomalies over the Maritime Continent, which results from the strong El Niño of 2015. This signal is stronger in the microwave dataset (Online Fig. S2.14) compared to HIRS (Plate 2.1n), possibly because of the sampling differences. The weak dry anomalies over India are an indication of the weak monsoon season in 2015 (see section 7g4).

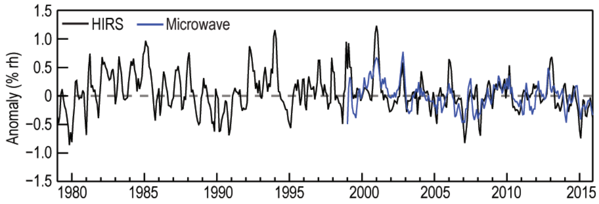

Fig. 2.18. Anomaly time series of upper tropospheric humidity using HIRS (black) and microwave (blue) datasets. The anomalies are computed based on 2001–10 average, and the time series is smoothed to remove variability on time scales shorter than 3 months.

4) Precipitation—R. S. Vose, A. Becker, K. Hilburn, G. Huffman, M. Kruk, and X. Yin

Precipitation over the global land surface in 2015 was far below the long-term average (Fig. 2.19). In fact, 2015 was the driest year on record in two prominent global products: the Global Precipitation Climatology Centre (GPCC) dataset (Schneider et al. 2011; Becker et al. 2013), which is based on surface stations, and the Global Precipitation Climatology Project (GPCP) version 2.3 (Adler et al. 2003), which is based on both satellite data and surface stations. Last year was also among the five driest years on record in a new (experimental) version of another prominent global product, the Global Historical Climatology Network (GHCN) dataset (Peterson and Vose 1997; Menne et al. 2012), which contains about five times as many surface stations as its operational counterpart (version 2).

From a spatial perspective, coherent anomaly patterns were evident across the global land surface in 2015 (Plate 2.1h). El Niño affected precipitation in many areas; in particular, below-average precipitation fell over much of northeastern South America, southern Africa, the Maritime Continent, and northern Australia, while above-average precipitation fell over the southeastern quadrants of North and South America. Relative to 2014, northern and eastern Asia became much wetter while western Europe became much drier.

In contrast to global land areas, precipitation over the global ocean surface in 2015 was much above the long-term average, continuing the general increase of the last five years (Fig. 2.19). Above-normal precipitation over the ocean served as a counterpoint to below-normal precipitation over land, and thus the global value for 2015 was slightly above the long-term

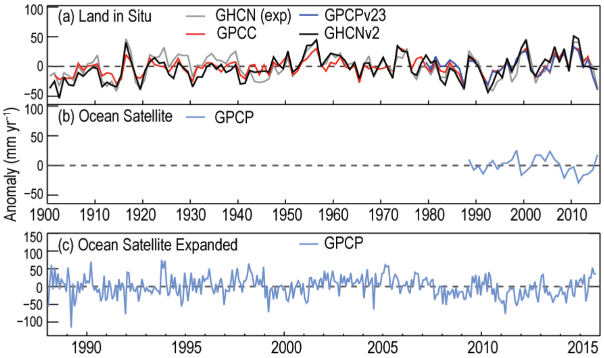

Fig. 2.19. Globally averaged precipitation anomalies (mm) for (a) four in situ datasets over land (1961–90 base period) and (b), (c) one satellite-based dataset over ocean (1988–2010 base period). Ocean averages are for the global ocean equatorward of 60° latitude using a common definition of "ocean" and the annual cycle has been removed.

average. The ongoing El Niño, which was particularly dominant in the tropics in the latter half of the year, resulted in several distinct anomaly patterns over the ocean (Plate 2.1h). In particular, an intense positive anomaly of rainfall stretched across the Pacific Ocean along the Inter-Tropical Convergence Zone, just north of the equator. The western Pacific experienced two distinct anomaly maxima (a larger one slightly to the south of the equator and a secondary one to the north). In addition, there was a strong negative rainfall anomaly over the seas of the Maritime Continent. Other large anomalies for 2015 include above-normal rainfall over the central Indian Ocean and the eastern Pacific Ocean (east of the Hawaiian Islands) as well as below-normal precipitation in parts of the northern and southern Pacific Oceans.

5) Cloudiness—M. J. Foster, S. A. Ackerman, K. Bedka, R. A. Frey, L. Di Girolamo, A. K. Heidinger, S. Sun-Mack, B. C. Maddux, W. P. Menzel, P. Minnis, M. Stengel, and G. Zhao

Based on the longest continuous record of cloud cover, PATMOS-x (Pathfinder Atmospheres Extended; Heidinger et al. 2013), 2015 was 1.4% less cloudy than the 35-year average, making it the 10th least cloudy year on record. Global mean annual cloudiness anomalies from eight satellite records are shown in Fig. 2.20. Four of the records—MISR (Multiangle Imaging Spectroradiometer; Di Girolamo et al. 2010), *Aqua* MODIS C6 (Moderate Resolution Imaging Radiospectrometer Collection 6; Ackerman et al. 2008), *CALIPSO* (Cloud-Aerosol Lidar and Infrared Pathfinder Satellite Observation; Winker et al. 2007), and CERES (Clouds and the Earth's Radiant Energy System) *Aqua* MODIS (CERES-MODIS; Minnis et al. 2008; Trepte et al. 2010) show little change in global cloudiness from 2014 to 2015 (<0.1%). PATMOS-x and HIRS (High Resolution Infrared Sounder; Wylie et al. 2005; Menzel et al. 2014)—show modest increases of 0.30% and 0.29%, respectively, while SatCORPS (Satellite ClOud and Radiative Property retrieval System; Minnis et al. 2015) shows an increase of 1.1%, and CLARA-A2 (Cloud, ALbedo and RAdiation dataset; Karlsson et al. 2013) shows a modest decrease of 0.25%. Three of the records—PATMOS-x, CLARA-A2, and SatCORPS—are derived from the AVHRR (Advanced Very High Resolution Radiometer) on the NOAA Polar Orbiter Environmental Satellite series and more recently the EUMETSAT Polar System Metop series. SatCORPS is the most recent addition and was developed through the NOAA Climate Data Record program. CLARA-A2 is the successor to CLARA-A1 and includes several changes, the most notable to impact global cloudiness being improvements in cloud detection over semiarid regions. In addition to instrument sensitivity and calibration, several factors contribute to differences among the records. For example, the AVHRR-derived records use different methods to account for satellite diurnal drift, while HIRS is primarily focused on detection of cirrus cloud.

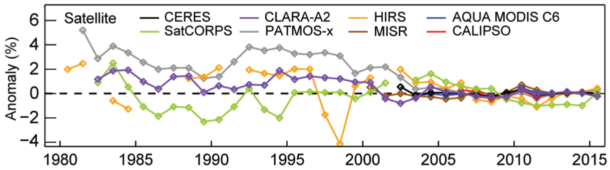

Fig. 2.20. Annual global cloudiness anomalies for 1981–2015 (base period, 2003–14, a period common to the satellite records excluding *CALIPSO*, where the entire record was used instead). Datasets include PATMOS-x, HIRS, MISR, *AQUA* MODIS C6, *CALIPSO*, CERES, SatCORPS and CLARA-A2.

The satellite records are in good agreement post-2000, but prior to 2000, global cloudiness was more variable among the records and was relatively higher for all series with the exception of SatCORPS. Four of the records in Fig. 2.20 are derived from instruments flown on the NASA Earth Observing System (EOS) satellite missions, beginning in 1999 with the launch of *Terra*. MISR is flown on *Terra*, while CERES and MODIS are flown on *Terra* and *Aqua* (launched in 2002). Recent calibration issues with IR channels on *Terra*/MODIS have resulted in artificial positive trends in cloudiness, noticeable from around 2010, so only *Aqua*/MODIS is included here. *CALIPSO* was launched in 2006.

One explanation posited for the discrepancy between pre- and post-2000 is the lack of strong El Niño events in recent years. The last strong El Niño event was observed in 1997/98. Thus 2015 is significant in that it is the first year with a strong El Niño event during the NASA EOS/post-2000 era. The close agreement between cloud records and lack of a large positive cloudiness anomaly in relation to the current El Niño suggest that El Niño events in the 1980s and 1990s are, by themselves, not sufficient to explain the larger variability and higher cloudiness seen in the records of that time.

Figure 2.21 shows the shift in the tropical ice clouds during the 2015/16 and 1997/98 El Niño events (see Sidebar 1.1). The 1998 and 2016 images show observations during strong El Niño months while the 1997 and 2015 images show the same month of the previous year (preceding the El Niño). Both El Niño events see a dramatic shift of ice clouds in January from the Warm Pool region of the western Pacific to

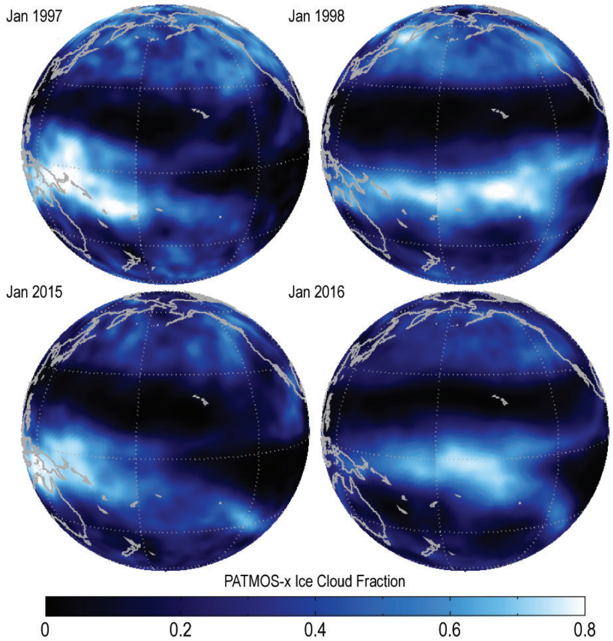

Fig. 2.21. Mean ice cloud fractions for Jan 1997, 1998, 2015 and 2016. Data from 1997 and 1998 are from NOAA-14/AVHRR and data from 2015 and 2016 from SNPP/VIIRS.

central Pacific. This caused statistically significant (at the 5% level) lower cloud cover over the Maritime Continent and the equatorial western Pacific and correspondingly significant higher cloud cover across the central and eastern Pacific (see Plate 2.1m). As the warm SSTs shift to the east, so do the tropical convection and the associated ice cloud. The 1997/98 data were taken from the AVHRR PATMOS-x record, which spans 1982–present. The 2015/16 data were generated using the SNPP/VIIRS instrument, which is the successor to the AVHRR.

Smaller, but still statistically significant, anomalies were observed across the globe, with many regional anomalies being attributable to teleconnections associated with El Niño. For example, the Amazon basin experienced significant drought, which corresponded to a reduction in cloud cover. The cloud cover over the southeast Pacific off the coast of Peru and the stratocumulus deck off the coast of southwest North America were both anomalously low. Interestingly, other atmospheric oscillations such as the record positive Pacific decadal oscillation (PDO) showed little impact on the annual and monthly cloud cover.

Other anomalies, not statistically significant for the entire year, were observed in the first half of the year, prior to El Niño (see Online Figs. S2.15, S2.16). Some of these anomalies corresponded with a record positive PDO, but were not directly attributable to it. Large positive anomalies in cloud cover over the southern United States coincided with its wettest month on record in May (see section 7b2).

6) River discharge—H. Kim

Runoff is one of the key components of the terrestrial water cycle. It serves as an integrated residual of the various hydraulic and hydrological processes after water has fallen on the land as precipitation. River discharge accumulates and transports total runoff generated in upstream watersheds to the ocean, playing a significant role in the freshwater balance and the salinity of the ocean.

Because of the lack of an observational methodology for real-time global long-term monitoring (Fekete et al. 2012), offline model simulation has been the primary method rather than in situ networks [e.g., the Global Runoff Data Centre (GRDC); Fekete, 2013]. A 58-year (1958–2015) terrestrial hydrologic simulation is performed by the ensemble land surface estimator (ELSE; Kim et al. 2009). The atmospheric boundary condition has been updated to use the second Japanese global atmospheric reanalysis (JRA-55; Kobayashi et al. 2015) and the Monitoring Product version 5 (Schneider et al. 2015) monthly observational precipitation by the Global Precipitation Climatology Centre (GPCC). The other parts of the simulation framework remain as described by Kim and Oki (2015). ELSE has been validated against the GRDC and also terrestrial water storage from GRACE (Kim et al. 2009).

The global distributions of runoff and river discharge anomalies in 2015 (relative to the 1958–2015 base period) are illustrated in Plates 2.1i and 2.1j, respectively. Most river basins in the tropics, such as the Congo, Zambezi, Tocantins, and São Francisco, show anomalously dry conditions. Among the major river basins in the subtropics and temperate regions, the Danube, La Plata, Indus, and Yangtze were wetter than the climate normal. The Mississippi, Nile, and Volga were drier than their long-term mean states. Many of the basins in northern latitudes (e.g., Ob, Yenisei, and Lena) were wetter than their climatological mean.

The 58-year time series of total terrestrial runoff anomalies and of the ENSO intensity are shown in Fig. 2.22. Variations of annual mean runoff and the oceanic Niño index (ONI) time series, smoothed by 12-month window moving average, are significantly anticorrelated with each other (R = −0.63). Because a strong El Niño developed through 2015, at the global scale the mean anomaly turned into a dry phase. However, it still remained close to the climate normal because of the lingering effect of La Niña

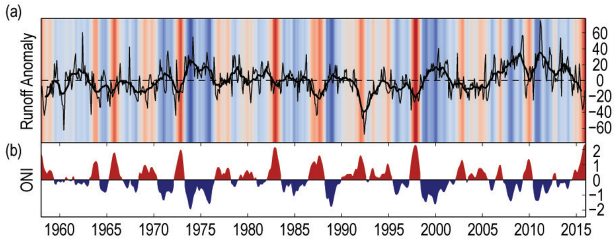

FIG. 2.22. (a) Interannual variability of global runoff anomalies relative to the 1958–2015 base period (thick line for 12-month window moving average) and (b) the oceanic Niño index (ONI) [red and blue shades for positive and negative phases, respectively, with lighter (darker) shades representing weaker (stronger) phases in (a)].

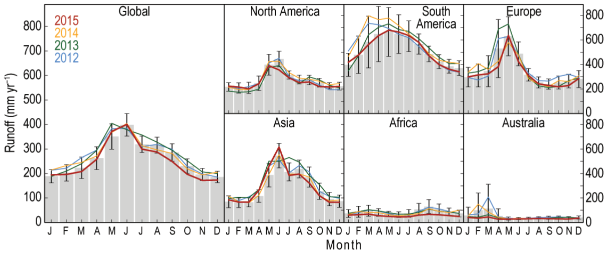

FIG. 2.23. Seasonal variations of global and continental runoff. Gray bars show the 58-year climatology (1958–2015) with error bars for 2σ and colored lines for the most recent 4 yrs.

after the 2009/10 El Niño. As shown in Fig. 2.23, seasonal variations of global runoff remained near the long-term mean during the boreal spring and summer and turned into a strong dry phase (~2σ) from the boreal autumn onwards. Regionally, North America, Asia, and Europe experienced significantly dry conditions during the latter half of 2015, and the dry condition was persistent in Africa through the entire year. During the most recent four years, large interannual variability affected South America, Europe, and Australia during February–July while the seasonal fluctuations in Africa were weak.

7) Groundwater and terrestrial water storage—
M. Rodell, D. P. Chambers, and J. S. Famiglietti

Terrestrial water storage (TWS) comprises groundwater, soil moisture, surface water, snow, and ice. Groundwater varies more slowly than the TWS components that are more proximal to the atmosphere, but often it is more dynamic on multiannual timescales (Rodell and Famiglietti 2001). In situ groundwater data are archived and made public by only a few countries. However, since 2002 the Gravity Recovery and Climate Experiment (GRACE; Tapley et al. 2004) satellite mission has been providing observations of TWS variations which are a reasonable proxy for unconfined (having a free water table that responds to atmospheric pressure and processes like plant uptake and evaporation) groundwater variations at climatic scales.

Changes in mean annual TWS from 2014 to 2015 are plotted in Plate 2.1g as equivalent heights of water in cm. TWS can be thought of as an integrator of other hydroclimatic variables (see Plates 2.1f–p). In addition to being very warm, 2015 was a dry year in terms of water in the ground, particularly in the southern tropics. TWS decreased in central and eastern South America, in southern Africa, and in central Australia. In 2014 the former two regions mostly had gained TWS. The year 2015 was also dry for much of the western United States and Canada, as the historic drought in California reached a crescendo in autumn before El Niño brought some relief. Drought diminished water levels across a swath of central Europe, from France across to western Russia. A combination of drought and water consumption most likely continued to diminish groundwater in the Middle East (Voss et al. 2013), northern India (Rodell et al. 2009; Panda and Wahr 2016), and the North China Plain (Feng et al. 2013). On the other hand, Turkey recovered from a major drought, and TWS also increased in a longitudinal band from Pakistan north through Afghanistan, Kazakhstan, and west central Russia. TWS also increased appreciably in Morocco (heavy rainfall in August), Texas and northern Mexico (continued recovery from a deep drought), central Argentina (heavy rains in February and August), and Peru and western Brazil. Northern Africa and eastern Asia were a mosaic of increasing and decreasing TWS, as seen in Plate 2.1g. Significant reductions in TWS in Greenland, Antarctica, and southern coastal Alaska represent ongoing ice sheet and glacier ablation, not groundwater depletion.

Figures 2.24 and 2.25 show time series of zonal mean and global, deseasonalized monthly TWS anomalies from GRACE, excluding Greenland and Antarctica. Data gaps occur in months when the satellites were powered down during certain parts of the orbital cycle to conserve battery life. Relative dryness in the southern tropics and northern equatorial zone in 2015 is clear in Fig. 2.24, while the northern midlatitudes maintained their low TWS conditions. All told, Earth's nonpolar TWS hit a new GRACE-period low in 2015, –2.3 cm equivalent height of water (Fig. 2.25), equivalent to about 9 mm of sea level rise across the global oceans.

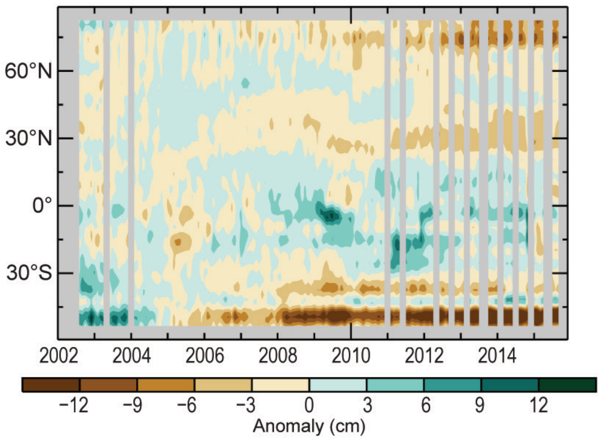

Fig. 2.24. GRACE zonal mean terrestrial water storage anomalies (cm equivalent height of water; base period: 2005–10). Gray areas indicate months when data were unavailable.

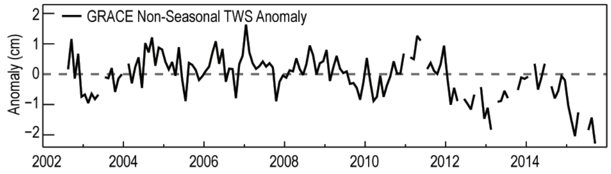

Fig. 2.25. GRACE global average terrestrial water storage anomalies (cm equivalent height of water, base period: 2005–10).

8) Soil moisture—W. A. Dorigo, D. Chung, A. Gruber, S. Hahn, T. Mistelbauer, R. M. Parinussa, C. Paulik, C. Reimer, R. van der Schalie, R. A. M. de Jeu, and W. Wagner

Satellite-mounted microwave instruments can measure the moisture content of the upper few centimeters of the unsaturated soil column. Dedicated soil moisture missions, such as the Soil Moisture Active Passive (SMAP) mission launched in 2015 by NASA, are able to provide nearly contiguous global spatial coverage at daily time scales but, as stand-alone missions, are too short for assessing soil moisture variability and change in the context of a changing climate. To bridge this gap, the ESA Climate Change Initiative (CCI) developed the first multisatellite surface soil moisture dataset (ESA CCI SM), which combines observations from a large number of historical and present-day passive and active microwave instruments (De Jeu et al. 2012b; Liu et al. 2012; Wagner et al. 2012). The current version of the dataset combines nine different sensors (SMMR, ERS-1/2, TMI, SSM/I, AMSR-E, ASCAT, WindSat, AMSR2, and SMOS) between late 1978 and December 2015. It has been used for a wide range of applications (e.g., Dorigo and De Jeu 2016) and has been benchmarked against a large number of land surface models and in situ datasets (Albergel et al. 2013; Dorigo et al. 2015b; Loew et al. 2013), revealing a good performance across the globe except for densely vegetated areas. The surface soil moisture content sensed by the microwave satellites is closely linked to that of the root zone (Paulik et al. 2012), except for very dry conditions where they may become decoupled (Hirschi et al. 2014). Based on the ESA CCI SM dataset, the yearly and monthly anomalies are computed here with respect to a 1991–2014 climatology.

For 2015, spatial anomaly patterns (Plate 2.1f) are markedly different from 2014 when, on a global scale, near-normal conditions prevailed (Dorigo et al. 2015a). The anomalous dry conditions in central-eastern Europe and Spain mainly resulted from the excessively warm and dry summer and autumn in this region (http://edo.jrc.ec.europa.eu/; ZAMG 2016, see October monthly anomalies; Online Fig. S2.17j). For eastern Brazil, strong anomalous negative soil moisture conditions were observed for the fourth consecutive year (Dorigo et al. 2014, 2015a; Parinussa et al. 2013), which may further exacerbate shortfalls in water supply in the states of São Paulo, Rio de Janeiro, and Minas Gerais. Below-average soil moisture conditions in southern Africa resulted from a dry episode in the southwest in early 2015, in combination with aggravating drought conditions towards the end of the year in the southeastern part of the continent (Online Fig. S2.17), increasing the risk of crop failure and food shortage in South Africa, Mozambique, Madagascar, Malawi, and Zimbabwe. For parts of Queensland, Australia, negative anomalies were a continuation of drought conditions observed in this region over the past three years (BoM 2016; Dorigo et al. 2014, 2015a). Even though most parts of Indonesia and Papua New Guinea are masked as missing because of dense vegetation, which is impenetrable for the microwave sensors used in ESA CCI SM, strong negative anomalies were still observed in the agricultural areas. Dry conditions promoted deforestation and biomass burning practices in this area, causing severe air quality problems during several months (sections 2g3, 2h3; Sidebar 2.2).

Prevailing wet soil moisture anomalies were observed for most of the United States, including the southwest, which was previously plagued by a persistent drought for several years (Dorigo et al. 2014, 2015a). Large parts of the United States experienced their wettest May on record (see section 7b2), which is reflected by the strong positive soil moisture anomalies (Online Figs. S2.17e,f). The shift from dry to wet conditions from October through November was remarkable, following the passage of Hurricane Patricia (Online Fig. S2.17). Anomalous wet soil moisture conditions were also observed in eastern China with reported severe floods in May–June. The southern part of South America also experienced wetter-than-usual conditions, including severe flooding in Argentina and heavy precipitation in the Chilean Atacama Desert in March (see section 7c3).

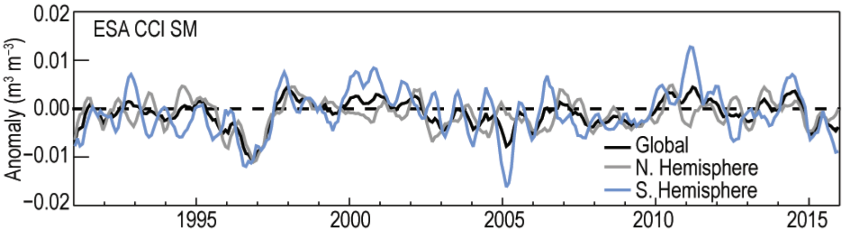

Fig. 2.26. Time series of average global soil moisture anomalies for 1991–2015 (base period: 1991–2014). Data were masked as missing where retrievals were either not possible or of very low quality (dense forests, frozen soil, snow, ice, etc.). (Source: ESA CCI.)

To a large extent, the spatially distinct patterns in 2015 can be related to the strong El Niño conditions during the second half of the year (NOAA/ESRL 2016). ENSO anomalies are known to potentially cause continentwide deviations in terrestrial water storages (Bauer-Marschallinger et al. 2013; Boening et al. 2012; De Jeu et al. 2011, 2012a; Miralles et al. 2014c). ENSO-driven global negative soil moisture anomalies were clear during the 1997/98 El Niño, while positive anomalies were observable for the strong La Niña episode of 2010/11, especially for the Southern Hemisphere (Fig. 2.26). The negative soil moisture anomalies in the Southern Hemisphere are visible in the time–latitude diagram (Fig. 2.27), which shows the strongest anomalies in the southern tropics. However, even though El Niño conditions in 2015 were almost as strong as in 1997/98, its impact up to the end of 2015 on global soil moisture was not as strong. This suggests that other climate oscillations may have partly counterbalanced the effects of El Niño during 2015 at least.

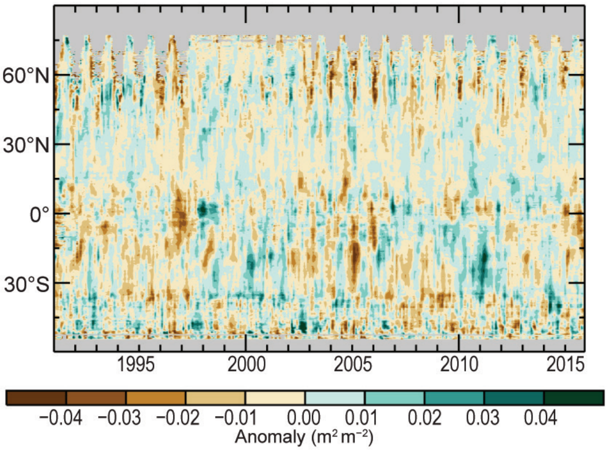

Fig. 2.27. Time–latitude diagram of soil moisture anomalies (base period: 1991–2014). Data were masked as missing where retrievals are either not possible or of low quality (dense forests, frozen soil, snow, ice, etc.). (Source: ESA CCI.)

No evident large-scale, long-term global soil moisture trends can be observed (Figs. 2.26, 2.27). However, this does not exclude the existence of long-term trends at the regional or local scale (Dorigo et al. 2012). Trends in average global soil moisture should be treated with caution owing to dataset properties changing over time and the inability to observe beneath dense vegetation, for mountain areas, or frozen soils (cf. gray regions in Plate 2.1f and Online Fig. S2.17).

9) Monitoring global drought using the self-calibrating Palmer drought severity index—T. J. Osborn, J. Barichivich, I. Harris, G. van der Schrier, and P. D. Jones

Hydrological drought results from a period of abnormally low precipitation, sometimes exacerbated by additional evapotranspiration (ET), and its occurrence can be apparent in reduced river discharge, soil moisture, and/or groundwater storage, depending on season and duration of the event. Here, an estimate of drought called the self-calibrating Palmer drought severity index is presented (scPDSI; Palmer 1965; Wells et al. 2004; van der Schrier et al. 2013a) using precipitation and Penman–Monteith potential ET from an early update of the CRU TS 3.24 dataset (Harris et al. 2014). Moisture categories are calibrated over the complete 1901–2015 period to ensure that "extreme" droughts and pluvials relate to events that do not occur more frequently than in approximately 2% of the months. This affects direct comparison with other hydrological cycle variables in Plate 2.1, which use a different baseline period. Other drought indices can give varied results (see van der Schrier et al. 2015).

van der Schrier et al. (2015) noted that 2014 appeared to have a remarkably small global area affected by drought, but the updated analysis (Fig. 2.28, with additional precipitation data that was not available at the time) now suggests that 2014 was affected by more extensive droughts (8% of land in severe drought at the end of 2014, compared with only 5% previously estimated). See Online Fig. S2.18 for a comparison with last year's analysis.

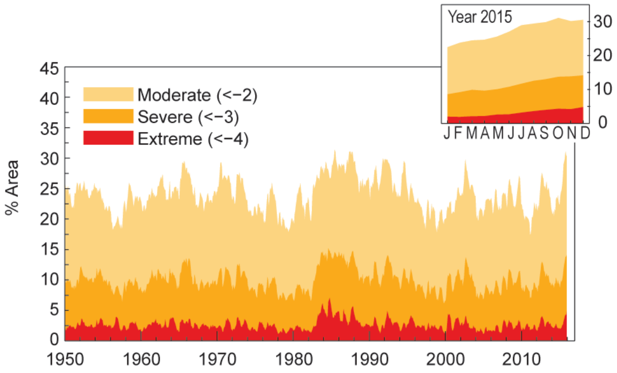

Fig. 2.28. Percentage of global land area (excluding ice sheets and deserts) with scPDSI indicating moderate (< −2), severe (< −3) and extreme (< −4) drought for each month of 1950–2015. Inset: 2015 monthly values.

There was a large expansion in the overall area of drought across the globe in 2015 (Fig. 2.28, inset), with 14% of global land seeing severe drought conditions (scPDSI < –3) by the end of the year. The areas where scPDSI indicates moderate (30%), severe (14%), or extreme (5%) droughts by the end of 2015 are among the highest in the post-1950 record, exceeded only by some years in the mid-1980s. The 2015 peak should be interpreted cautiously, given that more observations for the final months of 2015 will become available in due course (see Online Fig. S2.18).

The regional patterns of drought (Plate 2.1p) are partly associated with the strong El Niño event that developed during 2015. The full effect of this event may not be apparent until 2016, and other factors dominate in regions where the influence of the tropical Pacific is weak. Averaged over 2015, almost no regions of Africa experienced wet spells, and indeed most land areas south of 20°N across all continents were either near-normal (31% with scPDSI within ±1) or subject to some degree of drought (56% with scPDSI <–1).

Extensive severe or extreme drought affected many countries in southern Africa, intensifying as the 2015 El Niño progressed. These areas had been slowly recovering since a dry spell that began with the previous El Niño in 2010. In the Horn of Africa, severe drought affected Ethiopia and some neighboring regions in 2015, with significant impacts despite being apparent only over a relatively small region in the scPDSI data (Plate 2.1p). Very few areas of Africa exhibited wet spells in the 2015 mean scPDSI.

The effects of the 2014 drought in southeastern Brazil continued to be felt in 2015, though high rainfall farther south over the Paraná basin (consistent with previous strong El Niño events) replaced drought with wet conditions. New regions of drought emerged in the El Niño-sensitive regions of northeastern Brazil, Venezuela, and Colombia; these are expected to impact water supplies, hydroelectric power, and crop yields as El Niño continues into 2016. Parts of Chile remained in a severe 6-year drought in 2015 despite wetter El Niño conditions (www.cr2.cl/megasequía).

Drought conditions developed in some Central American and Caribbean nations, such as Guatemala and Haiti, contributing to food insecurity in the region. California continued to experience severe or extreme drought conditions, while most of the U.S. Midwest, South, and East were moderately or very wet, extending into Ontario, Canada.

Dry conditions were widespread across Australia, continuing from 2014. Severe or extreme drought conditions were apparent along the west coast, the southeast, and parts of Queensland, a region particularly susceptible to drought during protracted El Niño events, like the current one (section 2e1). Farther north, dry conditions were established across many parts of the Maritime Continent and parts of Southeast Asia, especially Myanmar and southwestern China (Plate 2.1p). Drought also affected parts of northern China and Mongolia in 2015 according to the scPDSI metric. In contrast with 2014, drought conditions were not evident in India despite a dry monsoon season. This was due to heavy out-of-season rainfall both early and late in the year. Dry conditions were, however, apparent over many Middle East countries.

In Europe, there was a strong contrast between the wet conditions of the southeast and Turkey and the severe drought indicated by scPDSI in eastern Europe and western Russia, affecting important crop production regions. Though not apparent in the annual-mean scPDSI (Plate 2.1p), July to December was very dry in Turkey, consistent with the strong positive North Atlantic Oscillation in late 2015 (sections 2e1, 7f).

The expansion in drought-affected areas during 2015 is similar to the earlier expansion during 1982 (Figs. 2.28, 2.29a), also a year when a strong El Niño developed, and is consistent with the reduction in the atmospheric transport of moisture from oceans to land during El Niño events (Dai 2013). The patterns of scPDSI drought (Plate 2.1p) correspond partly to those regions where El Niño events are associated with reduced rainfall (southeastern Africa, northeastern Australia, the Maritime Continent, and northeastern Brazil). There is weaker agreement with the 1997 pattern (Fig. 2.29b), which had less extensive droughts than in 2015, contributing to the absence of a clear signal in drought-affected area during the

SIDEBAR 2.1: **GLOBAL LAND EVAPORATION**—D. G. MIRALLES, B. MARTENS, A. J. DOLMAN, C. JIMÉNEZ, M. F. MCCABE, AND E. F. WOOD

Evaporation of water from soils, snow-covered surfaces, continental water bodies, and vegetation (either via transpiration or interception loss) accounts for approximately two-thirds of continental precipitation. As such, land evaporation represents a key mechanism governing the distribution of hydrological resources, spanning catchment to planetary scales. The ability to monitor land evaporation dynamics is also critical in climatological applications, since evaporation 1) represents the exchange of latent energy from land to atmosphere, directly affecting air temperature; 2) influences air humidity and cloud formation, playing a strong role in driving atmospheric feedbacks; and 3) is intrinsically connected to photosynthesis, echoing changes in vegetation carbon fixation. A number of recent studies have highlighted the impact of evaporation on climate trends (e.g., Douville et al. 2013; Sheffield et al. 2012) and hydrometeorological extremes (e.g., Teuling et al. 2013; Miralles et al. 2014a).

To date, land evaporation cannot be observed directly from space. However, a range of approaches have been proposed to indirectly derive evaporation by applying models that combine the satellite-observed environmental and climatic drivers of the flux (e.g., Price 1982, Nemani and Running 1989; Anderson et al. 1997; Su 2002). Pioneering efforts targeting the global scale (Mu et al. 2007; Fisher et al. 2008) have been advanced by international activities to further explore and develop global datasets, such as the European Union Water and global Change (WATCH) project, the LandFlux initiative of the Global Energy and Water-cycle Exchanges (GEWEX) project, and the European Space Agency (ESA) Water Cycle Multi-mission Observation Strategy (WACMOS)-ET project.

Nonetheless, continental evaporation remains one of the most uncertain components of Earth's energy and water balance. Both the WACMOS-ET and LandFlux projects have brought to light the large discrepancies among widely used, observation-based evaporation datasets, particularly in semiarid regimes and tropical forests (e.g., Michel et al. 2016; Miralles et al. 2016; McCabe et al. 2016). Figure SB2.1 displays the spatial variability of land evaporation over the 2005–07 period based on data from the Penman–Monteith model that forms the basis of the official MODIS product (PM–MOD; Mu et al. 2007), the Priestley and Taylor Jet Propulsion Laboratory model (PT–JPL; Fisher et al. 2008), the Model Tree Ensemble (MTE; Jung et al. 2010), and the Global Land Evaporation Amsterdam Model (GLEAM; Miralles et al. 2011). The ERA-Interim reanalysis (Dee et al. 2011) is also included for comparison. Global estimates range between the low values of PM–MOD and the high values of ERA-Interim, with the remaining models showing a higher degree of spatial agreement.

Records of observation-based global evaporation only span the satellite era. This has not prevented a handful of studies from attempting to disentangle the impact of climate change on trends in evaporation. Jung et al. (2010) suggested a reversal in the rise of evaporation since the late 1990s, which was later shown to be a temporary anomaly caused by ENSO (Miralles et al. 2014b). Nonetheless, these studies, together with more recent contributions (Zhang et al. 2015, 2016), have indicated the existence of a slight positive trend over the last few decades, in agreement with expectations derived from temperature trends and global greening, and the theory of an accelerating hydrological cycle.

Although many of the models used for global flux estimation were originally intended for climatological-scale studies, some have evolved to provide estimates of evaporation in operational

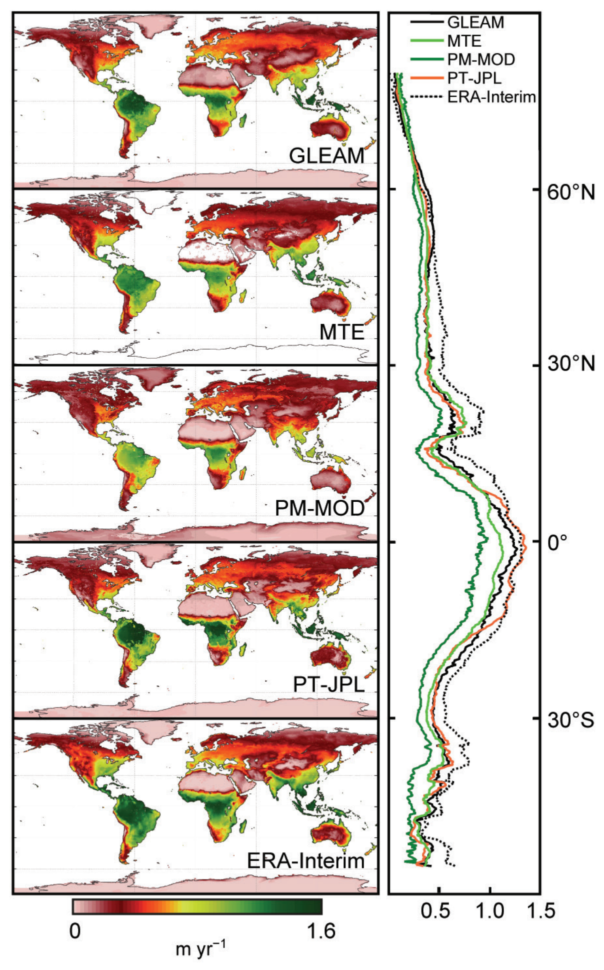

Fig. SB2.1. Mean land evaporation patterns for different datasets. The right panel illustrates the latitudinal averages over the 2005–07 period. Adapted after Miralles et al. (2016).

mode, with ongoing efforts aiming to reduce product latency and improve spatial resolution. This opens up a range of possible applications, from global drought monitoring to irrigation management. Some examples of evaporation datasets targeting near-real-time simulation at continental scales include the Land Surface Analysis Satellite Applications Facility (LSA SAF) product (Ghilain et al. 2011) and the Atmosphere–Land Exchange Inverse (ALEXI) datasets (Anderson et al. 1997, 2011). While GLEAM was not deliberately designed with an operational intent, the current version 3 dataset has been updated to include 2015, using observations from the Soil Moisture and Ocean Salinity (SMOS) mission (www.gleam.eu). Figure SB2.2 shows the anomalies in evaporation for 1980–2015 based on this new dataset.

Periods of global decline in evaporation typically coincide with El Niño conditions, and are associated with drought in the water-limited ecosystems of the Southern Hemisphere (Miralles et al. 2014b). The year 2015 was no exception: despite El Niño conditions intensifying only in the second half of 2015, Fig. SB2.2 shows anomalously low evaporation in central Australia, eastern South America, Amazonia, and southern Africa. Considering the entire multidecadal record, the continental evaporation in 2015 does not seem particularly anomalous, as climate variability is superimposed on a positive trend of ~0.4 mm yr^{-1}. For most of the Northern Hemisphere, evaporation was above the multidecadal mean, with the notable exception of California, which experienced extraordinary drought conditions.

With the development of improved algorithms dedicated to estimating evaporation from satellite observations, global operational monitoring of land evaporation is becoming a realistic proposition. While discrepancies amongst current models are still large (Michel et al. 2016; McCabe et al. 2016), several of the existing datasets compare well against each other and against in situ measurements. These datasets open new pathways to diagnose large-scale drought and irrigation needs, and to improve water resources management and the characterization of hydrological cycles. Satellite-based evaporation estimates respond to long-term changes in Earth's water and energy budgets and are able to capture fluctuations due to internal climate variability. The mean distribution of evaporation anomalies in 2015 (Fig. SB2.2) is a clear example of the underlying effects of multidecadal climate trends and climate oscillations on the terrestrial water cycle.

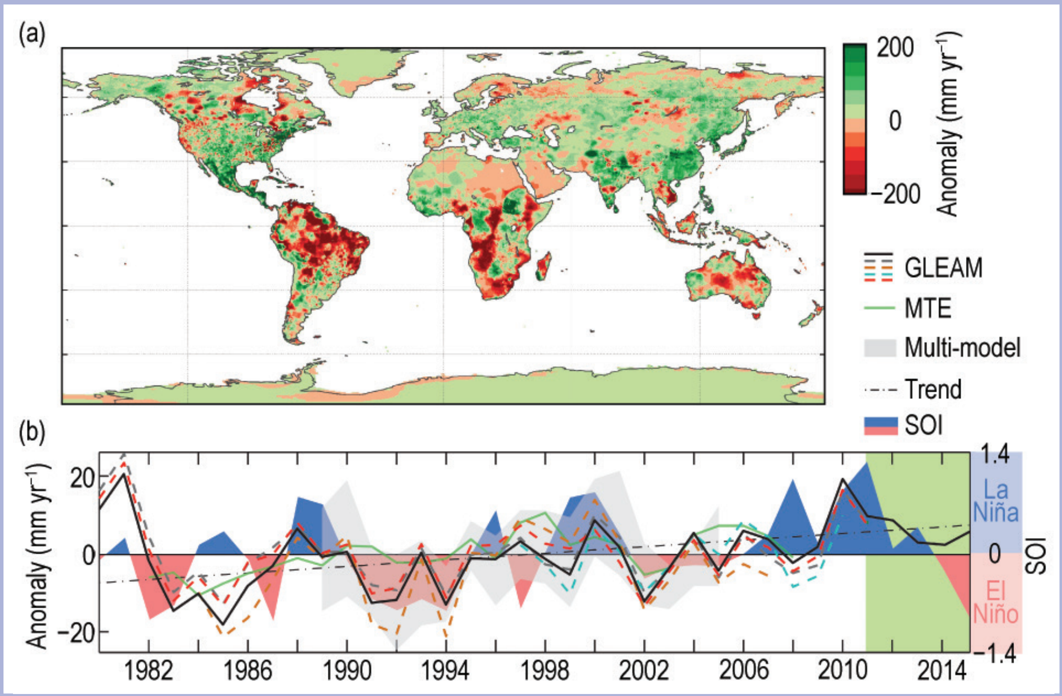

Fig. SB2.2. (a) 2015 land evaporation anomalies. (Source: GLEAM). (b) Mean continental evaporation anomaly time series for the satellite era, based on an ensemble of GLEAM datasets (after Miralles et al. 2014b). The MTE dataset (Jung et al. 2010), the satellite-based multimodel range by Mueller et al. (2013), and the Southern Oscillation index (SOI) are also shown. GLEAM runs for 2012–15 incorporate SMOS data. Anomalies are calculated relative to the 1997–2007 period in which all datasets overlap.

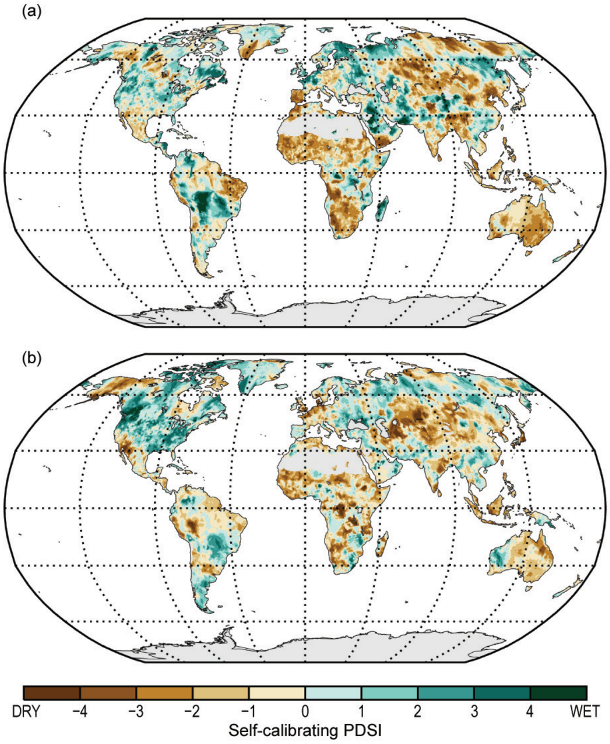

Fig. 2.29. Mean scPDSI for (a) 1982 and (b) 1997, years in which a strong El Niño developed. No calculation is made (gray areas) where a drought index is meaningless (e.g., ice sheets and deserts with approximately zero mean precipitation).

strong 1997/98 El Niño (Fig. 2.28). Indeed, the other post-1950 years with scPDSI drought areas as large as in 2015 (31% in moderate drought; e.g., 1985 and 1987) have quite different spatial patterns (Online Fig. S2.19), with severe drought in the Sahel and India, for example; 1985 was not a strong El Niño while 1987 was part of the long 1986/87 event.

e. *Atmospheric circulation*

1) Mean sea level pressure and related modes of variability—R. Allan and C. K. Folland

Mean sea level pressure (MSLP) provides diagnostics of the major modes of variability that drive significant weather and climate events (Kaplan 2011). Arguably, the most globally impactful mode is the El Niño–Southern Oscillation (ENSO), for which the sea level pressure-derived Southern Oscillation index [SOI; Allan et al. 1996; normalized MSLP difference between Tahiti and Darwin (various other indices are also commonly used); Kaplan 2011; section 4b] is an indicator. For 2015, the SOI was negative, indicating the presence of the strongest El Niño since 1997/98 (see Sidebar 1.1).

The SOI trace since 2009 highlights the shift from El Niño to strong La Niña conditions around mid-2010, continuation as a protracted La Niña (with cold SST anomalies in the Niño-4 region) until its demise in early 2012, and then near-normal conditions until early 2013. Mainly positive (La Niña–type) values followed until a swing to negative (El Niño–type) conditions since early 2014 (Fig. 2.30; with warm SST anomalies in the Niño-4 region). Apart from April and May 2014, the SOI was negative from February 2014 onwards (Fig. 2.30). Accordingly, the Niño-3 and 4 regional SST anomalies have been positive since April and February 2014 respectively (section 4b). Following Allan and D'Arrigo (1999), by these measures this constitutes a protracted El Niño episode: "*…periods of 24 months or more when the SOI and the Niño 3 and 4 SST indices were of persistently negative or positive sign, or of the opposite sign in a maximum of only two consecutive months during the period….*" Figure 2.30 shows the presence of these protracted El Niño and La Niña episodes in the SOI record since 1876, demonstrating that they can last up to six years (e.g., the 1990–95 protracted El Niño; see Gergis and Fowler 2009).

Major El Niño and La Niña events can be near-global in their influence on world weather patterns, owing to ocean–atmosphere interactions across the Indo-Pacific region, with teleconnections to higher latitudes in both hemispheres. Protracted El Niño and La Niña episodes tend to be more regional in

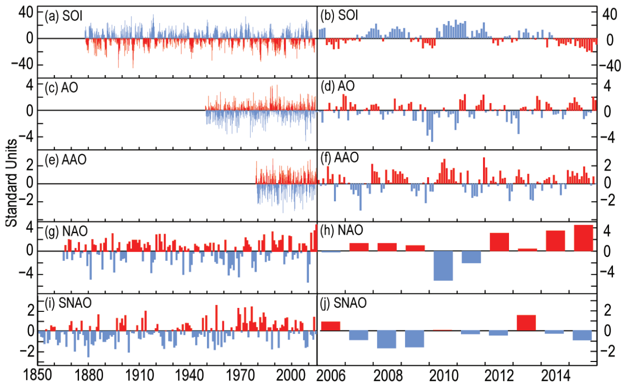

Fig. 2.30. Time series for modes of variability described using sea level pressure for the (left) complete period of record and (right) 2006–15. (a),(b) Southern Oscillation index (SOI) provided by the Australian Bureau of Meteorology; (c),(d) Arctic Oscillation (AO) provided by NCEP Climate Prediction Center; (e),(f) Antarctic Oscillation (AAO) provided by NCEP Climate Prediction Center; (g),(h) Winter (Dec–Feb) North Atlantic Oscillation (NAO) average provided by NCAR (presented for early winter of each year so winter 2015/16 is not shown); (i),(j) Summer (Jul–Aug) North Atlantic Oscillation (SNAO) average (Folland et al. 2009).

their impacts (Allan and D'Arrigo 1999; Allan et al. 2003). The main influence appears to be periods of persistent drought (widespread flooding) in Queensland, Australia, which often occur during protracted El Niño (La Niña) episodes (Murphy and Ribbe 2004). The dry 2014/15 across much of Queensland reflects this latest protracted El Niño episode (section 2d9).

More regionally, the Arctic Oscillation (AO), North Atlantic Oscillation (NAO), and the Antarctic Oscillation (AAO) indices can also be derived from mean sea level pressure. In the Northern Hemisphere, the last five boreal winters have displayed broadly positive NAO conditions but a diverse range of circulation patterns. In the winter of 2013/14, a strong northeastward-displaced North Pacific anticyclone (Fig. 2.31a) was accompanied by a positive AO and a deep trough over central Canada and the United States. The subtropical jet stream was enhanced and displaced southward, extending across the Atlantic to the United Kingdom and Europe under strong positive NAO conditions (Fig. 2.31d). This led to severe cold winter conditions across much of the United States and a succession of major midlatitude storms being steered across the Atlantic to Ireland and the United Kingdom. By contrast, during the 2014/15 boreal winter the North Pacific anticyclone was weaker and the Aleutian low was prominent (Fig. 2.31b). The exceptional storm track from the United States to Europe in the 2013/14 boreal winter was not evident in 2014/15. During early winter of 2015/16, a deep trough over the North Atlantic led to an enhanced jet stream that directed a series of extratropical cyclones towards northern Ireland and Scotland–northern England (Figs. 2.31c,f). By the mid-to-latter part of the 2015/16 winter, the pattern had changed, with the Aleutian low enhanced and troughing over the North Atlantic–northern Europe. Midlatitude storm tracks were displaced farther north.

In the Southern Hemisphere, the AAO was in its positive phase during 2015/16 (Fig. 2.30), which favors reduced sea ice extent in the West Antarctic Peninsula (WAP) region, owing to enhanced westerly wind conditions (Stammerjohn et al. 2008). During the current situation, however, the WAP sea ice margins were extended (http://nsidc.org/data/seaice_index/), because in the interplay between the protracted El Niño, which should favor a weaker polar jet stream, and the positive AAO mode, with stronger westerly winds, the former appeared to have dominated. Related positive wind speed anomalies were noted at 850 hPa (section 2e3) over the midlatitude Southern Ocean.

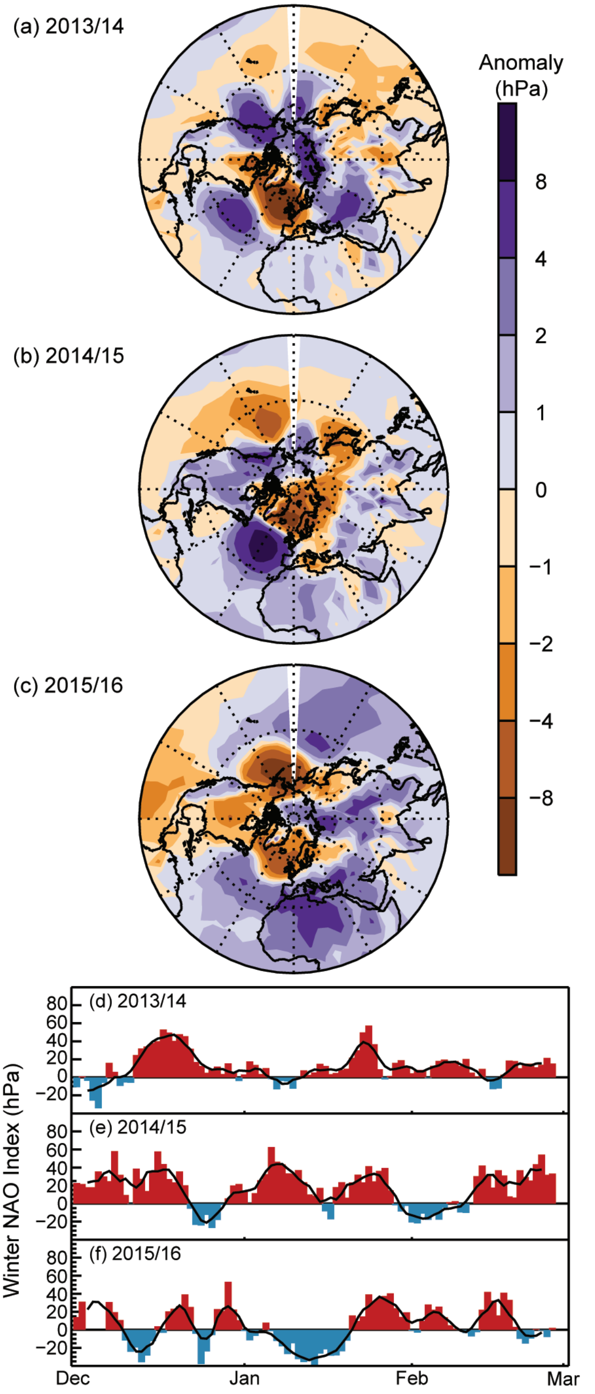

Fig. 2.31. Boreal winter sea level pressure anomalies (hPa, base period: 1981–2010) averaged over Dec–Feb for (a) 2013/14, (b) 2014/15, and (c) 2015/16. NAO daily time series (hPa) for winter (d) 2013/14, (e) 2014/15, and (f) 2015/16. The 5-day running mean is shown by the solid black line. The data are from HadSLP2r (Allan and Ansell 2006).

In 2015, the summer NAO (SNAO), defined over July and August as in Folland et al. (2009), continued its marked tendency to a more negative state in the last decade. Only 2013 was a prominent exception. The irregular decline in the SNAO index since its peak in the 1970s is striking (Fig. 2.30i). A negative state of the SNAO is consistent with generally strongly positive Atlantic multidecadal oscillation conditions over the last decade (Sutton and Dong 2012). However, evidence is strengthening that reductions in summer Arctic sea ice due to warming of the Arctic may also favor a negative SNAO (e.g., Knudsen et al. 2015, Petrie et al. 2015). The July 2015 MSLP anomaly pattern strongly resembled the negative SNAO. Although August also projected weakly onto the negative SNAO, Scandinavia had a high pressure anomaly with very warm temperatures over and to its south (Figs. 2.32a, b). Daily SNAO values reflect the somewhat different characters of July and August (Fig. 2.32c), with fewer days of negative SNAO in August. Despite this, the Central England Temperature (Parker et al. 1992) was close to its 1961–90 normal in both months. The HadCRUT4 temperature for July and August (Online Fig. S2.20) shows that central England was on the boundary between warmer-than-normal conditions over most of Europe and distinctly cool conditions in the central extratropical North Atlantic Ocean. The latter is consistent with the July and August MSLP anomalies, but its strength may also reflect a persistent tendency to cool conditions in this region over the last few years. The pattern of rainfall anomalies varied consistently with MSLP patterns between July and August; most of northwestern Europe had above-average rainfall in July, with most of southern Europe drier than normal. In August, most of Scandinavia and eastern Europe were drier than normal, with a more restricted wet area than in July extending from Ireland through France to the Netherlands (section 7f; Online Fig. S2.21).

(a) Jul 2015

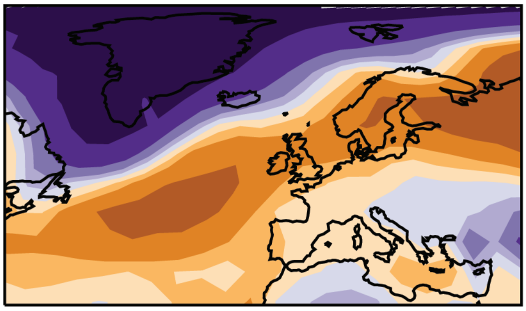

(b) Aug 2015

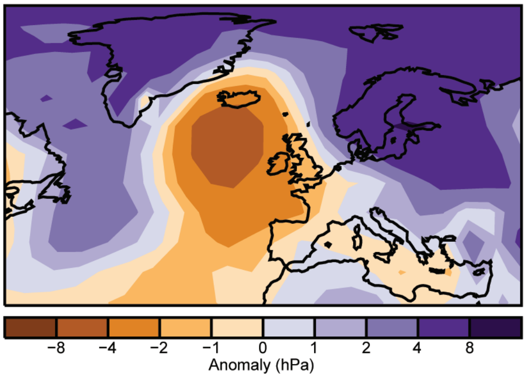

(c) Summer NAO Index

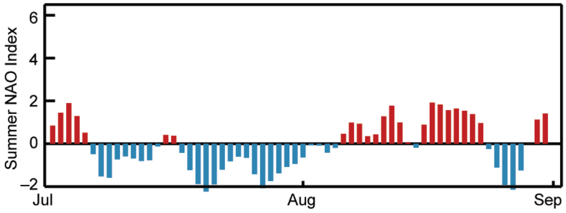

Fig. 2.32. HadSLP2r mean sea level pressure anomalies for Europe for (a) Jul and (b) Aug 2015. (c) EMULATE PMSL daily SNAO time series for Jul–Aug 2015 normalized over 1850–2015.

2) Surface winds—R. J. H. Dunn, C. Azorin-Molina, C. A. Mears, P. Berrisford, and T. R. McVicar

During 2015, over land, observational datasets have revealed generally higher surface wind speeds (Plate 2.1s; Fig. 2.33a) than in the last 20 years. This "recovery" continues the behavior observed since 2013 and concurs with Kim and Paik (2015), who reported a break from the decreasing trend in surface wind speed around the Republic of Korea during the most recent decade.

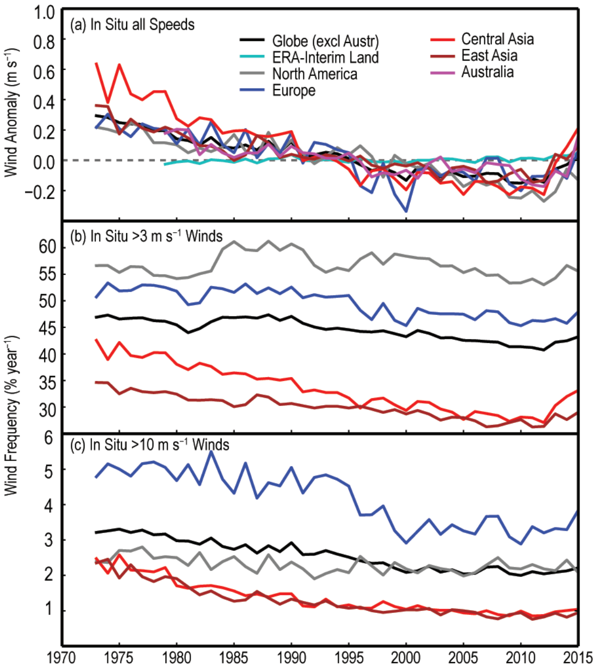

Fig. 2.33. Global (excluding Australia) and regional annual time series of land surface wind speed for 1981–2015 using HadISD and ERA-Interim showing (a) wind speed anomaly (m s^{-1}) relative to 1981–2010, and occurrence frequencies (in %) for wind speeds (b) >3 m s^{-1} and (c) >10 m s^{-1}. Frequencies for Australia are not shown in (b) and (c).

The observed global (excluding Australia) average anomaly from the 1981–2010 climatology was +0.025 m s^{-1} (Table 2.5) compared to −0.030 m s^{-1} in 2014. As a result of unresolved differences between the two observing systems used in Australia (wind run, compared to wind speed in HadISD), and given agreement of modeling pan evaporation trends when using wind run (Roderick et al 2007), Australia is treated separately and the wind run results updated from McVicar et al. (2008) are used. In Australia, the positive anomaly made 2015 the fourth windiest year in the 1979–2015 record. There were positive anomalies in all other regions, with the exception of a noticeable negative anomaly in North America. Over this latter region, 2015 was the ninth calmest year in the observed record, with a slightly lower occurrence of both moderate (>3 m s^{-1}) and strong (>10 m s^{-1}) winds (Figs. 2.33b,c), in agreement with Iacono and Azorin-Molina (2014). Overall increases in Europe, central Asia, and East Asia reflected a higher occurrence of moderate winds, and particularly of strong winds in Europe (Fig. 2.33b,c).

Adapting the approach of Berrisford et al. (2015), two quality-controlled wind speed datasets from instrumental records are used: 1) the global HadISD (1973–2015, Dunn et al. 2012), with the highest station density in the Northern Hemisphere, and 2) an Australian database (1979–2015, McVicar et al. 2008). The 10-m wind speed fields from ERA-Interim (Dee et al. 2011) are also used to investigate the spatial and temporal variability of winds over regions that have few observations. Over land surfaces with high-density wind observations, the large-scale anomaly patterns from ERA-Interim (Plate 2.1s) are relatively consistent with the instrumental records. Reanalysis products provide contiguous global information but have shortcomings in their representation of surface layer processes and hence near-surface winds speeds (see McVicar et al. 2008; Pryor et al. 2009; Vautard et al. 2010 for examples). In addition, reanalyzed winds are representative of larger spatial and temporal scales than point observations.

The percentage of stations showing positive and negative anomalies in 2015 from HadISD is split almost evenly, with a slight dominance of stations with positive anomalies. At 15% of the stations, the wind speed was at least 0.5 m s^{-1} above the 1981–2010 climatology while it was at least 0.5 m s^{-1} below it at 11% of the stations. The wind speed was at least 1.0 m s^{-1} above and below the climatology at 3.4% and 2.3% of stations, respectively.

Continentally, negative long-term trends of observed land surface wind speed dominate over 1979–2015, with a terrestrial global (excluding Australia) change of −0.087 m s^{-1} decade^{-1}, varying from −0.070 (East Asia) to −0.151 (Central Asia) m s^{-1} decade^{-1} (Table 2.5, Fig. 2.34), with Australia at −0.062 m s^{-1} decade^{-1}. Although the ERA-Interim pattern of reanalyzed trends (Fig. 2.34) is consistent with the observational HadISD dataset, the magnitude of changes is underestimated, as previously noted for other reanalysis products (McVicar et al. 2008;

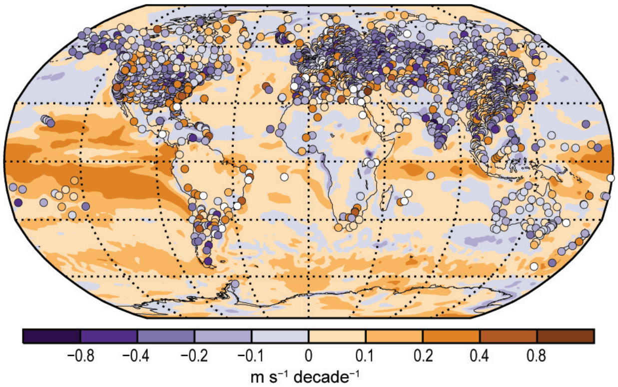

Fig. 2.34. Land surface wind speed trends for the observational HadISD and Australian datasets (points) and the ERA-Interim reanalysis (worldwide grids) over 1979–2015.

Table 2.5. Global and regional statistics for land surface wind speed using observational HadISD and Australian (McVicar et al. 2008) datasets.

Region	Mean 1981–2010 (m s^{-1})	Anomaly 2015 (m s^{-1})	Trend 1979–2015 (m s^{-1} decade^{-1}) and 5th to 95th percentile confidence range	Number of stations
Globe (excluding Australia)	3.309	+0.025	−0.087 (−0.094)–(−0.081)	2264
North America	3.685	−0.130	−0.100 (−0.111)–(−0.088)	587
Europe	3.747	+0.063	−0.087 (−0.100)–(−0.071)	589
Central Asia	2.887	+0.212	−0.151 (−0.162)–(−0.133)	263
East Asia	2.623	+0.092	−0.070 (−0.079)–(−0.060)	399
Australia	2.066	+0.160	−0.062	41

Pryor et al. 2009; Vautard et al. 2010). This worldwide slowdown of land surface wind speed observed since the 1980s has been reported over many regions (see McVicar et al. 2012 for a review).

The precise causes of this weakening in wind speed remain largely uncertain and do not necessarily reflect wind tendency at higher altitudes (McVicar and Körner 2013) than the standard 10-m observations (Vautard et al. 2010; Troccoli et al. 2012). Increase of surface roughness due to forest growth, land use changes, and urbanization (Vautard et al. 2010; Bichet et al. 2012; Wever 2012; Wu et al. 2016); changes in large-scale atmospheric circulation (Azorin-Molina et al. 2014, 2016); instrumentation changes (Wan et al. 2010); and air pollution (Xu et al. 2006) are among the major identified hypothetical causes, which differ in importance regionally. Unlike the long-term declining trend over land, there is an apparent reversal of the trends since 2013, but still with overall negative anomalies.

Over oceans, estimates of globally-averaged wind obtained from satelliteborne microwave radiometers (Wentz 1997; Wentz et al. 2007) were slightly lower than average in 2015 (Fig. 2.35). Estimates from reanalysis products differ, with JRA-55 and ERA-Interim showing that 2015 was above average, and MERRA-2 showing the opposite. Reanalysis winds, which are in relatively good agreement with both the satellite data and each other from 1990 to 2009, diverge after 2010 (Figs. 2.35a–c). A comparison of annual mean anomaly global ocean average wind speed between ERA-Interim and satellite radiometers shows moderate agreement on short time scales and poorer agreement on long time scales, with the ERA-Interim results showing a larger long-term increasing trend. All products show an increasing trend from 1990 to 2007, followed by a drop-off in 2008–09, and a recovery in 2010. Since then, the winds have fallen slightly in most products.

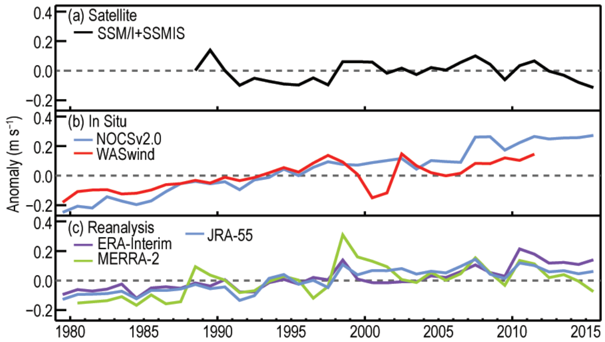

Fig. 2.35. Global average surface wind anomaly over ocean relative to the 1981–2010 base period from (a) satellite radiometers, (b) ships, and (c) reanalyses (as described in Fig. 2.1).

During 2015, ocean winds showed large negative anomalies in the central tropical Pacific associated with the ongoing El Niño event (Plate 2.1s), similar to those found above the surface at 850 hPa (Plate 2.1r). This weakening was most apparent in the latter half of 2015. Compared to the 1997/98 El Niño, the region of weakening did not extend as far east, and Indian and Atlantic Ocean patterns were much less striking (Online Fig. S2.22). Other regions with negative anomalies include much of the tropical Indian Ocean and the southern Pacific midlatitudes between New Zealand and Chile. Other regions of the Southern Ocean showed positive anomalies, which were also present in the western Pacific surrounding the Maritime Continent and in the eastern tropical Pacific south of the equator. Over land, the anomalies were less pronounced, with most land areas showing small positive anomalies.

3) Upper air winds—L. Haimberger and M. Mayer

Upper air wind is measured routinely with balloons and aircraft. Today it is also inferred from satellite imagery, at least in the lower to midtroposphere. Historical upper air wind data are particularly crucial for detecting signals associated with meridionally asymmetric aerosol forcing (Allen et al. 2014), for example, or with ENSO.

The buildup of a strong El Niño event was one of the major large-scale climate anomaly signals in 2015. There are many ways to depict this event, but it is useful to see its impact on upper level divergent flow. Figure 2.36 compares divergent wind anomalies at 200 hPa in late 2015 (3-month average centered around November 2015 to maximize the signal) with those from the strongest ENSO event in recent history (also centered around November 1997). The divergent flow of the 2015 event, while having the strongest divergence maximum east of the date line, was much more confined to the tropical Pacific than was the case in 1997, where the flow patterns over the whole tropics were massively perturbed. Regions with divergent flow are associated with deep convection and strong thermodynamic coupling between sea surface and the atmosphere, which also has a strong imprint on regional-scale energy flows (Mayer et al. 2013, 2014). Regions with strong convergence at this level are associated with large-scale subsidence and suppressed convection.

As may be expected (Zhang and Zhu 2012), this pattern fits well with the activity pattern of tropical cyclones in late 2015. There was an all-time record of 13 tropical cyclones in the central Pacific and enhanced tropical cyclone activity in the east Pacific (www.nhc.noaa.gov/text/MIATWSEP.shtml; see section 4e3). It is also interesting to note that the anomalous divergence pattern over the Arabian Sea coincided with the occurrence of two strong tropical cyclones in this region (on average there is less than one tropical cyclone per year), affecting Yemen and Oman (see section 4e5). Tropical cyclone activity over the western Pacific (which is the region of strongest divergence in the climatological mean) and Atlantic was normal or below normal. This can be seen in Fig. 2.36a from the locations of peak intensities of tropical cyclones that reached at least Category 1 on the Saffir–Simpson scale. The near-average cyclone activity in the western Pacific can partly be explained by cyclones originating in the central Pacific that reached peak intensity farther west.

The upper level convergence over Indonesia and particularly Australia in late 2015 is also consistent with the observed severe drought conditions over parts of these regions (see Fig. 2.29). As can be seen from Fig. 2.36, the upper level divergence pattern is generally less perturbed in 2015 than in 1997. If the RMS of the divergent wind speed in the tropics is used as a measure, it was 1.4 m s^{-1} in late 1997 compared to 1.3 m s^{-1} in late 2015. Nevertheless, its spread over the whole tropics is remarkable.

The imprint of the 2015 El Niño event can also be seen in the 850-hPa wind speed anomaly map in Plate 2.1r. There is a distinct weakening of the tropical easterlies just west of the upper level divergence maximum in Fig. 2.36a or the SST anomaly maximum in Plate 2.1c. Other features of the anomaly map are a slight poleward shift of Southern Hemisphere midlatitude westerlies that leads to enhanced wind speeds over the seas adjacent to Antarctica. These are likely related to the positive phase Antarctic Oscillation (AAO) during 2015 (section 2e1), and possibly enhanced through the exceptionally warm troposphere farther equatorward (Plate 2.1b). The positive wind speed anomaly over the eastern North Atlantic is consistent with the positive phase of the North Atlantic Oscillation (NAO) prevailing in 2015 (section 2e1).

Radiosonde and pilot balloon are the best sources for station-based upper air wind climatologies, dating back to the early 1940s in the northern extratropics. Maps of upper air winds are best inferred from atmospheric reanalyses, which are well constrained by observations. It is difficult to get wind climatologies from satellite data because the altitude of observations (mostly cloud-based atmospheric motion vectors) is highly variable. Since last year's article, early upper air data have been assimilated in an experimental reanalysis run called ERA-preSAT (1939–67, H. Hersbach et al. 2016,unpublished manuscript) which helped to extend the quasi-biennial oscillation (QBO) time series from reanalyses backward in time to at least the late 1940s.

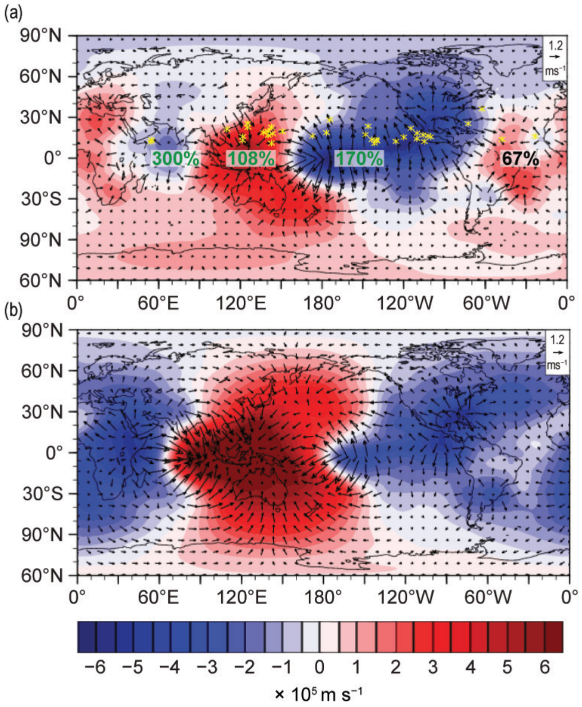

Fig. 2.36. Three-month averages of velocity potential and divergent wind at 200 hPa compared to the 1979–2014 climatology. Anomalies centered around (a) Nov 2015 and (b) Nov 1997. On panel (a) crosses indicate location of peak intensities for Category 1 or higher tropical cyclones in second half of 2015. Percentage of tropical cyclone frequency compared to the National Hurricane Center's 1966–2009 climatology is also indicated.

Figure 2.37 shows time series of zonal belt mean wind speeds in the tropics at 50 hPa to cover the QBO signal. The experimental ERA-preSAT shows potential to extend reanalysis time series backward in a more realistic manner than the surface data only reanalyses (Haimberger 2015). The depiction of the QBO signal back to the early 1950s is particularly encouraging. There are practically no digitized upper air data prior to the early 1950s reaching high enough altitudes in the tropical belt.

f. Earth radiation budget

1) EARTH RADIATION BUDGET AT TOP-OF-ATMOSPHERE—

P. W. Stackhouse, Jr., T. Wong, D. P. Kratz, P. Sawaengphokhai, A. C. Wilber, S. K. Gupta, and N. G. Loeb

The Earth's radiation budget (ERB) at the top-of-atmosphere (TOA) is the balance between the incoming total solar irradiance (TSI) and the sum of the

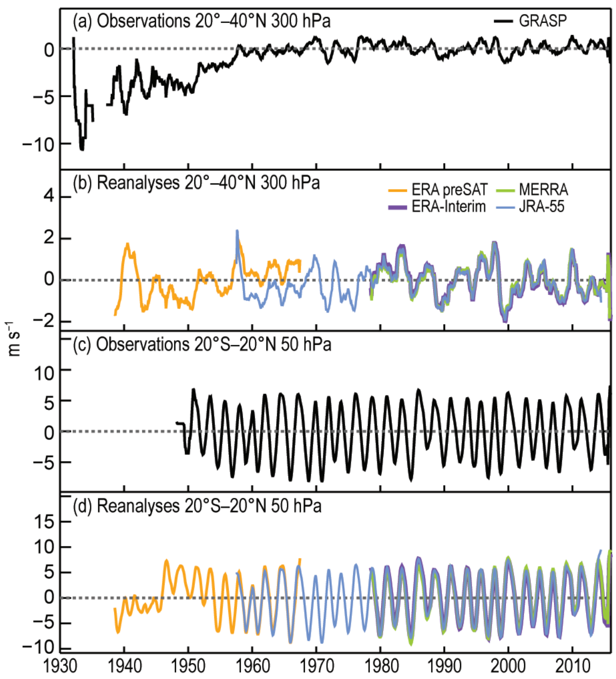

Fig. 2.37. Time series of zonal mean U-wind component in the (a) 20°–40°N belt at 300 hPa and (b) tropical belt 20°S–20°N at 50 hPa, calculated from ERA-Interim, MERRA, JRA-55, and ERA-preSAT reanalyses and pilot balloon/radiosonde winds (GRASP; Ramella-Pralungo et al. 2014). Note that positive (negative) changes in the zonal wind sped imply an increase in westerlies (easterlies). Data have been smoothed using a 12-point boxcar filter.

reflected shortwave (RSW) and outgoing longwave radiation (OLR). This balance defines the energetic state of the Earth–atmosphere system that drives weather processes, climate forcing, and climate feedbacks.

The year 2015 is remarkable due to the development of an intense El Niño that reached official status in April–May according to the multivariate ENSO index (MEI; Wolter and Timlin 1993, 1998; www.esrl.noaa.gov/psd/enso/mei/) and intensified into late 2015. Note that the MEI index is more appropriate than the SOI for comparing to radiative fluxes because it integrates information from across the Pacific. In contrast, 2013 was a neutral year while 2014 featured a slight shift from typical east–west Pacific conditions toward El Niño, becoming "marginal" by year end. Global annual mean OLR in 2015 increased ~0.15 W m^{-2} since 2014, but was ~0.30 W m^{-2} larger than for 2013 (Table 2.6). Meanwhile, the global-annual mean RSW decreased by ~0.45 W m^{-2} from 2014 and was ~0.75 W m^{-2} smaller than for 2013. In 2015, the global annually-averaged TSI was ~0.05 W m^{-2} larger than that of both 2013 and 2014. The combination of these components amounts to an addition of 0.40 W m^{-2} in the total net radiation into the Earth climate system relative to 2014 and corresponded to a ~0.50 W m^{-2} increase relative to 2013. All the global annual mean changes appear to be amplifying relative to the neutral ENSO year of 2013, perhaps indicative of the atmospheric response due to the circulation anomalies over the last two years. Relative to the 2001–14 average, the 2015 global annual mean flux anomalies (Table 2.6) are +0.30, +0.10, −0.55, and +0.35 W m^{-2} for OLR, TSI, RSW, and total net flux, respectively. These changes, except for the RSW anomaly, are within the corresponding 2-sigma interannual variability (Table 2.6) for this period and thus not viewed as particularly large anomalies. The 2015 global annual mean RSW flux anomaly greatly exceeds typical variability, implying a darkening of Earth's TOA albedo. Attribution of this to El Niño and/or other large-scale processes requires further analysis. However, it appears that reduction of the annually averaged RSW is resulting in a relative increase to the total net absorbed flux of the Earth–atmosphere system, indicating a net heating over the last two years.

Table 2.6. Global-annual mean TOA radiative flux changes between 2013 and 2015, 2014 and 2015, the 2015 global-annual mean radiative flux anomalies relative to their corresponding 2001–14 mean climatological values, and the 2-σ interannual variabilities of the 2001–14 global-annual mean fluxes (all units in W m^{-2}) for the outgoing longwave radiation (OLR), total solar irradiance (TSI), reflected shortwave (RSW), and total net fluxes. All flux values have been rounded to the nearest 0.05 W m^{-2}.

	Global-annual Mean Difference (2015 minus 2013) (W m^{-2})	Global-annual Mean Difference (2015 minus 2014) (W m^{-2})	2015 Anomaly (relative to climatology) (W m^{-2})	Interannual variability (2001 to 2014) (W m^{-2})
OLR	+0.30	+0.15	+0.30	±0.50
TSI	+0.05	+0.05	+0.10	±0.20
RSW	−0.75	−0.45	−0.55	±0.40
Net	+0.50	+0.40	+0.35	±0.65

Monthly mean anomaly TOA flux time series (Fig. 2.38) show that the OLR anomaly began 2015 with a value of 0.9 W m^{-2}, but then mostly oscillated between −0.2 and +0.7 W m^{-2}, which led to the slightly positive annual OLR anomaly (see Table 2.6) with higher values toward the end of 2015. This observed OLR variability is generally consistent with the NOAA-HIRS OLR (Lee et al. 2011). The absorbed shortwave (TSI – RSW) anomaly started the year with a value of 0.2 W m^{-2}, increased to just over 1.1 W m^{-2} in September, but then decreased the last few months of the year. The positive values towards the latter half of the year were large enough to dominate the annual average, leading to a large absorbed shortwave anomaly for the year. The total net anomaly, which contains the combined OLR and absorbed shortwave anomalies, began 2015 with a value of −0.7 W m^{-2}, then jumped to positive values, peaking in September at 0.9 W m^{-2} before falling below 0 W m^{-2} by the end of the year. The positive absorbed shortwave anomaly dominates the net, resulting in the positive annual total net anomaly. Long-term trend analyses that include the last two months of the merged dataset are discouraged due to the natural fluctuation in ERB components, the uncertainty from the data merging process, and potential for drift in the FLASHFlux product.

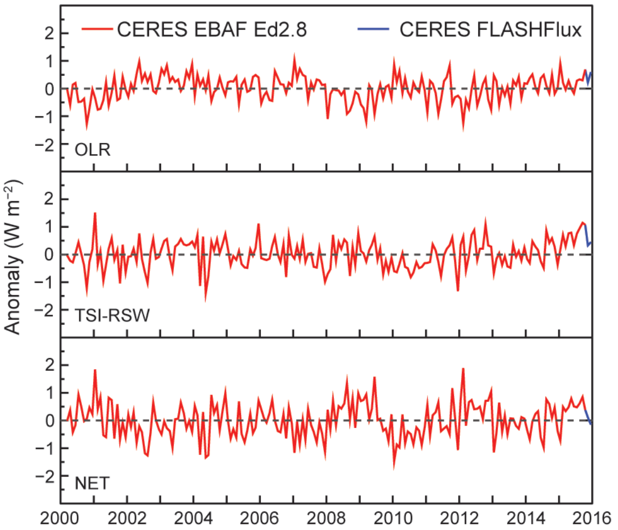

Fig. 2.38. Time series of global-monthly mean deseasonalized anomalies (W m^{-2}) of TOA earth Radiation Budget for OLR (upper panel), absorbed shortwave (TSI–RSW; middle panel), and total net (TSI–RSW–OLR; lower panel) from Mar 2000 to Dec 2015. Anomalies are relative to their calendar month climatology (2001–2014). The time series shows the CERES EBAF Ed2.8 1Deg data (Mar 2000 to Oct 2015) in red and the CERES FLASHFlux version 3B data (Nov–Dec 2015) in blue (Source: https://eosweb.larc.nasa.gov/project/ceres/ceres_table.)

TSI data are from the Total Irradiance Monitor (TIM) instrument aboard the Solar Radiation and Climate Experiment (SORCE) spacecraft (Kopp and Lean 2011) and the Royal Meteorological Institute of Belgium (RMIB) composite dataset (Dewitte et al. 2004), both renormalized to the SORCE Version 15 data. RSW and OLR data were obtained from the Clouds and the Earth's Radiant Energy System (CERES) mission (Wielicki et al. 1996, 1998), deriving flux data from the *Terra* and *Aqua* spacecraft.

Time series (Fig. 2.38) were constructed from the CERES EBAF (Energy Balanced And Filled) Ed2.8 product (Loeb et al. 2009, 2012) from March 2000 to October 2015 and the CERES Fast Longwave and Shortwave Radiative Fluxes (FLASHFlux) products (Kratz et al. 2014; Stackhouse et al. 2006), for November and December 2015. The FLASHFlux data are normalized to the EBAF data using the following procedure based on overlapping data from January 2009 through December 2014. First, successive versions of globally-averaged FLASHFlux TOA components are normalized to each other relative to the current version 3B. Then, this unified 6-year FLASHFlux dataset is cross-calibrated to the corresponding EBAF Ed2.8 data using TOA fluxes from both datasets, accounting for multiyear bias, linear change, and seasonal dependent differences. Finally, these coefficients are used to cross-normalize FLASHFlux to EBAF and provide an estimate of monthly globally averaged TOA flux components. The resulting 2-sigma monthly uncertainty of the normalization procedure for the 6-year overlap period was ±0.22, ±0.07, ±0.19, and ±0.22 W m^{-2} for the OLR, TSI, RSW, and total net radiation, respectively.

2) Mauna Loa clear-sky "apparent" solar transmission—K. Lantz

NOAA's Global Monitoring Division (GMD) maintains one of the longest continuous records of solar transmission at the Mauna Loa Observatory (MLO) in Hawaii. Because of the observatory's remote Pacific location and high elevation above local influences (3400 m a.s.l.), the solar transmission represents the free troposphere and above with limited local influences. This record is often used to show the influence of large explosive volcanic eruptions and is useful as an indicator of changes in background stratospheric aerosols. The "apparent" clear-sky solar transmission (AT) is calculated from the ratio of direct-beam broadband irradiance measurements from a pyrheliometer using fixed atmospheric paths (Ellis and Pueschel 1971). This technique is advantageous because using the ratio of fixed atmospheric paths removes influences due to extraterrestrial irradiance and instrument calibrations. Past studies of changes in clear-sky AT at MLO have looked at the influence of volcanic aerosol, aerosol transport from Asia, water vapor, ozone, and influences of the quasi-biennial oscillation (QBO; Bodhaine et al. 1981; Dutton et al. 1985; Dutton 1992; Dutton and Bodhaine 2001). Effects due to aerosol are the most prominent in the record.

The monthly record of clear-sky apparent solar transmission has been updated through December 2015 (Fig. 2.39). The monthly values are calculated using morning values to remove boundary layer influences that occur predominantly in the afternoon due to prevailing upslope wind conditions (Ryan 1997). Major eruptions from Agung, El Chichón, and Mount Pinatubo are clearly visible in the record in 1964, 1982, and 1991, respectively (Fig. 2.39). The cleanest period of observations is between 1958 and 1962, except for a brief period in 1978. As such, this period is treated as the "clean" background with which to compare all other variations (dashed line in Fig. 2.39). Seasonal trends are highlighted by a 6-month running smoothed fit to the monthly values and have been attributed primarily to Asian aerosol transport in the spring (Bodhaine et al. 1981). Long-term changes are highlighted by a 24-month running smoothed fit. The monthly clear-sky AT eventually returned to near-background conditions in mid-1998 after the eruption of Mount Pinatubo in 1991. The 24-month fit shows a slow decrease in AT over the subsequent decade (Fig. 2.39b). This slow decrease in clear-sky AT was attributed to increased stratospheric aerosol due to small volcanic eruptions (Solomon et al. 2011; Vernier et al. 2011). These eruptions have been shown to contribute aerosol to the layer between the tropopause and 15 km in mid- to high latitudes (Ridley et al. 2014). The last several years have not shown a continued increase in the clear-sky AT. There is a negligible change in the mean of the monthly clear-sky AT in 2015 with respect to 2014 (−0.0006). The amplitude of the seasonal changes in clear-sky AT in 2015 is ~0.006, which is comparable to results reported previously of ~0.007 (Bodhaine et al. 1981).

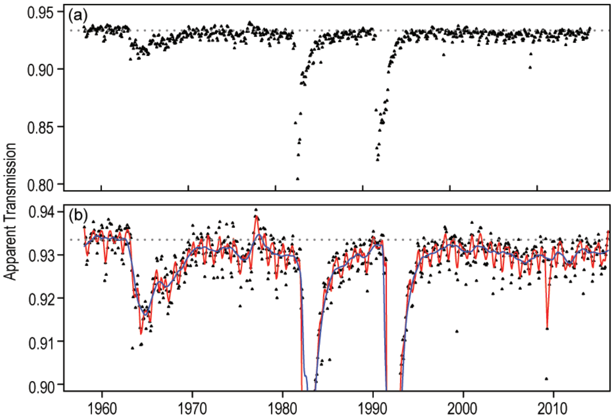

Fig. 2.39. (a) Monthly mean of the clear-sky Apparent Transmission at Mauna Loa Observatory. The dashed line is the background level from 1958 to 1972. (b) Enlarged plot to highlight the seasonal (red line, 6-month running smoothed fit) and long-term (blue line, 24-month smoothed fit) changes in the clear-sky AT record.

g. *Atmospheric composition*

1) Long-lived greenhouse gases—E. J. Dlugokencky, B. D. Hall, M. J. Crotwell, S. A. Montzka, G. Dutton, J. Mühle, and J. W. Elkins

Carbon dioxide (CO_2), methane (CH_4), and nitrous oxide (N_2O), in decreasing order, are the most dominant long-lived greenhouse gases (LLGHG) contributing to climate forcing. Systematic measurements of CO_2 began at Mauna Loa, Hawaii (MLO), in 1958, when the atmospheric mole fraction was ~315 ppm (parts per million in dry air). In 2015 the MLO annual average mole fraction of CO_2 exceeded 400 ppm (400.8 ± 0.1 ppm) for the first time (www.esrl.noaa.gov/gmd/ccgg/trends/), while the global average CO_2 mole fraction at Earth's surface was 399.4 ± 0.1 ppm (Fig. 2.40a, www.esrl.noaa.gov/gmd/ccgg/trends/global.html).

Atmospheric CO_2 growth since 1958 is largely attributable to a concurrent, fourfold increase in anthropogenic emissions from fossil fuel combustion and cement production (Boden et al. 2015). About half of this anthropogenic CO_2 remains in the atmosphere, while the other half is taken up by the terrestrial biosphere and oceans, where it acidifies seawater (see section 3l). The global growth rate of CO_2 has risen from 0.6 ± 0.1 ppm yr^{-1} in the early 1960s to an average of 2.1 ± 0.1 ppm yr^{-1} during the past 10 years. However, the increase at MLO during 2015 was 3.05 ± 0.11 ppm (0.76 ± 0.03%), the largest annual increase observed in the 56-year measurement record. The largest previous increase (2.93 ppm) occurred in 1998, which was also a strong El Niño year. ENSO plays a role in the interannual variability of the CO_2 growth rate through its influence on terrestrial carbon fluxes (Bastos et al. 2013).

Methane is emitted from both anthropogenic (60%) and natural (40%) sources (Fung et al. 1991). Anthropogenic sources include agriculture (e.g., ruminants and rice), fossil fuel extraction and use, biomass burning, landfills, and waste. Natural sources include wetlands, geological sources, oceans, and

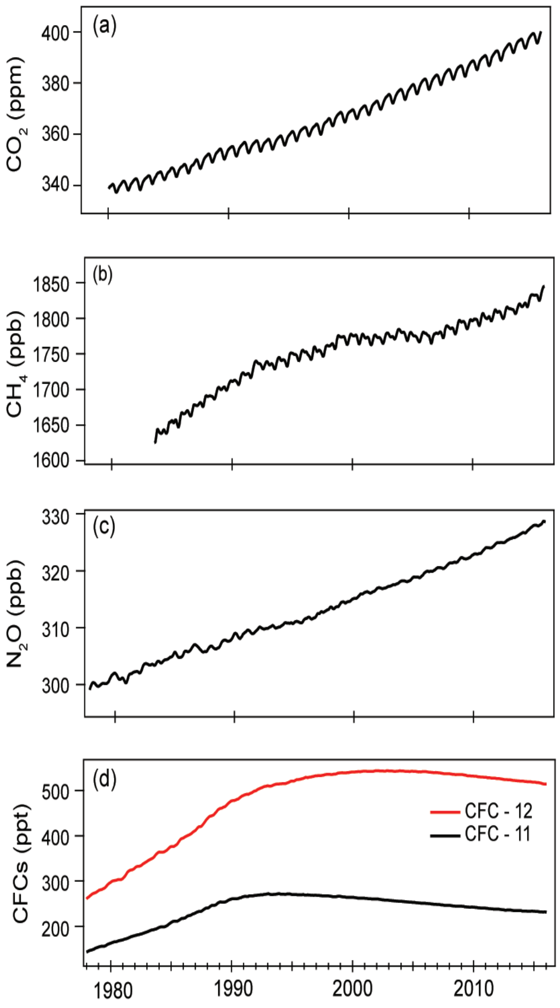

Fig. 2.40. Global mean surface mole fractions (in dry air) of (a) CO_2 (ppm), (b) CH_4 (ppb), (c) N_2O (ppb), and (d) CFC-12 and CFC-11 (ppt) derived from the NOAA sampling network.

termites (Dlugokencky et al. 2011). Fossil fuel exploitation (coal, oil, and natural gas) contributes ~20% of total global CH_4 emissions (Kirschke et al. 2013). Having increased 250% since pre industrial time, the atmospheric CH_4 burden currently contributes ~0.5 W m^{-2} direct radiative forcing, with an additional ~0.3 W m^{-2} indirect radiative forcing coming from the production of tropospheric O_3 and stratospheric H_2O from methane (Myhre et al. 2013). Total global CH_4 emissions are estimated at ~540 Tg CH_4 yr^{-1} (1 Tg = 10^{12} g), with a relatively small uncertainty of ~±10%, based on observations of globally averaged CH_4, its rate of increase, and an estimate of its lifetime (~9.1 yr). The complexity of the atmospheric CH_4 budget, with many sources that are difficult to quantify individually, makes bottom-up estimates by country and source difficult. The rate of CH_4 increase slowed from more than 10 ppb yr^{-1} in the 1980s to nearly zero in the early 2000s, then increased to an average of ~7 ppb yr^{-1} since 2007 (Fig. 2.40b). Surface observations, including its rate of increase and spatial distribution, provide strong top-down constraints on the CH_4 source and sink budgets. Based on NOAA background air sampling sites, the 2015 globally averaged CH_4 mole fraction at Earth's surface was 1834.0 ± 0.8 ppb. The 11.5 ± 0.9 ppb increase in annual means from 2014 to 2015 is the largest since 1997/98.

Nitrous oxide is a powerful greenhouse gas produced by natural (~60%) and anthropogenic (~40%) sources and is also an ozone-depleting substance (Ciais et al. 2013; Ravishankara et al. 2009). The observed 21% increase in atmospheric N_2O over preindustrial levels (270 to 328 ppb) is largely the result of nitrogen-based fertilizer use (Park et al. 2012). The mean global atmospheric N_2O mole fraction in 2015 was 328.2 ± 0.1 ppb, an increase of 1.1 ppb from the 2014 mean (Fig. 2.40c). The average N_2O growth rate since 2010 is 0.98 ± 0.02 ppb yr^{-1}, higher than the 0.75 ± 0.02 ppb yr^{-1} average growth over the previous decade.

Halogenated gases, such as chlorofluorocarbons (CFCs), hydrochlorofluorocarbons (HCFCs), hydrofluorocarbons (HFCs), and CCl_4 also contribute to radiative forcing. Atmospheric mole fractions of some CFCs, such as CFC-12 and CFC-11, have been decreasing for a decade or more in response to production and consumption restrictions imposed by the Montreal Protocol and its Amendments (Fig. 2.40d; Table 2.7). However, as a result of the CFC phase-out, the atmospheric burdens of CFC replacement gases—HCFCs and HFCs—have increased (Fig. 2.41; Table 2.7; Carpenter et al. 2014; Montzka et al. 2014). Interestingly, of the most abundant ozone-depleting substances that were controlled initially by the Montreal Protocol, the surface mole fraction of only one chemical, halon-1301, is not yet decreasing (Table 2.7).

Trends in the combined direct radiative forcing by five major LLGHGs (CO_2, CH_4, N_2O, CFC-11, and CFC-12) and 15 minor gases are summarized by the NOAA Annual Greenhouse Gas Index (AGGI; Hofmann et al. 2006; www.esrl.noaa.gov/gmd/aggi/). This index represents their annual cumulative radiative forcing relative to the Kyoto Protocol baseline year of 1990. The AGGI does not include indirect radiative forcings (e.g., influences on ozone and water vapor). In 2015, CO_2 contributed 1.94 W m^{-2} direct radiative forcing, 65% of the combined forcing of 2.98 W m^{-2} by the 5 major LLGHGs and 15 minor gases (Fig. 2.42). The combined forcing in 2015 represents a 38% increase (2015 AGGI = 1.38) since 1990, and a 1.4% increase over 2014 (AGGI = 1.36).

TABLE 2.7. Summary table of long-lived greenhouse gases for 2015 (CO_2 mixing ratios are in ppm, N_2O and CH_4 in ppb, and all others in ppt).

Industrial Designation or Common Name	Chemical Formula	AGGI	ODGI	Radiative Efficiency (W m^{-2} ppb^{-1})[a]	Mean Surface Mole Fraction, 2015 (change from prior year)[b]	Lifetime (years)
Carbon Dioxide	CO_2	Y	N	1.37×10^{-5}	399.4 (2.3) [c]	
Methane	CH_4	Y	N	3.63×10^{-4}	1834.0 (11.5) [c]	9.1
Nitrous Oxide	N_2O	Y	N	3.00×10^{-3}	328.2 (1.1) [c,d]	123
Chlorofluorocarbons						
CFC-11	CCl_3F	Y	Y	0.26	232.1 (–1.4) [c,d]	52
CFC-12	CCl_2F_2	Y	Y	0.32	516.1 (–3.4) [c,d]	102
CFC-113	CCl_2FCClF_2	Y	Y	0.30	71.9 (–0.5) [c,d]	93
Hydrochlorofluorocarbons						
HCFC-22	$CHClF_2$	Y	Y	0.21	233.0 (4.1) [c]	11.9
HCFC-141b	CH_3CCl_2F	Y	Y	0.16	24.3 (0.5) [c]	9.4
HCFC-142b	CH_3CClF_2	Y	Y	0.19	21.8 (–0.1) [c]	18
Hydrofluorocarbons						
HFC-134a	CH_2FCF_3	Y	N	0.16	83.5 (5.9) [c]	14
HFC-152a	CH_3CHF_2	Y	N	0.10	6.6 (0.2) [c]	1.6
HFC-143a	CH_3CF_3	Y	N	0.16	16.1 (1.4) [c]	51
HFC-125	CHF_2CF_3	Y	N	0.23	17.0 (1.9) [c]	31
HFC-32	CH_2F_2	N	N	0.11	9.9 (1.6) [c]	5.4
HFC-23	CHF_3	Y	N	0.18	28.1 (1.0) [c]	228
HFC-365mfc	$CH_3CF_2CH_2CF_3$	N	N	0.22	0.8 (0.08) [c]	8.7
HFC-227ea	CF_3CHFCF_3	N	N	0.26	1.1 (0.09) [c]	36
Chlorocarbons						
Methyl Chloroform	CH_3CCl_3	Y	Y	0.07	3.1 (–0.6) [c]	5.0
Carbon Tetrachloride	CCl_4	Y	Y	0.17	82.5 (–1.3) [c,d]	26
Methyl Chloride	CH_3Cl	N	Y	0.01	550 (6) [c]	0.9
Bromocarbons						
Methyl Bromide	CH_3Br	N	Y	0.004	6.6 (–0.04) [c]	0.8
Halon 1211	$CBrClF_2$	Y	Y	0.29	3.61 (–0.08) [c]	16
Halon 1301	$CBrF_3$	Y	Y	0.30	3.27 (0.01) [c]	72
Halon 2402	$CBrF_2CBrF_2$	Y	Y	0.31	0.43 (–0.01) [c]	28
Fully fluorinated species						
Sulfur Hexafluoride	SF_6	Y	N	0.57	8.60 (0.33) [c]	>600
PFC-14	CF_4	N	N	0.09	81.9 (0.7) [c]	~50000
PFC-116	C_2F_6	N	N	0.25	4.49 (0.08) [c]	~10000

[a] Radiative efficiencies were taken from IPCC AR5 (Myhre et al. 2013). Steady-state lifetimes were taken from Myhre et al. (2013) (CH_4), Ravishankara et al. (2009) (SF_6), Ko et al. (2013), and Carpenter et al. (2014). For CO_2, numerous removal processes complicate the derivation of a global lifetime.

[b] Mole fractions are global, annual surface means for the indicated calendar year determined from the NOAA global cooperative air sampling network (Hofmann et al. 2006), except for PFC-14, PFC-116, and HFC-23, which were measured by AGAGE (Mühle et al. 2010; Miller et al. 2010). Changes indicated in brackets are the differences between the 2015 and 2014 global mean mole fractions.

[c] Preliminary estimate.

[d] Global means derived from multiple NOAA measurement programs ("Combined Dataset").

2) OZONE-DEPLETING GASES—B. D. Hall, S. A. Montzka, G. Dutton, and J. W. Elkins

In addition to direct radiative forcing, chlorine- and bromine-containing gases contribute indirectly to radiative forcing through their destruction of stratospheric ozone. The emissions and atmospheric burdens of many of the most potent ozone-depleting gases have been decreasing in response to production and consumption restrictions imposed by the Montreal Protocol and its Amendments (Figs. 2.40d, 2.41). For example, the abundance of CH_3CCl_3 at Earth's surface has declined 98% from its peak in 1992 (Fig. 2.41). CFC-11 and CFC-12, which have much longer atmospheric lifetimes (Table 2.7), have declined by 7.7% and 2.3%, respectively, from their peak mole fractions in 1994 and 2002.

Equivalent effective stratospheric chlorine (EESC) is a measure of the ozone-depleting potential of the halogen loading in the stratosphere at a given time and place. As EESC declines, stratospheric ozone is expected to show signs of recovery. Some recovery is indeed evident in the upper stratosphere, and is attributable, in part, to the decrease in EESC (Pawson et al. 2014; see section 2g4). EESC is calculated from surface measurements of halogenated, ozone-depleting gases and weighting factors that include surface-to-stratosphere transport times, mixing during transit, photolytic reactivity, and ozone-destruction efficiency (Daniel et al. 1995; Schauffler et al. 2003; Newman et al. 2007). Progress towards reducing the stratospheric halogen load is evaluated by the NOAA Ozone-Depleting Gas Index (ODGI; Hofmann and Montzka 2009). The ODGI relates EESC in a given year to the EESC maximum (ODGI = 100) and 1980 value (ODGI = 0), a benchmark often used to assess progress towards reducing stratospheric halogen to pre-ozone hole levels (Fig. 2.43).

The EESC and ODGI are calculated for two representative stratospheric regions—Antarctica and the midlatitudes—that differ in total available reactive halogen (Fig. 2.43a). At the beginning of 2015, EESC values were ~3820 ppt and ~1620 ppt over Antarctica and the midlatitudes, respectively. EESC is larger in the Antarctic stratosphere than in the midlatitudes because more ozone-reactive halogen is released during transit to the Antarctic. Corresponding ODGI values at the beginning of 2015 were 82.9 and 59.5, compared to 84.3 and 61.5 at the beginning of 2014. These represent ~17% and ~40% reductions from the peak values in EESC over Antarctica and the midlatitudes, respectively, towards the 1980 benchmarks (Fig. 2.43b).

3) AEROSOLS—S. Rémy, A. Benedetti, and O. Boucher

Aerosol particles play an important role in the atmosphere through various mechanisms. They influence the radiation budget, directly by scattering and absorbing short- and long-wave radiation, and indirectly by affecting the concentrations, sizes, and chemical composition of cloud condensation nuclei (CCN) that impact the life cycle, optical properties, and precipitation activity of clouds. More information about the radiative forcing by aerosols is provided by Boucher et al. (2013). Aerosols also impact air quality and may cause serious public health issues,

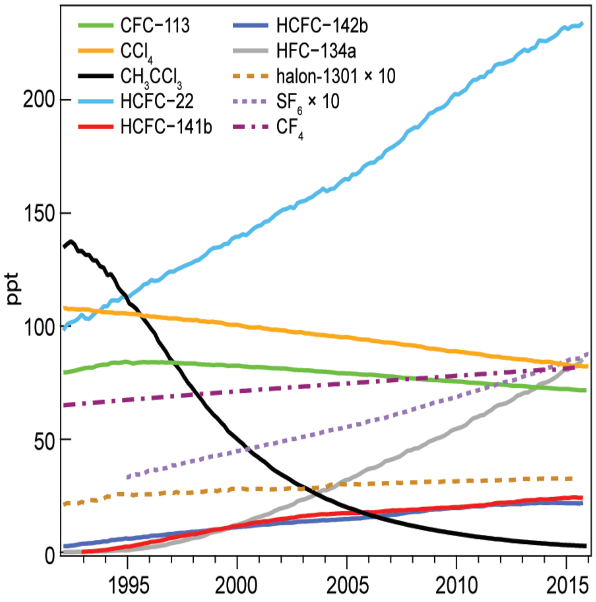

FIG. 2.41. Global mean surface mole fractions at Earth's surface (ppt, dry air) for several halogenated long-lived greenhouse gases. See Table 2.7 for the 2015 global mean mole fractions of these gases.

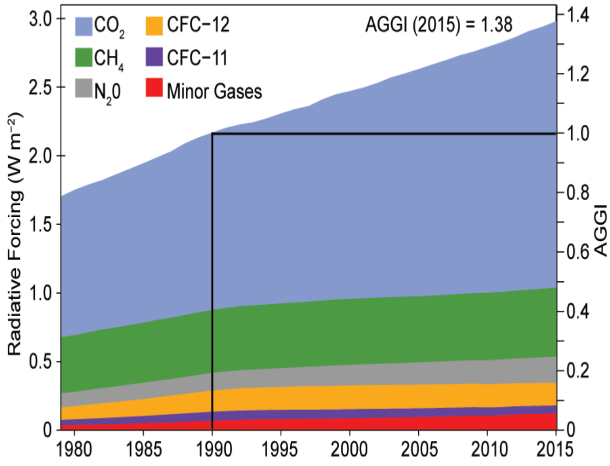

FIG. 2.42. Direct radiative forcing (W m^{-2}) due to 5 major LLGHG and 15 minor gases (left axis) and the Annual Greenhouse Gas Index (right axis).

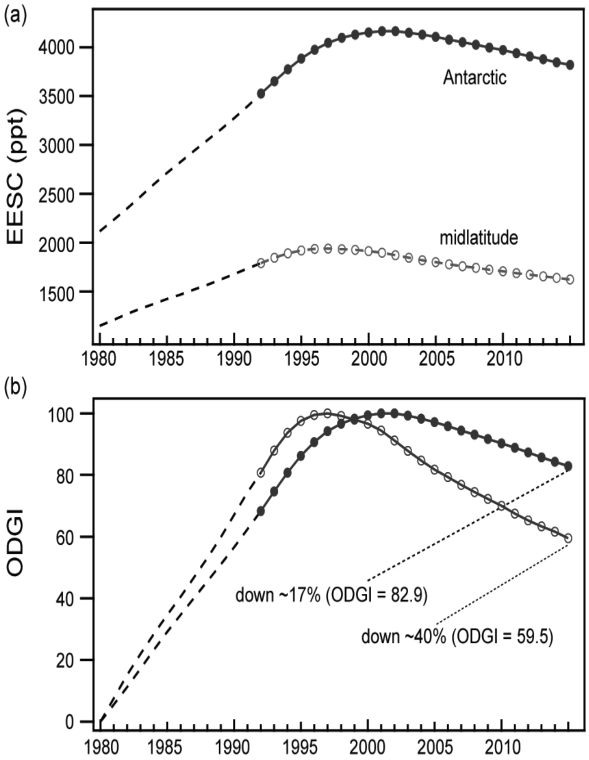

Fig. 2.43. (a) Equivalent Effective Stratospheric Chlorine (EESC) and (b) the NOAA Ozone-Depleting Gas Index (ODGI). The ODGI represents the relative mole fractions of reactive halogen in the midlatitude and Antarctic stratosphere scaled such that ODGI=100 at maximum EESC and zero in 1980. Both EESC and ODGI are derived from NOAA surface measurements of ozone-depleting gases (symbols) or, for earlier years, WMO scenarios (dashed lines, Harris and Wuebbles 2014). The EESC and ODGI values from 1992 forward are for Jan of each year.

as documented by the world media during strong particulate pollution outbreaks in 2015 in parts of western Europe (March), Indonesia and adjacent countries (September–October), and northern China (November).

For the first time in this section, a new interim reanalysis of global aerosols is utilized that spans 2003–15. This was developed within the framework of the Copernicus Atmosphere Monitoring Service (CAMS; J. Flemming, *personal communication*, Feb 2016). Collection 5 retrievals of aerosol optical depth (AOD) at 550 nm from the satellite-based Moderate Resolution Imaging Spectroradiometer (MODIS; Remer et al. 2005) were used as observational constraints. All relevant physical aerosol processes, such as emissions, wet/dry deposition, and sedimentation, are included and fully coupled with the meteorology. The aerosol types treated are naturally produced sea salt and desert dust, as well as black carbon, organic matter, and sulfate aerosols produced by anthropogenic and natural sources. Biomass burning aerosol emissions are the sum of the black carbon and organic matter emitted by open fires and biofuel combustion. Open fire emissions for this new reanalysis were provided by the Global Fire Assimilation System (GFAS) inventory (Kaiser et al. 2012) that estimates emissions from MODIS observations of fire radiative power. Preliminary verification of total AOD using independent observations from the ground-based Aerosol Robotic Network (AERONET) shows that the reanalysis has a global average bias of −2.5% but is consistent over time (J. Flemming, *personal communication*, Feb 2016).

The 2015 annual average anomalies of AOD due to total aerosols, dust, and biomass burning (Plates 2.1v,w,x, respectively) depict strong regional anomalies from biomass-burning events in Alaska, Siberia, Canada, and Indonesia. Overall, the 2015 anomalies of biomass burning aerosols (Plate 2.1x) are consistent with those of tropospheric ozone (section 2g6), carbon monoxide (section 2g7), and fires (section 2h3). Besides the large events already mentioned, the anomaly map of biomass burning aerosols reveals that the 2015 seasonal burning in Africa was more severe than usual south of the equator and less severe north of it. Biomass burning in the Amazon basin in 2015 was similar to the 2003–14 average, interrupting the decreasing trend observed for several previous years. There is a positive anomaly of dust extending west from western Sahara across the tropical Atlantic to Central America (Plate 2.1w), pointing to more active transatlantic dust transport in 2015 than in previous years. On the other hand, dust episodes were less important in 2015 over the northern Sahara and the Mediterranean Sea, and less dust was transported from the Taklamakan and Gobi Deserts into China. Sea salt aerosol anomalies (not shown) were strongly negative in the equatorial Pacific Ocean and west of Indonesia, probably due to disturbances in the trade winds by the strong El Niño conditions during the second half of the year. Positive anomalies of sea salt in the North Atlantic Ocean were caused by a string of active storms there in November–December.

Global maps of the total 550-nm AOD average for 2003–14 and statistically significant (95% confidence) linear trends from 2003 through 2015 are shown in Fig. 2.44. The highly polluted areas of eastern Asia and India are prominent features in the map of long-term average total AOD (Fig. 2.44a), as are the dust-producing regions of the Sahara, the Arabian Peninsula, the Middle East, and the Taklamakan and Gobi Deserts. Large AOD values over the Amazon

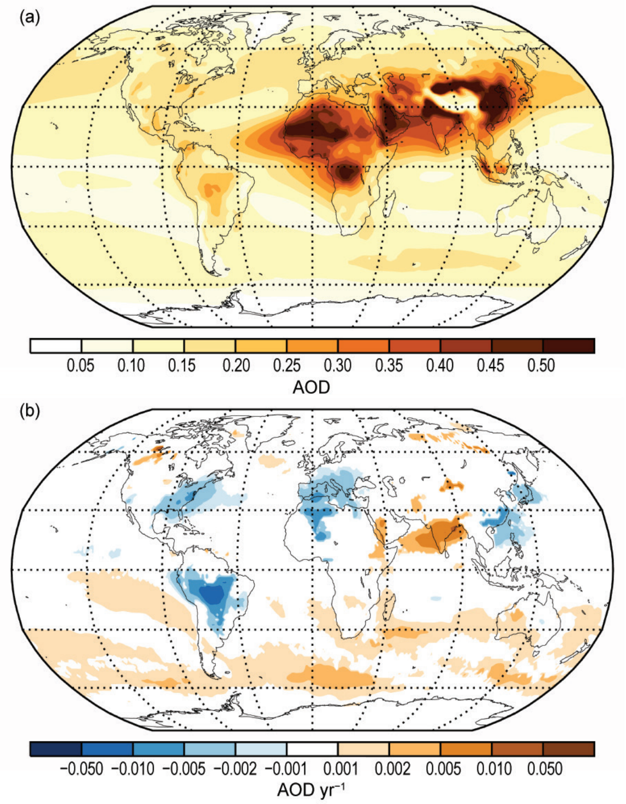

Fig. 2.44. (a) Total 550-nm AOD averages for 2003–14. (b) Linear trends from 2003 through 2015 of total AOD (AOD unit per year). Only trends that are statistically significant at the 95% level of confidence are shown.

basin, equatorial Africa, and Indonesia are caused by seasonal biomass burning. The linear trends highlight long-term decreases in anthropogenic aerosols over the eastern United States, Europe, and parts of southern China, while increases occurred over most of the Indian subcontinent. The area of decreasing trends in the southern Amazon basin is associated with reduced deforestation there (Chen et al. 2013). The decreasing trends over the northern Sahara and western Mediterranean indicate lower frequencies or intensities of dust episodes in these regions. Though many positive trends over the Southern Hemisphere oceans are not statistically significant, those that are could be an artefact of the MODIS Collection 5 observations used in the reanalysis. Time series of globally-averaged total AOD during 2003–15 (Fig. 2.45) show strong seasonality, typically with yearly maxima in March–April and August–September driven mainly by dust episodes and biomass burning in Africa and South America.

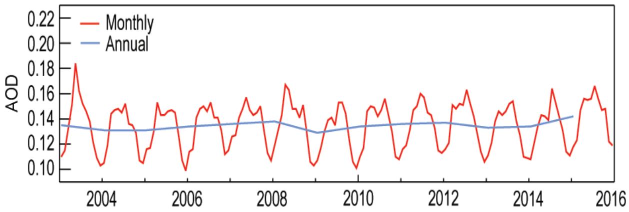

Fig. 2.45. Global averages of total AOD at 550 nm averaged over monthly (red) and annual (blue) periods for 2003–15.

Aerosol monitoring relies on a multistream global observing system. Routine aerosol observations are mainly provided by two federated, ground-based networks: AERONET and Global Atmospheric Watch (GAW), which in 2015 operated 311 and >220 stations, respectively. MODIS satellite instruments on *Aqua* and *Terra* have continued to provide retrievals of AOD during 2015, while the Visible Infrared Imaging Radiometer Suite (VIIRS) on *Suomi NPP* has provided aerosol data products since 2013. Geostationary satellites are also increasingly being used to measure aerosols. For instance, AOD derived from Meteosat Second Generation (MSG) observations over Europe and Africa is available from 2014 (Carrer et al. 2014). AOD observations are now routinely incorporated into atmospheric models using data assimilation algorithms (e.g., Zhang et al. 2008; Benedetti et al. 2009; Inness et al. 2015b) to combine them with short-term forecasts. Such observationally constrained models can be used to build a reanalysis of atmospheric composition. Reanalyses can, to a large extent, be considered a good proxy for observed conditions. They provide whole atmosphere coverage and the ability to provide variables not routinely observed, such as the AOD of different aerosol types (e.g., dust, sea salt, and carbonaceous). However, their limitations should be kept in mind. To accommodate limited computing resources, models usually simplify aerosol processes and may not take into account all of the aerosol species and/or their interaction. This means that the atmospheric composition reanalysis aerosol products usually do not capture all of the observed variability and complexity of aerosol fields. Assessing the relative weight of observations and model values in the data assimilation scheme of such systems is not trivial; this can also lead to uncertainties (Inness et al. 2013).

4) Stratospheric ozone—M. Weber, W. Steinbrecht, C. Roth, M. Coldewey-Egbers, D. Degenstein, Y. E. Fioletov, S. M. Frith, L. Froidevaux, J. de Laat, C. S. Long, D. Loyola, and J. D. Wild

Total ozone columns in 2015 were close to the 1998–2008 average for most of the globe, except in extended regions at high latitudes in both hemispheres, where ozone columns were largely below average (Plate 2.1q). The strong negative anomalies at high Southern Hemisphere latitudes reflect the large Antarctic ozone hole observed in September–December, whose size reached maximum values that were near the all-time record high (see section 6h).

In Fig. 2.46 the total ozone annual means from different data sources are shown for 1970–2015 in various zonal bands: near-global (60°S–60°N), midlatitudes in both hemispheres (35°–60°), and the inner tropics (20°S–20°N). Also shown are the polar time series in March (Northern Hemisphere, 60°–90°N) and October (Southern Hemisphere, 60°–90°S), the months when polar ozone losses are largest in each hemisphere. Poleward of 60°S, a record low October mean was observed (Fig. 2.46e). Weaker-than-usual dynamical wave activity in the Southern Hemisphere winter diminished transport from the tropics, reducing ozone at Southern Hemisphere midlatitudes and in the collar region of the polar vortex, and permitting a very stable and cold polar vortex. The high vortex stability and low temperatures resulted in larger-than-usual polar ozone losses and a near-record ozone hole in terms of size and persistence. Ozone annual mean columns at mid- to polar latitudes (35°–90°) in each hemisphere are largely determined by winter/spring ozone levels. These vary considerably with changes in stratospheric meteorological conditions (e.g., Steinbrecht et al. 2011; Weber et al. 2011; Kuttippurath et al. 2015). The year-to-year variability seen in all ozone time series also reflects quasi-biennial oscillation (QBO)-related variations extending from the tropics into the extratropics (Randel and Wu 1996; Strahan et al. 2015).

It is clear that the Montreal Protocol and its Amendments have been successful in stopping the multidecadal decline in stratospheric ozone by the late 1990s (WMO 2011). However, at most latitudes, it has not yet been possible to determine a statistically significant increase in total column ozone or lower stratosphere ozone because the expected small increases are masked by large interannual variability (e.g., Chehade et al. 2014; Coldewey-Egbers et al. 2014; Frith et al. 2014; Kuttippurath et al. 2015; Nair

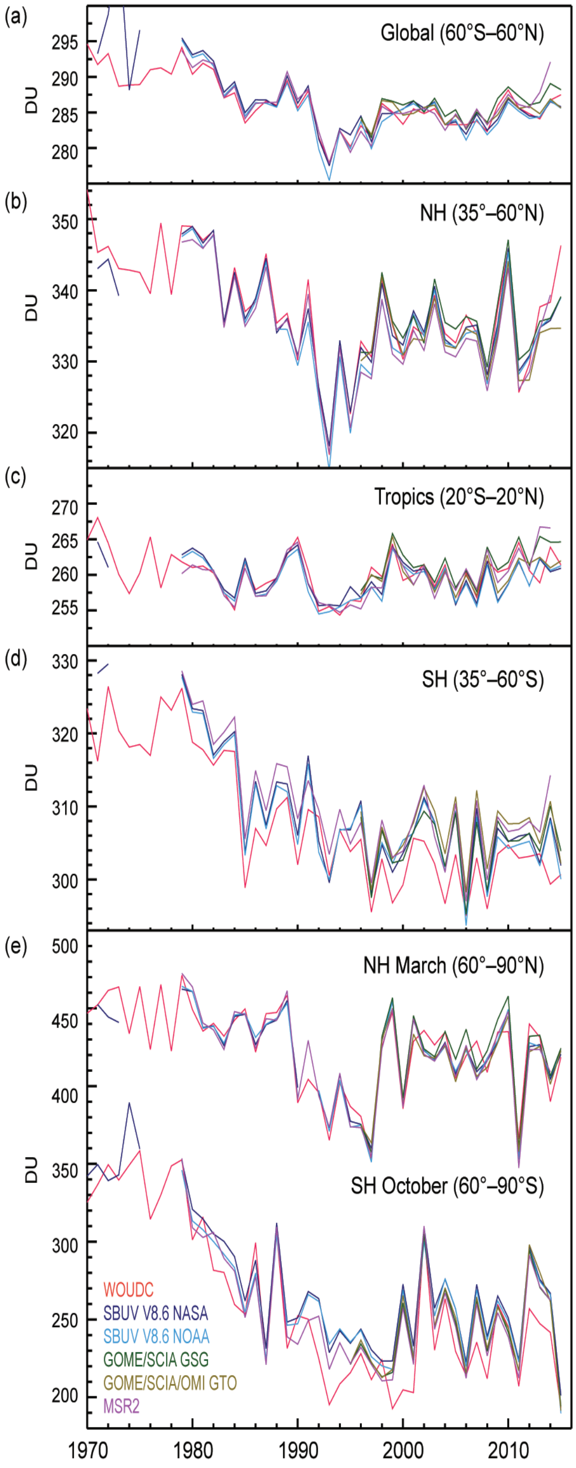

Fig. 2.46. Time series of annual mean total ozone in (a–d) four zonal bands and (e) polar (60°–90°) total ozone in Mar (Northern Hemisphere) and Oct (Southern Hemisphere). Data are from WOUDC ground-based measurements combining Brewer, Dobson, SAOZ, and filter spectrometer data (red: Fioletov et al. 2002, 2008); the BUV/SBUV/SBUV2 V8.6 merged products from NASA (MOD V8.6, dark blue, Chiou et al. 2014; Frith et al. 2014) and NOAA (light blue, Wild et al. 2012); the GOME/SCIAMACHY/GOME-2 products GSG from University of Bremen (dark green, Weber et al. 2011) and GTO from ESA/DLR (light green, Coldewey-Egbers et al. 2015); and the MSR V2 assimilated dataset extended with GOME-2 data (van der A et al. 2015). WOUDC values for 2015 are preliminary because not all ground station data were available in early 2016.

et al. 2015; de Laat et al. 2015). The 2015 total ozone columns in Fig. 2.46 are consistent with this overall picture and lie within the expected usual variations.

In the tropics, no discernible long-term trends in total column ozone have been observed for the entire 1970–2015 period (see Fig. 2.46). Ozone trends in the tropical lower stratosphere are mainly determined by tropical upwelling (related to changes in sea surface temperature). In a changing climate it is expected that tropical upwelling will increase and thus ozone will continue to decline (Zubov et al. 2013; WMO 2014). However, there is some evidence of a hiatus in tropical upwelling trends and corresponding lower stratospheric ozone trends during the last decade (Aschmann et al. 2014). Because tropospheric ozone contributes to the total ozone columns, trends in total ozone, despite major contributions from the lower stratosphere, may differ from trends in lower stratospheric ozone (Shepherd et al. 2014).

The most recent ozone assessment (WMO 2014) and studies (Nair et al. 2015; Harris et al. 2015) indicate that the clearest signs of significant ozone increases should occur in the upper stratosphere (2%–4% decade^{-1} at ~2 hPa or 40 km; see Fig. 2.47). However, there still are uncertainties associated with the various available data records and with the proper interpretation of statistical approaches used to derive and attribute trends (e.g., Nair et al. 2015; Kuttippurath et al. 2015; Harris et al. 2015). This is reflected in the updated Stratospheric Aerosol and Gas Experiment (SAGE)–Optical Spectrograph and Infrared Imager System (OSIRIS) record, which now better accounts for tangent altitude drifts, and in the updated Solar Backscatter Ultraviolet (SBUV) data from NOAA with improved inter-satellite adjustments. Overall, the 2015 annual means in Fig. 2.47 support the claim of recent increases in upper stratospheric, extra-polar ozone. These suggest the Montreal Protocol has successfully turned the previous downward trend in ozone into an ozone increase, at least in the upper stratosphere.

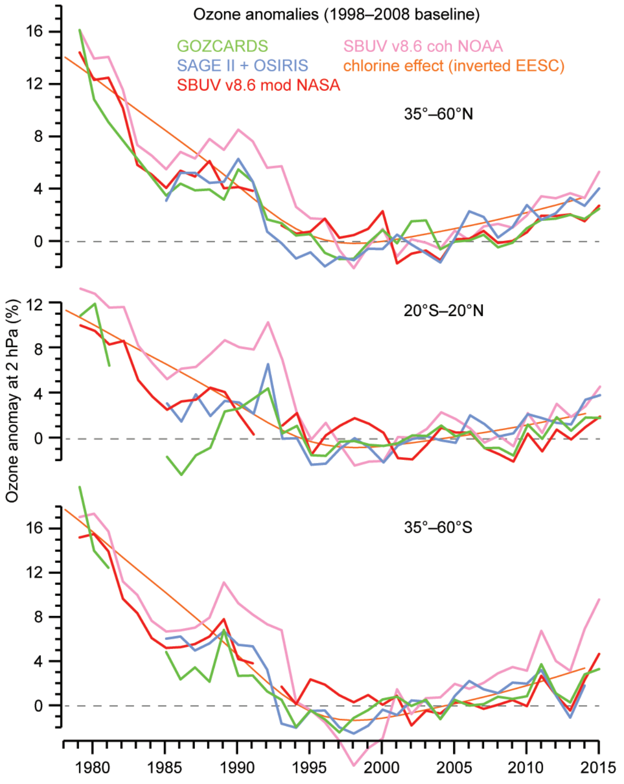

Fig. 2.47. Annual mean ozone anomalies at 2 hPa (~40 km, upper stratosphere) in three zonal bands. Data are from the merged SAGE II/OSIRIS (Bourassa et al. 2014) and GOZCARDS (Froidevaux et al. 2015) records and from the BUV/SBUV/SBUV2 v8.6 merged products from NASA (McPeters et al. 2013; Frith et al. 2014) and NOAA (Wild et al. 2012) (base period: 1998–2008). The orange curves represent EESC (effective equivalent stratospheric chlorine), scaled to reflect the expected ozone variation due to stratospheric halogens. Data points for 2015 are preliminary, because SAGE-OSIRIS data were not yet available after July 2015, and adjusted SBUV2 v8.0 data are used after July 2015 instead of v8.6 data, which are not available in early 2016.

5) Stratospheric water vapor—S. M. Davis, K. H. Rosenlof, D. F. Hurst, and H. B. Selkirk

Variations in stratospheric water vapor (SWV) over interannual-to-decadal timescales have the potential to affect stratospheric ozone (Dvortsov and Solomon 2001) and surface climate (Solomon et al. 2010). Throughout the first 10 months of 2015, water vapor mixing ratios in the tropical lowermost stratosphere were within 10% (0.4 ppm, µmol mol^{-1}) of the previous decade's average. Then, starting in November and continuing through December, tropical lowermost SWV increased to near-record levels, especially over the tropical western Pacific and Indian Ocean regions. The deep tropical-averaged (15°S–15°N) SWV anomaly at 82 hPa, based on data from the *Aura* Microwave Limb Sounder (MLS), was +0.7 ppm (+17%) in November and +0.9 ppm (+24%) in December. These values are in stark contrast to the weak negative (dry) tropical average anomalies of about −0.2 ppm (−6%) in November–December 2014 (Figs. 2.48, 2.49). Since the MLS record began in August 2004, the November–December 2015 anomalies at 82 hPa are surpassed only by +0.9 ppm (+25%) deep tropical anomalies in February–March 2011. The +0.7 ppm (+19%) average deep tropical anomaly at 100 hPa in November–December 2015 is the high-

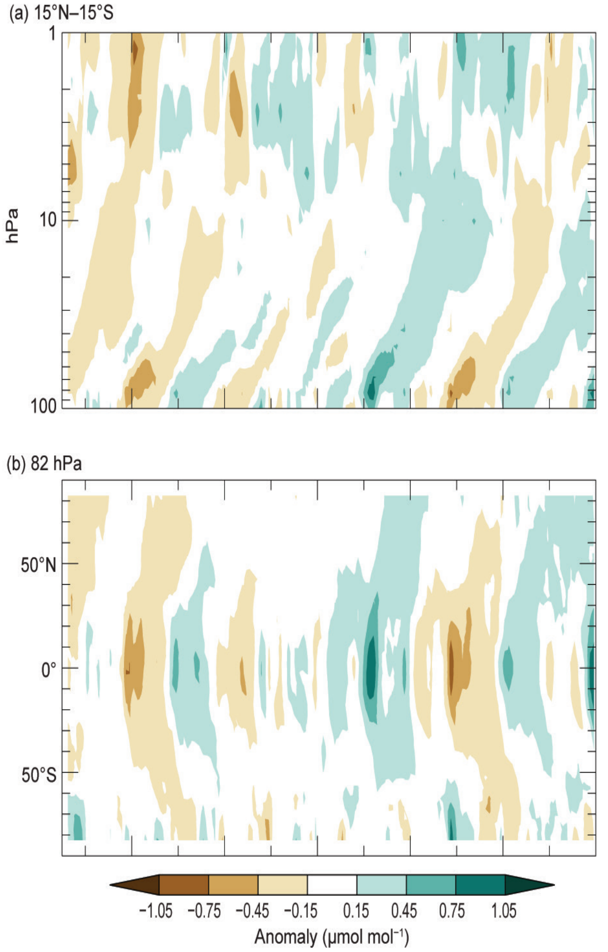

Fig. 2.48. (a) Vertical profiles of MLS tropical (15°S–15°N) water vapor anomalies (μmol mol⁻¹) and (b) latitudinal distributions of MLS water vapor anomalies (μmol mol⁻¹) at 82 hPa. Anomalies are differences from the 2004–15 mean water vapor mixing ratios for each month.

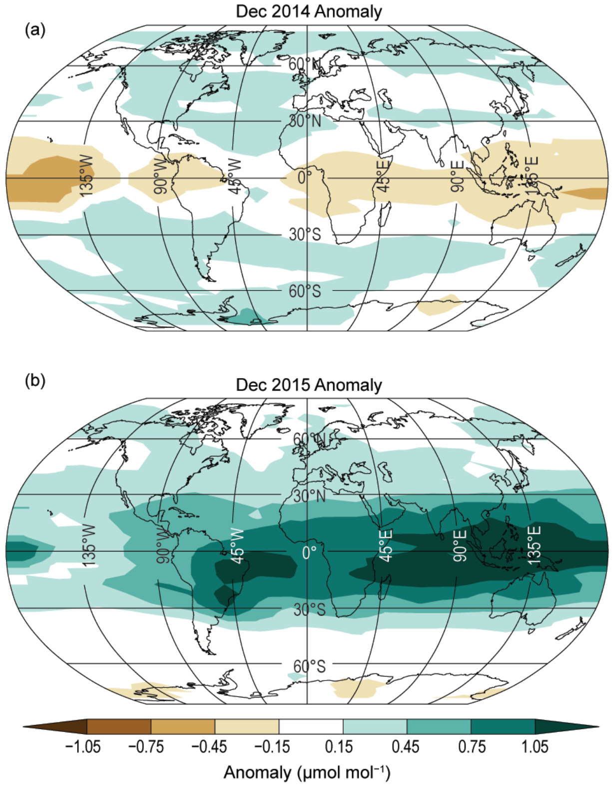

Fig. 2.49. Global stratospheric water vapor anomalies (μmol mol⁻¹) centered on 82 hPa in (a) Dec 2014 and (b) Dec 2015 from the *Aura* Microwave Limb Sounder.

est ever observed by MLS at that pressure level. The change in tropical lower SWV from December 2014 to December 2015 was +1.1 ppm, ~50% of the typical seasonal mixing ratio amplitude at 82 hPa in the tropics. Strong water vapor increases in the tropical lower stratosphere at the end of 2015 were also observed at Hilo, Hawaii (20°N), and San José, Costa Rica (10°N), by balloonborne frost point hygrometers (Figs. 2.50b,c).

The seasonal variability of water vapor in the tropical lower stratosphere is predominantly controlled by the annual cycle of cold-point temperatures (CPTs) in the tropical tropopause layer (TTL). These minimum temperatures determine the amounts of water vapor that remain as moist tropospheric air masses are freeze-dried during their slow ascent into the stratosphere. Seasonal-to-interannual variations in tropical lower SWV are highly correlated with CPT variations in the TTL. The dramatic increase in tropical lower SWV at the end of 2015 is consistent with the observed ~1°C increase in tropical CPTs over the same period (Fig. 2.50c).

Interannual variations in CPTs are potentially related to the changing phases of the El Niño–Southern Oscillation (ENSO) and the stratospheric quasi-biennial oscillation (QBO). In October, the QBO phase transitioned from easterly (cold) to westerly (warm) and persisted in the westerly phase through the end of 2015 (see sections 2b3, 2e3). The evolution towards a warmer TTL and wetter tropical lower stratosphere at the end of 2015 is consistent with this reversal of the QBO phase. Regionally, the enhancement of SWV in the tropical western Pacific and Indian Ocean regions is consistent with the adiabatic response of the TTL to reduced convection in this region as a result of the El Niño conditions present during 2015. Other factors such as variations in the strength of the Brewer–Dobson circulation can also impact SWV anomalies on an interannual timescale. However, given the potential interrelationships between ENSO, QBO, and the Brewer–Dobson circulation, a rigorous attribution of the positive SWV anomalies present at the end of 2015 is not possible.

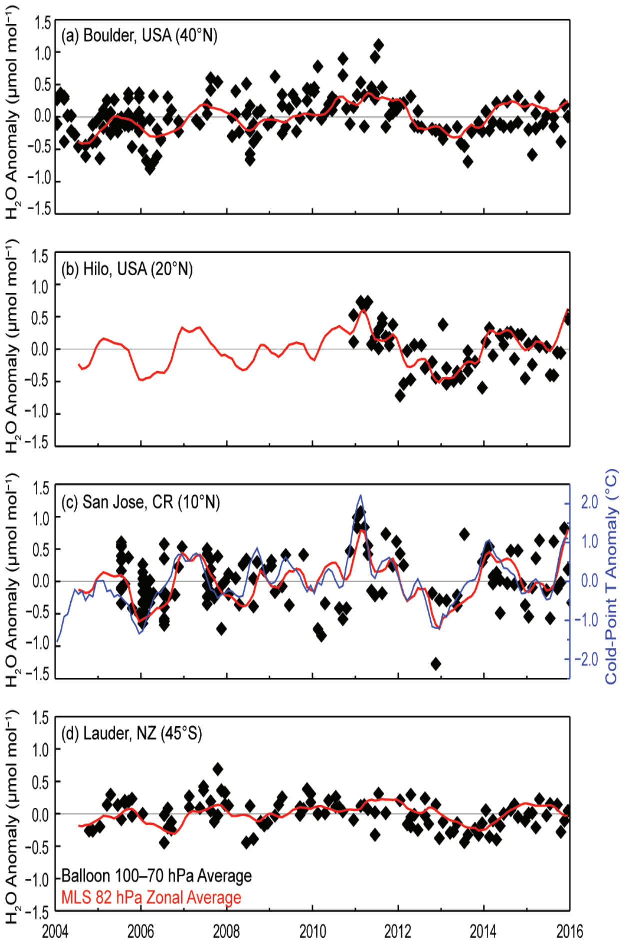

Fig. 2.50. Lower stratospheric water vapor anomalies (μmol mol^{-1}) at 82 hPa over four balloonborne frost point (FP) hygrometer stations. (a)–(d) show the anomalies of individual FP soundings (black) and of monthly zonal averages of MLS retrievals in the 5° latitude band containing the FP station (red). High-resolution FP vertical profile data were averaged between 70 and 100 hPa to emulate the MLS averaging kernel for 82 hPa. Each MLS monthly zonal mean was determined from 2000 to 3000 profiles. Tropical cold-point temperature anomalies based on the MERRA reanalysis [(c), blue curve] are generally well correlated with the tropical lower SWV anomalies.

Anomalies in tropical lower SWV propagate from the tropics to the midlatitudes of both hemispheres, as is visually demonstrated by the many "C"-shaped contours in Fig. 2.48b. The late 2015 wet anomaly in tropical lower SWV (Figs. 2.48b, 2.50c) was just starting to reach the midlatitudes of each hemisphere at the end of 2015.

During 2015, SWV anomalies over Lauder, New Zealand, were close to zero or slightly positive (Fig. 2.50d). These are consistent with the poleward transport of weak dry tropical SWV anomalies present at the end of 2014 and early 2015 (Fig. 2.49a), and the 2014 Antarctic vortex being anomalously weak, warm, and less dehydrated (Davis et al. 2015; see sections 2b3 and 6h). In general, Southern Hemisphere midlatitude SWV can vary interannually with the degree of seasonal dehydration within the Antarctic vortex and the strength of the poleward transport of dehydrated air masses (Fig. 2.48b). Indeed, the 2015 Antarctic vortex was particularly strong (see section 6h), as evidenced by the appearance of a −0.5 ppm anomaly in the high southern latitudes near the end of 2015 (Fig. 2.48b).

6) Tropospheric ozone—J. R. Ziemke and O. R. Cooper

Two of the most important reasons to monitor tropospheric ozone are that it is a surface pollutant with harmful biological effects and is a greenhouse gas that affects long-term climate change. Tropospheric ozone is also the primary source of the hydroxyl radical (OH), the main oxidizing agent for pollutants in the troposphere. Sources of tropospheric ozone include transport from the stratosphere, photochemical production from lightning NO_x, and photochemical production from precursor gases emitted by the combustion of fossil fuels, biofuels, and biomass (e.g., Sauvage et al. 2007; Martin et al. 2007; Leung et al. 2007; Murray et al. 2013; Hess and Zbinden 2013; Young et al. 2013).

The variability of tropospheric ozone, from urban to hemispheric scales, is driven by a combination of photochemical ozone production and atmospheric transport. Tropospheric ozone production varies because its precursor gases and sunlight are variable. Transport phenomena that drive large-scale variability include ENSO (e.g., Chandra et al. 1998, 2009; Sudo and Takahashi 2001; Doherty et al. 2006; Koumoutsaris et al. 2008; Voulgarakis et al. 2011) and the Madden–Julian oscillation (MJO: Sun et al. 2014). Small- to large-scale tropospheric ozone variability also occurs over shorter periods, including weekly baroclinic timescales (e.g., Ziemke et al. 2015, and references therein), and finer scale airstream transport on the order of hours to days. Changes in tropospheric ozone at hemispheric and global scales include decadal trends (e.g., Hess and Zbinden 2013; Cooper et al. 2014; Lin et al. 2014; Parrish et al. 2014).

Global maps of annual means and anomalies of tropospheric column ozone from the satellite-based Ozone Monitoring Instrument (OMI) and MLS for 2015 are shown in Fig. 2.51 and Plate 2.1u, respectively. As in previous reports, OMI/MLS ozone trends are calculated only for latitudes 60°S–60°N where there is full annual coverage by OMI. In 2015, as for the last decade, annual average tropospheric column ozone

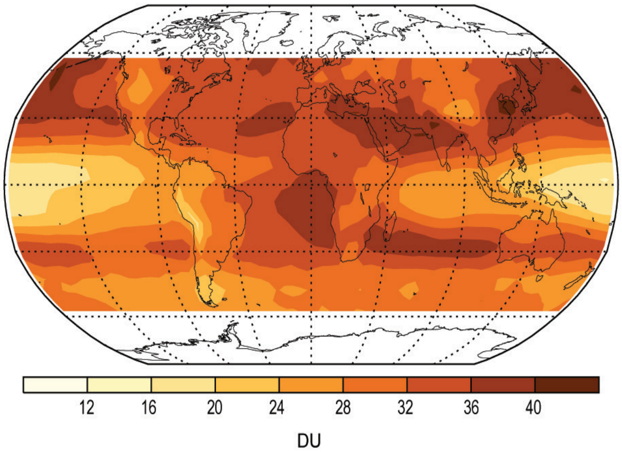

Fig. 2.51. Average OMI/MLS tropospheric ozone column ozone for 2015. Data poleward of ±60° are not shown due to the inability of OMI to measure ozone during polar night.

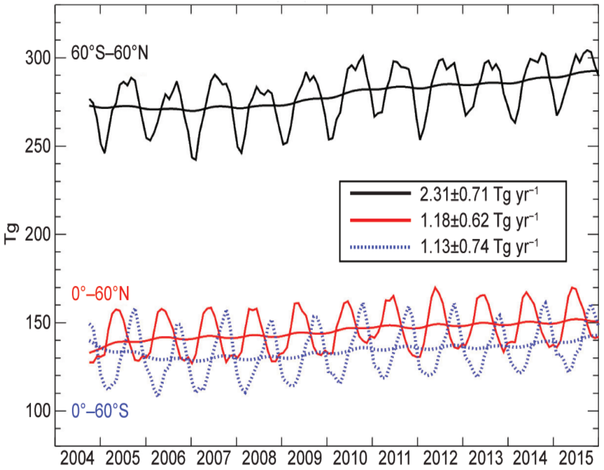

Fig. 2.52. Monthly averages of OMI/MLS tropospheric ozone burdens (Tg) from Oct 2004 through Dec 2015. The top curve (black) shows 60°S–60°N monthly averages with 12-month running means. The bottom two curves show monthly averages and running means for the Northern Hemisphere (red) and Southern Hemisphere (blue). Slopes of linear fits (Tg yr^{-1}) of all three curves are also listed along with their ±2σ statistical uncertainties.

amounts in the Northern Hemisphere exceeded those in the Southern Hemisphere. Some basic features of tropospheric column ozone include strong topographical effects, such as greatly reduced amounts over the Tibetan Plateau and the western U.S. Rocky Mountain region, with much larger amounts east and west of these regions over both land and ocean. The greatest annual mean tropospheric column values were observed over the Mediterranean–South Asian region and from eastern China eastward toward North America. In the tropics, the west-to-east zonal wave-1 pattern (Fishman et al. 1990) is evident, with high values over the Atlantic and low values over the Pacific. An extended band of high ozone was present at 30°S, with the greatest amounts between southern Africa and Australia. Zonally-averaged tropospheric column averages and their 95% confidence intervals for 2015 were 30.7 ± 2.2 DU for 60°S–60°N, 32.1 ± 2.6 DU for 0°–60°N, and 29.4 ± 1.9 DU for 0°–60°S. These column averages convert to tropospheric burdens of 291.2 ± 20.9, 152.1 ± 12.3, and 139.1 ± 9.0 Tg, (Tg = 10^{12} g), respectively. For comparison, the tropospheric column averages for 2005–15 for the three regions were 29.5 ± 2.1, 30.7 ± 2.5, and 28.2 ± 2.2 DU (279.0 ± 19.9, 145.4 ± 11.8, and 133.6 ± 10.4 Tg).

The 2015 average tropospheric ozone burdens for each hemisphere and the globe were greater than those in 2014, and 12-month running averages of each show steady increases since October 2004 (Fig. 2.52). Linear trends (in Tg yr^{-1}) with their ± 2σ statistical uncertainties are also given. The increasing trends in OMI/MLS tropospheric column ozone are statistically significant for both hemispheric means and the near-global mean. Relative to the average burdens for 2005–15 the three trends all depict increases of 0.8% yr^{-1}. The combined OMI/MLS record now exceeds 11 years and the measured increases are becoming more indicative of true long-term trends, building on similar findings from previous reports.

Cooper and Ziemke (2013) reported surface ozone increasing since 1990 over eastern Asia and the western United States, but decreasing over the eastern United States, using measurements by ground- and satellite-based instruments. Cooper and Ziemke (2014) presented a time series of near-global (60°S–60°N) tropospheric burdens determined from satellite measurements that indicated a statistically significant increase over 2005–13 and Cooper and Ziemke (2015) showed that the increase in global tropospheric ozone continued through 2014.

For the past two years, the *State of the Climate* tropospheric ozone summary was based upon only the OMI/MLS satellite measurements (Ziemke et al. 2006) due to insufficient updated analyses of the ground-based measurement network data since 2012. Updates of the surface ozone data and trends have continued to be infrequent during 2015, so once again only the OMI/MLS satellite data are used. One significant change from previous reports is the use of new MLS version 4.2 ozone retrievals. A new activity of the International Global Atmospheric Chemistry (IGAC) project began in earnest in 2015 to produce a Tropospheric Ozone Assessment Report (TOAR). The TOAR is expected to be completed by the end of 2016 and will summarize the global distribution and trends of tropospheric ozone through 2014/15 (depending on the product) using a variety of satellite, surface, ozonesonde, lidar, and aircraft ozone measurements (www.igacproject.org/TOAR).

7) Carbon monoxide—J. Flemming and A. Inness

Carbon monoxide (CO) is not a greenhouse gas, but plays a significant role in determining the abundance of climate forcing gases like methane (CH_4), through hydroxyl radical (OH) chemistry, and tropospheric ozone (O_3), as a chemical precursor (Hartmann et al. 2013). Thus, CO is regarded as an indirect climate forcing agent. Sources of CO include incomplete fossil fuel and biomass combustion and in situ production via the oxidation of CH_4 and other organic trace gases. Combustion and chemical in situ sources typically produce similar amounts of CO each year.

New in 2015 is a CAMS-based retrospective analysis of CO for the period 2003–15 based on total column CO retrievals from the Measurements of Pollution in the Troposphere (MOPITT) instrument (Deeter et al. 2013, Version 5). This dataset is part of the CAMS interim reanalysis of atmospheric composition, an extended and temporally more consistent dataset than the previous Monitoring Atmospheric Composition and Climate (MACC) reanalysis (Inness et al. 2013). The MACC has been used in previous *State of the Climate* assessments of CO and aerosols. MOPITT retrievals between 65°N and 65°S were assimilated into the European Centre for Medium-Range Weather Forecasts (ECMWF) Integrated Forecasting System (IFS) that has been extended to simulate atmospheric chemistry (Flemming et al. 2015). The assimilation technique is documented in Inness et al. (2015b). The anthropogenic emissions for the assimilating model were taken from the MACCity inventory (Granier et al. 2011) that accounts for projected emission trends. Biomass burning emissions were taken from the Global Fire Assimilation System (v1.2, Kaiser et al. 2012). The global three-dimensional CO distribution from the CAMS interim reanalysis is used here to assess the anomalies in CO total columns for 2015.

The global CO burden in 2015 was significantly increased by the intensive El Niño-induced wildfires in Indonesia from mid-August to mid-November (Sidebar 2.2). Annual wildfire emissions from this region contributed 31% (140 Tg) of the global wildfire emissions in 2015, whereas for 2003–14 the contributions ranged from 5% to 20%. The highest total (biomass burning and anthropogenic) monthly CO emissions since 2003 were injected into the atmosphere during the 2015 Indonesian fire period. This El Niño–related increase in Indonesian fires and CO emissions was already reported for 2014 (Flemming and Inness 2015) and high fire activity is anticipated for the March–April fire season in 2016. An analysis by Huijnen et al. (2016) suggests that the 2015 carbon emissions from the Indonesia fires were the second largest since the extreme El Niño year of 1997, although the 2015 emissions were only 25% of those in 1997.

Plate 2.1ac shows the relative 2015 anomalies of the total column CO (TCCO) from the CAMS interim reanalysis with respect to 2003–15. The strong positive TCCO anomalies were located predominately over the Indonesian region and the eastern Indian Ocean, but the fire emissions increased CO over much of the tropics. Tropospheric CO mixing ratios between 50° and 100°E in the tropics in September and October were 50%–100% higher than the CO climatology. Larger-than-usual wildfire activity in North America during 2015 produced >10% anomalies in June–August and led to a positive anomaly in total column CO for the year. The CO anomaly of –10% over the Amazon basin reflects a decadal decrease in fires in that region, but the 2015 anomaly was not as strongly negative as in the two previous years.

The high global CO burden in 2015 occurred against a 12-year backdrop of a decreasing global CO burden. Figure 2.53 shows the time series of monthly mean global CO burdens since 2003. A decreasing linear trend of −0.86 ± 0.23% yr^{-1} is evident, yet the monthly averaged global burdens for October–December 2015 are the highest values in the entire record. Worden et al. (2013) estimate trends of –1% yr^{-1} for both the globe and Northern Hemisphere over the last decade by studying observations from

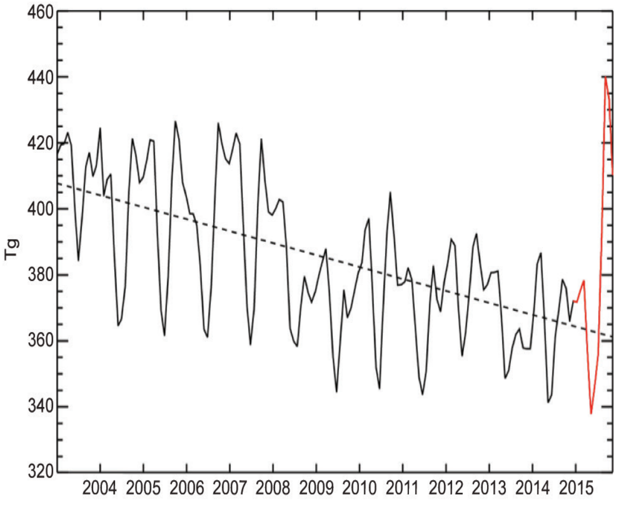

Fig. 2.53. Time series of monthly global CO burdens (Tg) from the CAMS interim reanalysis.

SIDEBAR 2.2: ATMOSPHERIC COMPOSITION CHANGES DUE TO THE EXTREME 2015 INDONESIAN FIRE SEASON TRIGGERED BY EL NIÑO—A. BENEDETTI, F. DI GIUSEPPE, J. FLEMMING, A. INNESS, M. PARRINGTON, S. RÉMY, AND J. R. ZIEMKE

One of the most extreme events of 2015 was the extensive burning of peat throughout large parts of Indonesia. As a common practice in Indonesia, fires are set during the dry season (July–October) to clear land and remove agricultural residues. During intense dry seasons these fires can penetrate into degraded subsurface peat soil with enhanced flammability. They are extremely difficult to extinguish and can burn continuously until the return of the monsoon rains, usually in late October or early November. In 2015, the annual fires were more widespread and intense than those that have typically occurred in Kalimantan since the 1980s and in Sumatra since at least the 1960s (Field et al. 2009). The strength and prevalence of these fires are strongly influenced by large-scale climate patterns like El Niño (Field et al. 2004; van der Werf 2008). Research started after the strong 1997/98 El Niño, which induced a severe fire/haze disaster in Indonesia, has provided a reliable understanding of how much fire and haze may occur for a given drought strength (Usup et al. 2004; Field et al. 2009). Despite this predictive capability, the 2015 fires in Indonesia still escalated to an environmental and public health catastrophe (Thielen et al. 2015; Inness et al. 2015; Field et al. 2015, manuscript submitted to *Proc. Natl. Acad. Sci. USA*).

The 2015 Indonesia fire season began in August, and by September much of Sumatra, Kalimantan, Singapore, and parts of Malaysia and Thailand were covered in thick smoke, affecting the respiratory health of millions of people. Visibility was also reduced to less than 10% of normal over Borneo, and large parts of the region could not be seen from space, as was documented for previous fire events in that region (Marlier et al. 2013; Wang et al. 2004). Preliminary estimates suggest that greenhouse gas emissions from the burning (in CO_2 equivalent) exceeded Japan's 2013 emissions from fossil fuel combustion (Van der Werf 2015). Even after the worst of the 2015 Indonesian fires were no longer burning, the remaining pollution stretched halfway around the globe.

Ongoing research into the socioeconomic drivers of the fires is beginning to identify the responsibilities of the landholders and the need for political action in regulating the agricultural practices in the region (Tacconi 2003). While finding the socioeconomic causes of this event is beyond the scope of this work, we can utilize analytical results from observations and reanalyses of atmospheric composition over Indonesia to provide an assessment of the current monitoring capabilities of observational and modeling systems.

To this end, we use the data assimilation system of the Copernicus Atmosphere Monitoring Service (CAMS) developed at the ECMWF since 2005. The interim CAMS reanalysis is an improved version of the previous MACC reanalysis (Inness et al. 2013) and is updated in quasi near–real time. Observational datasets used, among others, are the NASA MODIS Aerosol Optical Depth Collection 5 product (Remer et al. 2005) and the MOPITT V5 total column carbon monoxide (CO) retrievals. A reanalysis dataset provides a dynamically consistent 3D estimate of the climate state at each time step and can be considered a good proxy for atmospheric conditions, including variables that are not directly observed. Here, 2015 anomalies of CO and carbonaceous aerosols are determined from the 2003–15 CAMS reanalysis, while the ozone anomalies are based on the 2005–14 ozone records from NASA's Ozone Monitoring Instrument (OMI) and Microwave Limb Sounder (MLS) (Ziemke et al. 2006).

Realistic biomass burning emissions estimates, provided by the Global Fire Assimilation System (GFAS; Kaiser et al. 2012; Di Giuseppe et al. 2016, manuscript submitted to *J. Geophys. Res. Atmos.*), are an important input to the CAMS system. In the GFAS, the fire radiative power (FRP) measured by the MODIS sensors on the *Aqua* and *Terra* satellites is converted into emissions of 44 constituents using the regression coefficients of Wooster et al. (2003). The FRP observations accumulated over the period August–October 2015 (Fig. SB2.3) provide an overview of the extent and severity of the 2015 Indonesian fire season.

Fire emissions in Indonesia during August–October were consistently and extraordinarily strong, as clearly shown by the number of days in 2015 when daily emissions of CO and biomass burning aerosols [black carbon (BC),

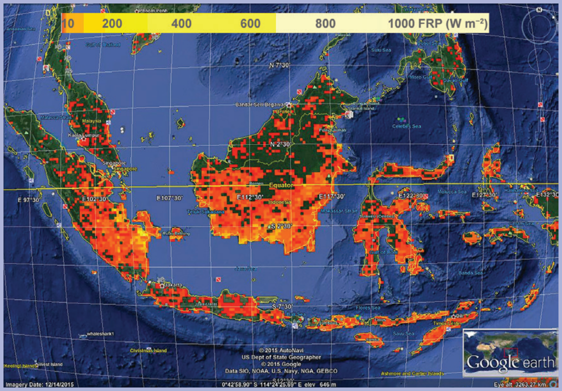

Fig. SB2.3. Fire radiative power (W m$^{□2}$) accumulated over Indonesia during the 2015 fire season (Aug–Oct).

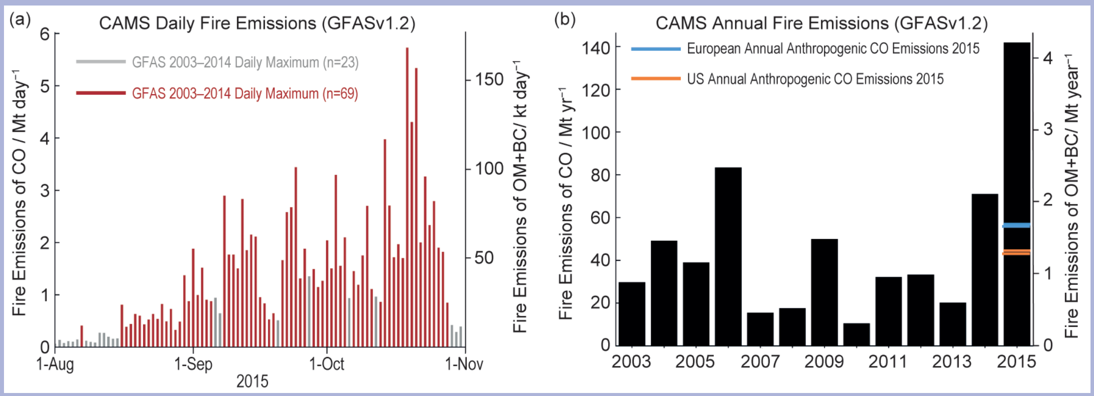

Fig. SB2.4. (a) Daily Indonesian fire emissions in 2015 of CO (Mt day^{-1}) and OM+BC aerosols (kt day^{-1}). Red bars show the days in 2015 with emissions greater than the previous (2003–14) maximum emission estimate for that day. (b) Annual fire emissions of CO and OM+BC aerosols (Mt yr^{-1}) from Indonesia indicating their scale relative to the 2015 total anthropogenic CO emissions from the United States (red line) and Europe (blue line) from the MACCity emissions inventory. GFASv1.2 emissions of CO and OM+BC from biomass burning are directly proportional.

and organic matter (OM)] exceeded the maximum daily emissions during the same days in 2003–14 (Fig. SB2.4a). Total annual fire emissions over Indonesia (10°S–5°N, 60°–180°E) computed by the GFASv1.2 system for CO and BC+OM are substantially greater for El Niño years 2006, 2009, and 2015 (Fig. SB2.4b). For perspective, CO emissions from the Indonesian fires for 2015 were approximately three times the 2015 total anthropogenic emissions from the continental United States (25°–50°N, 70°–130°W) and Europe (30°–70°N, 10°W–45°E).

Inness et al. (2015a) utilized reanalysis data to investigate connections between El Niño/La Niña and atmospheric composition fields such as ozone, CO, and aerosols. They concluded that anomalies of CO and biomass burning aerosols depend mainly on local emissions. Hence, their strong positive anomalies over Indonesia during August–October 2015 (Figs. SB2.5a,b) were a direct consequence of the widespread fires in that region. Anomalies in ozone (O_3; Fig. SB2.5c), also produced by these fires, were further affected by El Niño–induced dynamical changes that altered the downward transport of O_3 from the stratosphere and modified O_3 photolysis rates. Total column CO anomalies that reached 500% in the core of the fire region were remarkable (Fig. SB2.5a), but even more striking were the extremely large anomalies (~2000%) in total AOD at 550 nm for biomass burning (OM+BC) aerosols that covered large areas of the Indian and western Pacific Oceans (Fig. SB2.5b). For tropospheric ozone (Fig. SB2.5c), the positive anomalies over Indonesia were a more modest 30%–40%.

The CAMS reanalysis is a valid tool for monitoring the evolution of large-scale pollution events in quasi near–real time and providing useful information at the onset of a pollution-related crisis. Because El Niño is highly predictable on a seasonal timescale and Indonesian fires are known to assume catastrophic proportions during exceptionally intense El Niño years, further development of CAMS towards integrating a seasonal prediction system with fire risk and air quality forecasts would provide comprehensive information for early warnings and planning of mitigation actions.

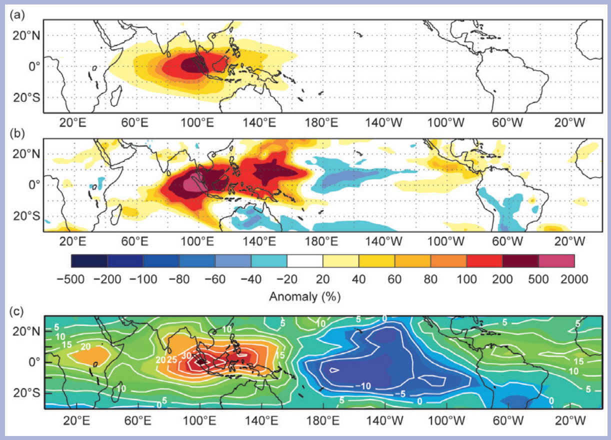

Fig. SB2.5. Anomalies (%) averaged over the 2015 Indonesian fire season (Aug–Oct) from the CAMS reanalysis of (a) total column CO and (b) biomass burning AOD at 550 nm. (c) Mean OMI/MLS tropospheric column ozone anomalies for Aug–Oct 2015, with contours drawn every 5%.

different satellite-based instruments. The spatial distribution of CO trends from the CAMS reanalysis (Fig. 2.54) shows significant decreasing trends of –1.0% to –1.5% year^{-1} in most regions north of 40°N, up to –3.0% year^{-1} over the Amazon basin and its outflow regions, –0.5% to –1.0% year^{-1} for most of the rest of the globe, and almost no trends over India, eastern China, and a large region surrounding Indonesia. Diminished anthropogenic emissions in North America and Europe as well as strong reductions in fire emissions over South America are the main causes for the decreasing global CO burden during 2003–15.

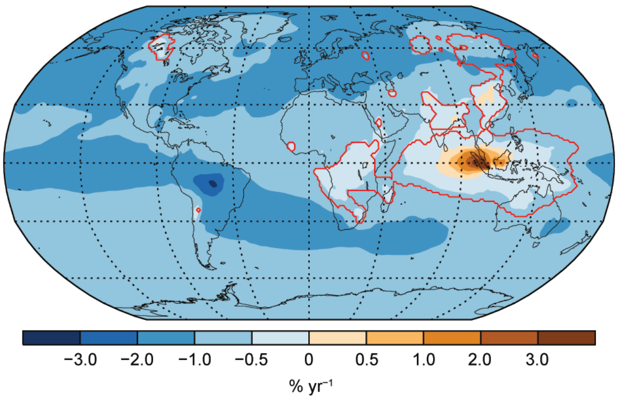

Fig. 2.54. Linear trends (% yr□¹) in total column CO from the CAMS interim reanalysis for the period 2003–15. All trends are statistically significant at the 95% level of confidence except for those inside red contours.

h. *Land Surface Properties*

1) Land surface albedo dynamics—B. Pinty and N. Gobron

The land surface albedo is the fraction of solar radiation scattered backward by land surfaces. In the presence of vegetation, surface albedo results from complex nonlinear radiation transfer processes determining the amount of radiation that is scattered by the vegetation and its background, transmitted through the vegetation layer, or absorbed by the vegetation layer and its background (Pinty 2012).

The geographical distribution of normalized anomalies in visible and near-infrared surface albedo for 2015 calculated with respect to a 2003–15 base period [for which two MODIS sensors are available (Schaaf et al. 2002)] are shown in Plates 2.1z and 2.1aa, respectively. Mid- and high-latitude regions of the Northern Hemisphere are characterized by both positive and negative anomalies, mainly as a consequence of interannual variations in cover, amount, and duration of snow in winter and spring seasons. The large negative anomalies over eastern Europe, southern Sweden, western Russia, Caucasus, southwestern Siberia, and northern China are probably associated with a below-average snow cover in winter and early spring seasons, due to the occurrence of relatively high temperatures in some of these regions. Similarly, negative anomalies over Canada can be related to an unusually small snow cover extent (section 2c2). The amplitude of these negative changes can reach (or locally exceed) ±30% in relative units and is larger in the visible than the near-infrared domain, although with the same sign. By contrast, the average February snow cover extent across the eastern United States resulted in a positive annual anomaly.

A few snow-free regions show positive anomalies, especially in the visible domain. In the equatorial regions, these are well marked over Indonesia and, with more limited amplitude, over Amazonia, central Africa and Queensland, Australia. These are generally associated with less favorable vegetation growing conditions compared with previous years (section 2h2), although contamination of the albedo retrievals by clouds and aerosol load, especially in Indonesia (Sidebar 2.2), may also have induced some artifacts. The majority of snow-free regions exhibit noticeable negative anomalies, particularly in the visible domain, across Mexico and the southern United States and over the southern regions of South America, Australia, India, and China. The unusually warm conditions over northern regions such as western Europe, Turkey, and northwestern Iran may have contributed to the observed limited negative anomalies. A significant fraction of these variations are attributable to vegetation dynamics (Pinty et al. 2011a, 2011b) over these regions, which are sensitive to stress from ambient conditions and, in particular, water availability. Although weaker in the near-infrared, these negative anomalies sometimes occur simultaneously in the visible and the near infrared. Generally, the amplitude of both positive and negative anomalies changes seasonally.

Analysis of the zonally-averaged albedo anomalies in the visible and near-infrared (Fig. 2.55) spectral domains indicates considerable interannual variations related to the occurrence of snow events in winter and spring at mid- and high latitudes but also in vegetation conditions during the spring and summer periods. Strong negative anomalies are noticeable between 20° and 45°S, featuring a deviation from average conditions mainly over the southern regions in Latin America, Africa, and Australia. Limited but consistent positive anomalies are discernible across equatorial regions in 2015.

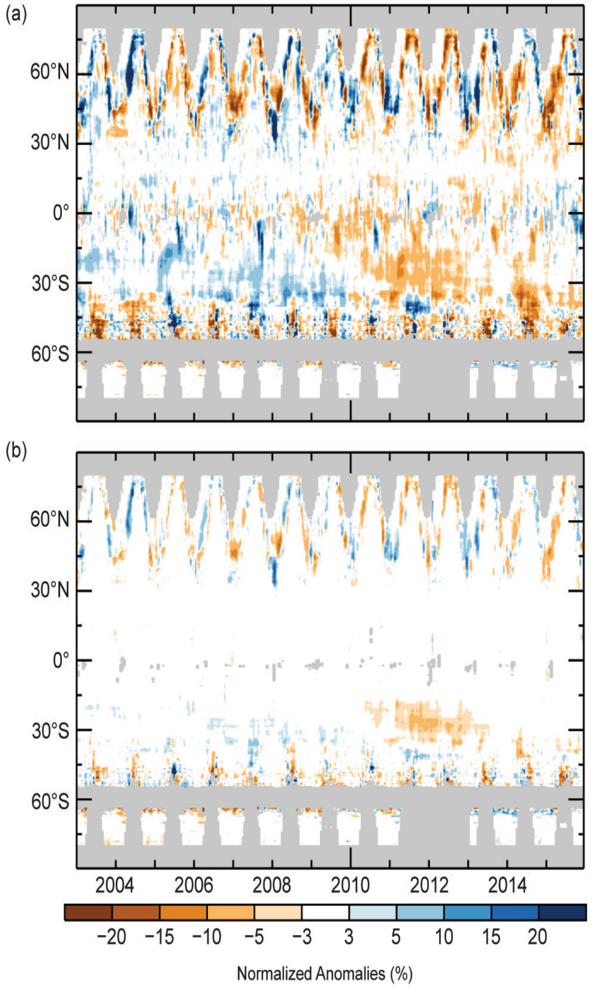

Fig. 2.55. Zonal means of the MODIS White Sky broadband surface albedo (NASA) normalized anomalies in the (a) visible and (b) near-infrared domain relative to a 2003–15 base period.

The 12-month running mean globally averaged normalized anomalies (Fig. 2.56) vary within ~±5% (~±3%) in the visible (near-infrared) domain. Antarctica is excluded owing to missing data. The year began with globally averaged negative albedo anomalies and ended with slightly positive anomalies. The trend towards positive anomalies was driven by contributions from the Southern Hemisphere. Figure 2.56 also shows analogous interannual and multiannual variations in the visible and near infrared during the 2003–15 base period, with mostly positive anomalies at the beginning of this base period.

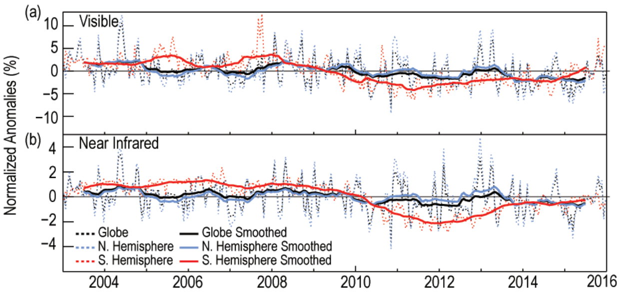

Fig. 2.56. Globally-averaged MODIS White Sky broadband surface albedo (NASA) normalized anomalies with a 12-month running mean in the (a) visible and (b) near-infrared domain relative to a 2003–15 base period at the global scale (black), Northern Hemisphere (blue), and Southern Hemisphere (red).

2) Terrestrial vegetation dynamics—N. Gobron

Analysis of the 18-year record shows that large spatiotemporal deviations in vegetation dynamics occurred at regional and continental scales during 2015 (Plate 2.1y). The state of vegetation is examined by merging 1998–2015 estimates of the Fraction of Absorbed Photosynthetically Active Radiation (FAPAR) from three different sensors: SeaWiFS (NASA), MERIS (ESA), and MODIS (NASA) (Gobron et al. 2010; Pinty et al. 2011b; Gobron and Robustelli 2013).

A large number of regions experienced seasonal precipitation deficits in 2015 (sections 2d4 and 2d9), especially in the Southern Hemisphere, along with much higher-than-average annual temperatures across most of the globe (section 2b1). This translates into a large variation in vegetated surface conditions.

The largest annual negative anomalies (not favorable for vegetation) occurred over the high northern latitudes from Alaska to Sweden and Norway, and also over the equatorial belt from central and northeastern Brazil, central Africa, and Indonesia. To a lesser extent, regions near the Black and Caspian Seas were also affected.

The largest positive annual anomalies appeared over Mexico, the southern United States, Minas Gerais (Brazil), Turkey, and China. Limited positive anomalies occurred over eastern parts of Europe, India, and the Ural region of Russia.

Below-normal precipitation occurred during the second half of the year in Brazil and Indonesia, impacting the annual anomalies. The anomalies over southwestern and central Africa were mainly due to a warmer-than-normal spring together with below-normal precipitation.

Higher precipitation in spring over Mexico and the southern United States and in autumn over western China contributed to favorable conditions for vegetation health and growth, as was the case in 2014. Over Turkey, the positive anomalies were mainly correlated with a slight excess of rainfall and higher temperatures compared to previous years.

Zonally averaged monthly mean anomalies (Fig. 2.57) illustrate the differences between the two

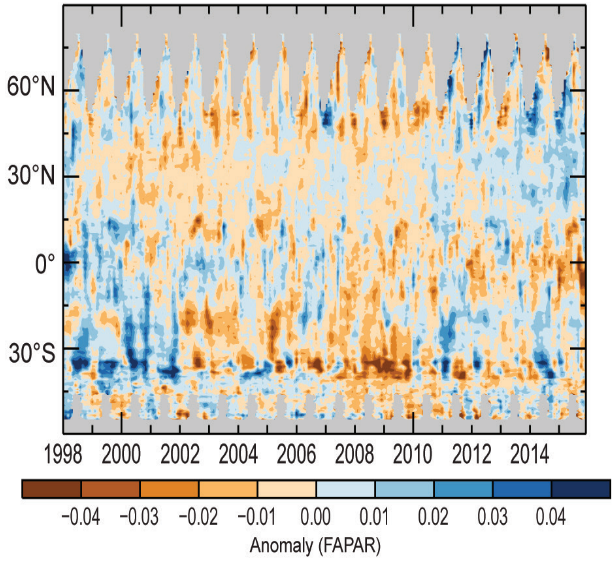

Fig. 2.57. Time series of monthly zonal anomalies (base period: 1998–2015) of the Fraction of Absorbed Photosynthetic Radiation (FAPAR) from SeaWiFS, MERRIS, and MODIS sensors. Gray areas indicate missing data.

hemispheres, with persistent negative anomalies over the Southern Hemisphere during all seasons from around 2002 to 2009. A succession of positive and negative anomalies, suggesting a seasonal cycle, are depicted between 10°S and 30°S since 2010. In contrast, strong positive anomalies are observed over regions between 20° and 60°N since 2012; these persisted during 2015. Larger seasonal negative anomalies are seen over mid- and high latitudes in the Northern Hemisphere since mid-2012. A strong negative anomaly is depicted in 2015 around the equatorial regions, likely influenced by low precipitation and severe fires over Indonesia (Sidebar 2.2); it appeared to extend into the entire Southern Hemisphere during the last quarter of 2015.

The monthly mean averaged anomalies smoothed using a 12-month running average (Fig. 2.58) indicate that 2015 shows a relatively unhealthy state of the vegetation over the Southern Hemisphere compared with a more healthy state over the Northern Hemisphere.

3) Biomass burning—J. W. Kaiser, G. R. van der Werf, and A. Heil

Climate and weather provide boundary conditions for biomass burning or landscape fires to occur; in return these fires influence climate and weather by emitting greenhouse gases and aerosols and by modifying surface properties such as albedo and roughness. Generally, most fires occur in the tropics where they are often started by humans to manage the landscape. This includes frequent burning in many savannas and the use of fire to clear forest and make way for agricultural land. In temperate and boreal regions, fires tend to occur less frequently and can be either human or lightning ignited.

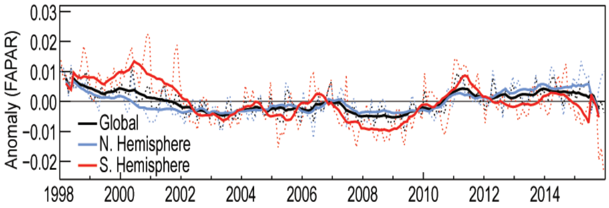

Fig. 2.58. Average monthly FAPAR anomalies with a 12-month running mean (base period: 1998–2015) at the global scale (black), Northern Hemisphere (blue), and Southern Hemisphere (red).

Since the late 1990s, fire occurrence and the associated burned area has been routinely detected by satellites. The Global Fire Assimilation System (GFAS) builds on active fire detections and their associated fire radiative power to estimate emissions in near–real time (Kaiser et al. 2012). GFAS is calibrated to partly match the Global Fire Emissions Database (GFED), which estimates emissions based on burned area and fuel consumption which have a much longer latency (van der Werf et al. 2010). The combined use of GFAS (2001–15) and GFED (1997–2014) indicates that fire emissions were on average 2.1 Pg C year^{-1} (Pg = 10^{15} g), with substantial interannual variability, the latter mostly stemming from tropical deforestation zones and the boreal region where fire activity varies more from year to year than in most savanna areas.

In 2015, total global fire emissions were somewhat above average (+4%, see Table 2.8). By far, the largest anomaly was found in tropical Asia, where emissions were almost three times as high as the 2001–14 average (Plate 2.1ab, Fig. 2.59). As in 2014, North America also saw higher-than-average emissions (see sections 7b1 and 7b2). These positive anomalies were partially compensated for on a global scale by below-average emissions from South America and Northern Hemisphere Africa. The former is related to a downward trend in deforestation during the last decade (Chen et al. 2013), although fire emissions in 2015 were somewhat higher than in the previous two years. The latter is in line with an ongoing trend, possibly due to expansion of cropland (Andela and van der Werf 2014)

The exceptional fire season in tropical Asia is apparent in the pronounced aerosol and carbon monoxide (CO) anomalies (sections 2g3, 2g7; Sidebar 2.2). The fires were most active during September and October (see Fig. 2.60) and located predominantly in

TABLE 2.8. Annual continental-scale biomass burning budgets in terms of carbon emission (Tg C yr^{-1}). 2001–02 from GFASv1.0 (Remy and Kaiser 2014), 2003–15 from GFASv1.3.

Time Period		2001–14	2015	
Quantity Tg C yr^{-1}		Mean Value (Range)	Value	Anomaly (%)
Global		2116 (1803–2371)	2201	86 (4%)
North America	30°–57°N 170°W–30°W	117 (50–171)	172	+55 (+47%)
Central America	0°–30°N 170°W–30°W	71 (54–102)	72	+1 (+1%)
S. Hem. America	0°–60°S 170°W–30°W	314 (170–477)	246	−68 (−22%)
Europe and Mediterranean	30°–75°N 30°W–60°E	39 (26–60)	36	−3 (−9%)
N. Hem. Africa	0°–30°N 30°W–60°E	405 (337–506)	369	−36 (−9%)
S. Hem. Africa	0°–35°S 30°W–60°E	519 (473–585)	509	−10 (−2%)
Northern Asia	30°–75°N 60°E–170°W	227 (122–449)	202	−25 (−11%)
Southeast Asia	10°–30°N 60°E–170°W	129 (83–173)	116	−13 (−10%)
Tropical Asia	10°N–10°S 60°E–170°W	123 (40–240)	340	+217 (+176%)
Australia	10°–50°S 60°E–170°W	172 (58–296)	140	−32 (−18%)
Sumatra		65 (17–147)	183	+118 (+182%)
Borneo		41 (8–93)	99	+58 (+142%)

Sumatra and Kalimantan (see Table 2.8, Plate 2.1ab, Fig. 2.59 and Fig. SB2.3). These regions are most vulnerable to ENSO because drainage and deforestation have created large areas with degraded peatlands that can burn easily under El Niño-induced drought conditions. Such peat fires are difficult to extinguish and usually last until the onset of the wet season in late October or early November. Accordingly, increased emissions were observed during the previous El Niño years of 2004, 2006, and 2009 (Fig. 2.60a).

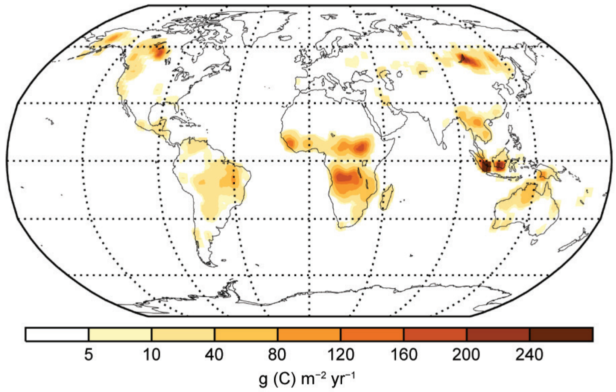

FIG. 2.59. Global map of fire activity in 2015 in terms of actual carbon consumption. (Source: GFASv1.3.)

Smoke from open fires in Indonesia has a strong impact on residents and economy (Marlier et al. 2013; Sidebar 2.2). In addition, peat burning represents a net source of CO$_2$ to the atmosphere because drainage prevents regrowth of peat. During the 2015 fire season of tropical Asia, about 80% of the pyrogenic carbon flux occurred in peatlands. Both the carbon flux and its relative peatland contribution were the highest since the MODIS record started in 2001 (Fig. 2.60a).

Pinpointing the exact magnitude of emissions remains challenging. This is largely due to difficulties in estimating the burn depth of peat fires, leading to larger-than-average uncertainties in any kind of emission assessment. Instead of fire observations, Huijnen et al. (2016) used satellite-based CO observations of the smoke plume and in situ measurements of the CO emission factors to estimate a carbon flux of 227 ± 66 Tg C for the most affected subregion of tropical Asia during September and October. The corresponding values for GFASv1.2 and GFASv1.3 are 320 and 250 Tg C, respectively, while preliminary GFED4 estimates are about 400 Tg C (www.globalfiredata.org/updates.html), but this estimate includes the full fire season. Compared to GFASv1.2, GFASv1.3 includes an improved representation of the diurnal variability of cloud cover, which prevents satellite observations of fires, and a higher-resolution peat map based on Wetland International (Wahyunto et al. 2003, 2004). While 2015 was the highest fire year in the GFAS record in tropical Asia, scaling the 2015 GFAS record to GFED based on a common base period in 2006 indicates that 2015 was only about half as strong as the extreme year 1997 (Fig. 2.60b).

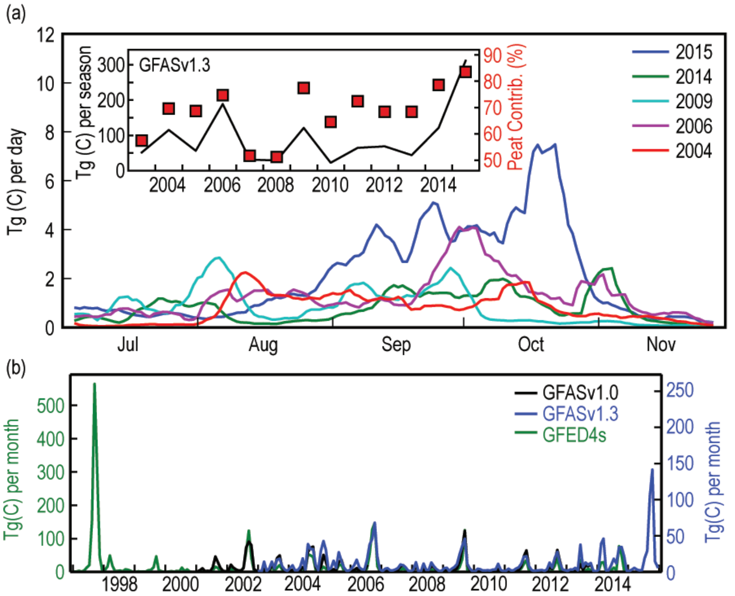

Fig. 2.60. (a) Temporal evolution of fire emissions in tropical Asia during the Sep–Oct 2015 fire season, compared to the four most active fire seasons since 2003 (5-day smoothed GFASv1.3 data). The inset shows annual total emissions since 2003 and the relative contribution of fire emissions from peat fires, highlighting the increased relative importance of these fires in high fire years. (b) Monthly fire activity in tropical Asia for 1997–2015. The *y*-axis ranges are adjusted so that GFED4s and GFASv1.3 coincide graphically in Oct 2006.